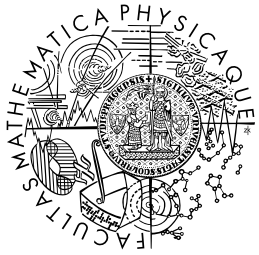

FACULTY
OF MATHEMATICS
AND PHYSICS
Charles University

MASTER THESIS

Ivo Vinklárek

Temperature dependence of the triplet-triplet energy transfer in photosynthetic light-harvesting complexes

Department of Chemical Physics and Optics

Supervisor of the master thesis: doc. RNDr. Jakub Pšenčík, Ph.D.

Study programme: Physics

Study branch: Biophysics and Chemical physics

Prague 2017

I declare that I carried out this master thesis independently, and only with the cited sources, literature and other professional sources.

I understand that my work relates to the rights and obligations under the Act No. 121/2000 Sb., the Copyright Act, as amended, in particular the fact that the Charles University has the right to conclude a license agreement on the use of this work as a school work pursuant to Section 60 subsection 1 of the Copyright Act.

In ..... date ..... signature of the author

Title: Temperature dependence of the triplet-triplet energy transfer in photosynthetic light-harvesting complexes

Author: Ivo Vinklárek

Department: Department of Chemical Physics and Optics

Supervisor: doc. RNDr. Jakub Pšenčík, Ph.D., Department of Chemical Physics and Optics

Abstract: Toxic singlet oxygen can be populated by the quenching of triplet states of chlorophyll (Chl). In photosynthetic light-harvesting complexes (LHCs), the generation of singlet oxygen is prevented by a photoprotective mechanism based on an energy transfer from Chl triplets to carotenoids, which occurs via a Dexter mechanism (DET). The temperature dependence of the DET was studied in three selected LHCs by means of transient absorption spectroscopy. The emphasis was on a chlorophyll *a*-chlorophyll c_2-peridinin-protein complex (acpPC) of *Dinoflagellate Amphidinium carterae*. The results obtained from acpPC were compared with those acquired for LHC-II from pea and chlorosomes of *Chloroflexus aurantiacus*. All three antennas exhibit high efficiency and fast rate of chlorophyll triplet quenching by carotenoids at room temperature, which prevents the accumulation of Chl triplets. The fast rate of quenching persists at low temperatures ($\geq$77 K) in the case of LHC-II. However, the efficiency of the Chl triplets quenching is lower as proved by a detection of long-lived Chl triplets with a millisecond lifetime. These triplets were assigned to peripheral Chls that are not neighbouring with carotenoids active at 77 K. A similar population of long-lived Chl triplets was detected in the acpPC complex. In acpPC, the rate of the quenching by carotenoids is different in three subpopulations of carotenoids. The first subpopulation is ascribed to peridnin in a non-polar environment (or diadinoxanthin) and exhibits a fast rate of DET independently of temperature. Two other subpopulations formed by peridinin in a polar and non-polar environment (or diadinoxanthin) show a strong temperature dependence with a more than 1000 times lower rate at 77 K compared to room temperature. Chlorosomes also exhibit the temperature dependence of the quenching rate by carotenoids. However, no long-lived bacteriochlorophyll triplets were detected.

Keywords: light-harvesting complexes, quenching of chlorophyll triplet states, transient absorption spectroscopy

I would like to thank Prof. Eckhard Hofmann and Dr. Heiko Lokstein for providing the samples. Especially, I am grateful to my supervisor, Dr. Jakub Pšenčík, for encouraging me and for providing me with excellent advice throughout the thesis process. Many thanks also to Dr. Jan Alster, who provided me with the global analysis program and who helped me solve several problems. Finally, I would like to thank to my colleagues for creating a good laboratory atmosphere.

This thesis is dedicated to my parents, my brother, my grandmother, František and Radka, for their love and constant support, and for giving me the opportunity to study.

Contents

Introduction

The great variety of life conditions on Earth led to the evolution of a broad range of photosynthetic organisms with different abilities to use sunlight as their life propulsion. Photosynthesis may serve as an inspiration for the currently topical issue of the shortage of energy supplies. Fossil fuels - in fact products of photosynthesis - are quickly being exploited by our growing society. One of the possible solutions to the problem is to master biophysical paths of light-harvesting and storing the energy from sunlight into a fuel or batteries. Artificial photosynthesis seems to be a utopian concept from today's perspective. However, some pioneers of artificial photosynthesis research, like Daniel Nocera [1], have convinced us of the good prospects of a replication of natural photosynthesis. A prerequisite for success is fundamental research on light-harvesting and the photoprotection in natural photosynthesis, which is the subject of this thesis.

Photosynthesis is a biosynthetic process in which plants, algae and some bacteria acquire energy from sunlight and store it in high-energy macromolecules by attaching carbon dioxide. The process can be divided into primary processes called "light-dependent" photosynthesis and subsequent processes called the Calvin cycle, which embraces the "light-independent" reactions of photosynthesis. [2] Although the processes are called light-independent, they are inefficient without a sufficient supply of energy from the primary light-dependent reactions.

In the light-dependent processes, a photon is absorbed by pigments in the protein complexes called light-harvesting complexes (LHCs, or "light-harvesting antennas"). The subsequent excitation is then transferred from the pigments in the LHC to the pigments in the reaction centre (RC), where the excitation is trapped and used for charge separation. The separated electron is transported from the pigments in the RC step-by-step through a reduction line with decreasing redox potential in exchange for the protons pumping across a membrane. The disequilibrium of ions on both sides of the membrane makes a gradient of Coulomb and chemical potential, which forces the ATP-synthase complex to form adenosine triphosphate (ATP) with a high-energy bond. Consequently, another energy carrier, nicotinamide adenine dinucleotide (NAD^+), is reduced as the last step in the electron transport chain. Both highly energetic molecules - ATP and NADH - provide energy for light-independent processes. [2]

Although there are some differences in these briefly summarized photosynthesis processes among plants, algae, and photosynthetic bacteria, all of the photosynthetic organisms use LHCs for harvesting photons by pigments being absorbed in the visible spectrum. Otherwise, the RCs would stay inactive for most of the time. However, the LHCs are quickly overfilled by excitation energy during sunshine. [2] Majority of the pigments involved in the energy transfer are chlorophylls (Chls) or bacteriochlorophylls (BChls), which can populate the long-lived triplet (T_1) states by intersystem crossing from the first singlet excited (S_1) state, when they cannot transfer excitation to the next pigment. Unfortunately, the T_1 states of Chl and BChl can be quenched by the ground triplet state of molecular oxygen, giving rise to a singlet state of oxygen ($^1O_2$); see figure 1.1. [3] $^1O_2$ belongs among reactive oxygen species, which are toxic for a photosystem and can cause damage through the oxidation of some of the photosystem subunits. [4] During evolution,

organisms developed several photoprotective processes. One of them is based on carotenoids, which can quench the T_1 states of Chl and BChl, and thus prevent the generation of $^1O_2$, or eventually they can quench directly $^1O_2$. Except for the above mentioned processes, there are other photoprotective processes involved in photosynthesis, such as non-photochemical quenching or the detachment of LHCs from the photosystem. [2, 5, 6, 7, 8]

This work focuses on photoprotective processes occurring in selected LHCs at a low temperature. The emphasis is on the efficiency of the quenching of Chl triplets in a chlorophyll *a*-chlorophyll c_2-peridinin-protein complex (acpPC) of the alga *Amphidinium carterae*, which is compared with the light-harvesting complex II (LHC-II) of a pea and the chlorosomes of the green non-sulfur photosynthetic bacterium *Chloroflexus aurantiacus*. *Amphidinium carterae* belongs to the *Dinoflagellates*, which are important members of marine phytoplankton. For instance, *Symbiodinum* is a coral symbiotic *Dinoflagellate*, which contains acpPC and plays a crucial role in coral bleaching. [9] Marine phytoplankton is responsible for more than 45 % of the net primary production of photosynthesis on the Earth [10], and it significantly contributes to the Earth's biosphere stability. [11] The photosynthetically-active marine phytoplankton had to adapt their light-harvesting antennas to blue-green solar irradiance below the ocean surface; see figure 1.17. Therefore, marine algae often utilize carbonyl-containing carotenoids like peridinin for light-harvesting. [11] One may ask a question whether the efficiency of the photoprotective processes in marine algae is affected by carbonyl-containing carotenoids. This study follows up on the previous findings of Kvíčalová et al. [12], who concluded that the Chl triplet states are quenched by carotenids with 100 % efficiency in acpPC and the peridinin-chlorophyll *a*-protein complex (PCP) of *A. carterae* at room temperature (RT). However, the efficiency of the chlorophyll triplet quenching in acpPC seems to be lower at low temperatures (< 77 K). Niedzwiedski et al. [9] reported long-lived triplet states of Chl at 77 K with lifetimes $\approx$150 ns and $\approx 2\,\mu$s [9]. On the contrary, the PCP complex, which has a very similar pigment composition, but very different structure, shows the ability to quench triplets of Chl independently of temperature [13]. However, the PCP antenna is unique in this respect, and the detection of long-lived triplet states of Chl at low temperatures is not rare among LHCs. [14, 15, 8] The decrease in carotenoid quenching ability may occur as a result of the structural changes in LHCs with decreasing temperature or due to the intrinsic dependency on temperature of the Dexter mechanism of energy transfer, which governs the process of Chl triplet quenching by carotenoids.

1. Theory

1.1 Light-harvesting complex

All photosynthetic organisms need a stable, non-harming supply of energy to the reaction centre (RC), where it triggers the charge separation. The excitation energy is mostly acquired and transferred from the so-called light-harvesting antennas (LHC, or "light-harvesting complex"). [5] These are comprehensive functional subunits of photosynthetic apparatus that absorb sunlight and funnel the gained energy to the other antennas towards the RC by energy transfer (ET). It should be mentioned that contrary to the photosynthetic RCs, where the structure is preserved among different photosynthetic organisms, the structure of LHC varies a lot depending on the photosynthetic organisms species and their natural conditions. [2]

Each LHC absorbs a photon by its pigments, which subsequently transfer the excitation energy to the other pigments in the direction of the RC. However, the ET does not usually occur in a one-dimensional organization and the variety of ET pathways in a three-dimensional organization of LHC can serve as guarantee of the energy supplement to the RC. [2] The probability of a pigment being in an excited state ($p_i^\star$) is driven by Pauli's master equation

$$\frac{\mathrm{d}p_i^\star}{\mathrm{d}t} = \sum_j \left(k_{ji}p_j^\star - k_{ij}p_i^\star\right) - \frac{p_i^\star}{\tau_i}, \tag{1.1}$$

where k_{ij} are rate constants of ET from a donor pigment i to an acceptor pigment j and τ_i is a natural lifetime of a pigment i (figure 1.1). In order to prevent reverse energy transfer, the pigments closer to the RC absorb at gradually longer wavelengths and the energy between them is transferred by Förster mechanism, which leads to the sacrificing of part of the energy. This is called the 'funnel' concept. [2]

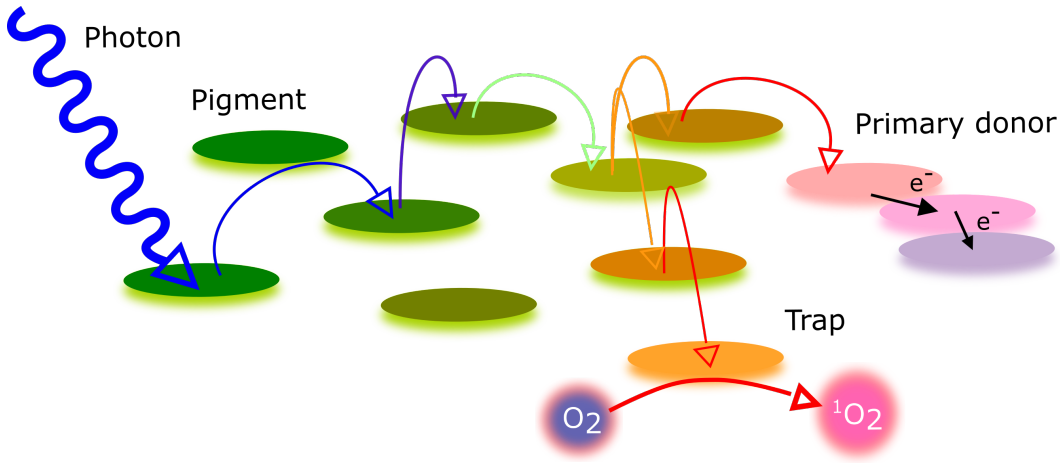

Figure 1.1: Scheme of light-harvesting of photons and energy transfer of absorbed energy to the primary donor.

The LHCs are divided according to their spatial position in respect to the RC into integral membrane and peripheral membrane light-harvesting antennas. [2]

The integral membrane LHCs are further split into different forms - fused, core and accessory antennas. All of the integral membrane LHCs are embedded in a bilayer lipid photosynthetic membrane. The fused and core antennas are inner complexes, which are directly connected to the RC. The fused LHCs form a cover around the special pair and electron transfer components. Core LHCs are strongly bound to the RC by hydrophobic bonds and they have a precise stoichiometric ratio to the RC. The inner antennas mediate energy transfer from outer LHCs. Accessory antennas are nested in the membrane by α-helices and they are usually mobile. The position or stoichiometry of attached accessory antennas to the RC depend on the cultivating conditions and light stress. [2] Peripheral membrane antennas have a hydrophilic nature and are located in an intermembrane space and attached to a component, which is buried in the membrane. Peripheral antennas also transfer the absorbed energy to the RC through integral membrane antennas. [2, 16]

The pigments in LHCs can be found strongly coupled (e.g. LH1 purple bacteria, chlorosomes) or weakly coupled (e.g. LHC II of higher plants). [17] For instance, the strong coupling is characterized by stronger dipole-dipole interaction (V_{ij}) among pigments than the interaction of pigment with the surrounding environment (Γ_m). The strong coupling leads to the splitting of energy levels and the excitation is delocalized. Oppositely, the situation of weak coupling $V_{ij} < \Gamma_m$ leads to a non-coherent energy transfer. [17] For example, non-coherent energy transfer occurs in the case of isolated molecules. The next sections and paragraphs will be discussed from the view of a weak coupling.

1.2 Energy transfer

The excited pigment called a donor can transfer energy to the other pigments called acceptors located in the same LHC or a different antenna. Although the ET is known to be a resonance energy transfer (isoenergetic) [18], some of the gained energy is quickly lost after the ET by vibrational relaxation (VR) to the lowest vibrational level in exchange for the irreversible energy flow ($k_{ET} < k_{VR}$). This illustrates that the rate constant of the ET is highly dependent on the energetic difference between purely electronic states of a donor and an acceptor. In general, the exergonic ("downhill") processes are more favourable than the endergonic. [19] The thermal energy can break the irreversibility of the process, but the probability and rate constant of the reverse transition are much lower compared to the funnelling toward the RC. [2] The loss of energy for the sake of the higher rate and directivity of ET suggests that the most eminent property for energy supply is not the energetic efficiency (energy provided by antennas/absorbed energy), but the quantum efficiency. The efficiency of this energy funnel is also strongly dependent on the composition of pigments, their interactions, energetic sub-ordinance and, most importantly, on interactions of pigments with the surrounding environment which influences their energy of transition by the electrostatic interactions, prevents diffusion of pigments and keeps them at a certain respective distance. Simultaneously, the ET competes with other relaxation pathways. [20, 21, 17]

An excited pigment can relax to the ground (S_0) state by various pathways involving radiative and non-radiative paths. The pigment usually relaxes to the

S_1 state from a higher singlet state through a non-radiative decay like internal conversion (IC) due to the vibrational state coupling ($\approx 10^{-14} - 10^{-11}$ s, [22]). The relaxation from the S_1 state can occur by emission of a photon called prompt fluorescence (further only 'fluorescence'), whose lifetime is usually up to several nanoseconds at RT for tetrapyrrole pigments. In the case of a large spin-orbit coupling, caused e.g. by the presence of a magnesium ion in the centre of chlorophyll, the T_1 excited state can be generated through intersystem crossing (ISC) from the S_1 state ($\approx 10^{-8} - 10^{-3}$ s) with higher probability. [22] The T_1 state can relax to the S_0 state by ISC, emission of a photon, or by delayed fluorescence through reverse ISC to the S_1 state. All the mentioned mechanisms of relaxation compete with ET and lower its efficiency.

The ET in LHC occurs by several distinct mechanisms, whose description is derived from the perturbation theory. The theory specifies the molecule excited by a photon as a Frenkel exciton, which can interact with surrounding molecules. [23] The quantum excited state consists of an excited electron located on the molecule and a vacancy in the highest occupied molecular orbital (HOMO). The ET mechanisms, which are discussed in the next sections, are the result of a weak interaction between one molecule in an excited state and a second molecule in the S_0 state

$$M_1^* + M_2(S_0) \xrightarrow{k_{ET}} M_1(S_0) + M_2^*. \tag{1.2}$$

Their interaction arises as a consequence of the Coulomb interaction. The electrostatic potential describing the Coulomb interaction of two pigments - donor and acceptor - is

$$V_{El.stat.} = \frac{1}{4\pi\epsilon_0} \sum_{i \neq j} \frac{q_i q_j}{r_{ij}}. \tag{1.3}$$

The interaction between two molecules described by a general form in equation 1.3 behaves like a two-body operator, which couples two particles at any given moment. The wavefunction describing the initial electronic state of a donor and an acceptor is provided by the Slater determinant, which ensures that the wavefunction is antisymmetrical. [24] The wavefunction for an initial state is a product of orthonormal spin-orbitals $\phi(i) = \varphi(i)\sigma(i)$, where φ is a spatial function, and σ is a simple function of spin coordinate with values of $\uparrow$ or $\downarrow$.

$$|\psi_I(D^*A)\rangle = |\phi_{D1}\phi_{D2}\phi_{D3}...\phi^*_{Dn}\phi_{A1}\phi_{A2}\phi_{A3}...\phi_{Am}| =$$
$$= \frac{1}{\sqrt{k!}} \begin{vmatrix} \phi_{D1}(1) & ... & \phi^*_{Dn}(1) & \phi_{A1}(1) & ... & \phi_{Am}(1) \\ \phi_{D1}(2) & ... & \phi^*_{Dn}(2) & \phi_{A1}(2) & ... & \phi_{Am}(2) \\ ... & ... & ... & ... & ... & ... \\ \phi_{D1}(n+m) & ... & \phi^*_{Dn}(n+m) & \phi_{A1}(n+m) & ... & \phi_{Am}(n+m) \end{vmatrix},$$

and similarly for the final electronic state

$$|\psi_F(DA^*)\rangle = \left|\phi_{D1}\phi_{D2}\phi_{D3}...\phi'_{Dn}\phi_{A1}\phi_{A2}\phi_{A3}...\phi^*_{Am}\right|. \tag{1.4}$$

The rate constant of the non-radiative ET in systems with a weak coupling can be calculated from the Fermi-golden rule [20, 19]

$$k_{ET} \approx M^2 = \frac{4\pi^2}{h} \langle\psi_I(D^*A)|V_{El.stat.}|\psi_F(DA^*)\rangle^2 \rho(E), \tag{1.5}$$

where $\rho(E)$ is a density of vibrational states. $\rho(E)$ must be included in the case of the non-resonance ET due to the fact that the ET is isoenergetic.

The equation 1.5 can be split into two terms using the Slater-Condon rules due to orthonormal spin-orbitals. The Slater-Condon rules claim that the integrals over the initial and final state with more than two different spin-orbitals vanish from equation 1.5. It is evident that the initial and final states in the case of ET differ exactly in two spin-orbitals. Therefore, the results are two terms [19]

$$\begin{aligned} &\sum_{i\neq j}\langle\psi_I(D^*A)|\frac{1}{r_{ij}}|\psi_F(DA^*)\rangle = \\ &= \langle\varphi_D^*(1)\varphi_A(2)|\frac{1}{r_{12}}|\varphi_D(1)\varphi_A^*(2)\varphi\rangle\langle\sigma_D^*(1)|\sigma_D(1)\rangle\langle\sigma_A(2)|\sigma_A^*(2)\rangle - \\ &-\langle\varphi_D^*(1)\varphi_A(2)|\frac{1}{r_{12}}|\varphi_A^*(1)\varphi_D(2)\rangle\langle\sigma_D^*(1)|\sigma_A^*(1)\rangle\langle\sigma_D(2)|\sigma_A(2)\rangle. \end{aligned} \tag{1.6}$$

The first term is called a direct term and it leads to the Förster resonance ET (FRET) mechanism in long-distance approximation. The direct term conserves the spin multiplicity of each molecule. The second term is called an exchange term and it leads to the Dexter ET mechanism. The exchange term conserves multiplicity of the exchanged electron. Except for the processes like triplet-triplet ET, it can also allow singlet-singlet ET. The comparison of these two processes is shown in figure 1.2, which explains why the Dexter mechanism is sometimes denoted as an electron exchange mechanism. [19]

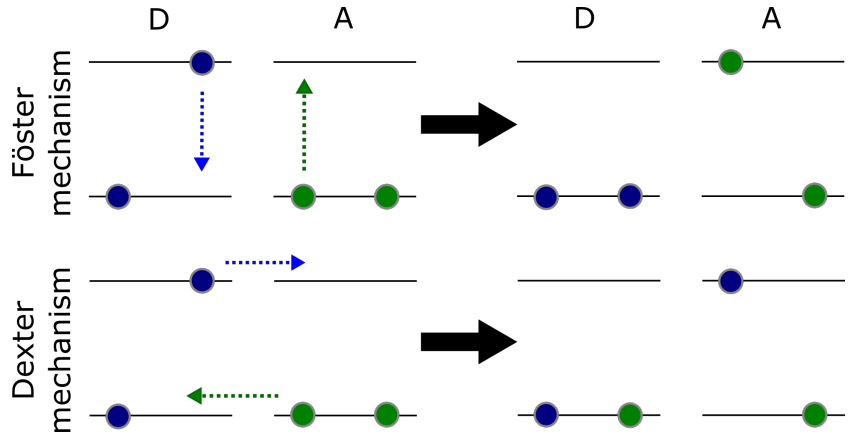

Figure 1.2: Scheme of Dexter and Förster energy transfer mechanisms.

In fact, the previous paragraph explains that both mechanisms are present in singlet-singlet ET, but one dominates over the other in exact donor-acceptor distance separation. Obviously, the mechanisms of ET discussed in the next sections differ in required conditions for an efficient ET from donor to acceptors such as the relative molecules orientation and the distance separation, spin multiplicity, temperature, spectral properties of donor and acceptor or their transition dipole moments.

1.2.1 Dipole-dipole energy transfer (Förster)

The potential of electrostatic interaction 1.3 can be separated into components of internal interactions within each pigment, which are not involved in ET, and ex-

ternal interactions between two pigments that provides ET in the case of pigment separation much larger than the size of the molecule [25]

$$V_{el.stat.} = V_{int.} + V_{ext.} = V_{int.} + V_{DA} = V_{int} + \frac{1}{4\pi\epsilon_0} \sum_{I\in D,\ J\in A} \frac{q_I q_J}{r_{IJ}}. \tag{1.7}$$

The interaction term V_{DA} can be simplified in the limit of long distance separation by the multipole expansion containing components with donor and acceptor charges $q_{D/A}$, electric dipole moments $\vec{\mu}_{D/A}$ and quadrupole electric tensors $Q_{D/A}(ij)$. [25]

$$\begin{aligned} V_{DA} \approx \frac{q_D q_A}{r} + \frac{q_D(\vec{\mu}_A\hat{\vec{r}}) - q_A(\vec{\mu}_D\hat{\vec{r}})}{r^2} + \frac{\vec{\mu}_D\vec{\mu}_A + 3(\vec{\mu}_D\hat{\vec{r}})(\vec{\mu}_A\hat{\vec{r}})}{r^3} + \\ + \frac{q_D\left[Q_A(xx) + Q_A(yy) - 2Q_A(zz)\right]}{r^3} \\ + \frac{q_A\left[Q_D(xx) + Q_D(yy) - 2Q_D(zz)\right]}{r^3} + ... \end{aligned} \tag{1.8}$$

The application of multipole expansion in the limit example of ET leads directly to dipole-dipole (Förster) mechanism due to charge neutrality of a donor and an acceptor. The only non-zero element in the equation 1.8 is the third element describing the dipole-dipole interaction. The other (not shown) non-zero components are involved in dipole-quadrupole, quadrupole-quadrupole and higher orders of interaction and they quickly decrease with distance compared to the dipole-dipole component. The expression for interaction V_{DA} can be rewritten as [17]

$$V_{DA} = \frac{5.04\kappa_{DA}}{\varepsilon} \frac{\mu_D\mu_A}{r_{DA}^3}, \tag{1.9}$$

where $\kappa_{DA} = \cos\alpha - 3\cos\beta_i\cos\beta_j$ describes relative position and orientation between acceptor and donor dipole vectors and ε is permittivity. The squared brackets in equation 1.5 can be split into two components using the previous expression and a presumption that in the case of the weak interaction, the wavefunction of system donor-acceptor can be expressed as a combination of wavefunctions of isolated systems

$$\langle\psi_I(D^*A)|V_{DA}|\psi_F(DA^*)\rangle^2 = const.\frac{\kappa^2}{r_{DA}^6}\left[\langle\psi(D^*)|\mu_D|\psi(D)\rangle\langle\psi(A)|\mu_A|\psi(A^*)\rangle\right]^2. \tag{1.10}$$

The total probability of FRET is calculated through a distribution of initial state of donor and acceptor φ_{D^*}, φ_A, their degenerations g_A, g_{D^*} and the difference of energy between the initial and final states $E = E_I - E_F = (\epsilon_{D^*} + \epsilon_A) - (\epsilon_D + \epsilon_{A^*})$ [19]

$$\begin{aligned} P_{D\longrightarrow A} = \\ \frac{4\pi^2}{hg_Ag_{D^*}}\frac{5.04\kappa^2}{\epsilon r_{DA}^6}\int \mathrm{d}E \int \mathrm{d}\epsilon_A\varphi_A(\epsilon_A)\int \mathrm{d}\epsilon_{D^*}\varphi_{D^*}(\epsilon_{D^*})\times \\ \times\left[\langle\psi(D^*)|\mu_D|\psi(D)\rangle\langle\psi(A)|\mu_A|\psi(A^*)\rangle\right]^2 \end{aligned} \tag{1.11}$$

The last equation can be simplified to an expression which depends only on factors that can be determined experimentally, e.g. emission spectra f, extinction coefficients ε_A, index of refraction, lifetimes [19]:

$$k_{DA} = \frac{1}{\tau}\left[\frac{r_0}{r_{DA}}\right]^6, r_0 = 8.875 \times 10^{17}\frac{\kappa^2}{n^4}\int f_D(\nu)\varepsilon_A(\nu)\nu^{-4}\mathrm{d}\nu, \tag{1.12}$$

where τ is a lifetime of a donor fluorescence, when no acceptor is present. R_0 is distance, where the efficiency of ET is 50%. One might be surprised that the rate constant for a non-radiative mechanism contains a dependency on absorption and emission spectra. However, as we can see from the expressions above, it is derived from the component $\rho(E)$ describing the density of donor and acceptor states.

To recapitulate, the FRET occurs via coupling of a donor and acceptor by dipole-dipole interaction, which triggers the ET resulting in two simultanous transitions $D^* \rightarrow D$ and $A \rightarrow A^*$. [19, 20] The induction of a dipole oscillation in the acceptor can be carried out for a long distance and does not require overlap of the frontier orbitals. [19] The FRET is mainly responsible for singlet-singlet energy transfer in LHCs.

1.2.2 Triplet-triplet energy transfer (Dexter)

The theory of energy transfer induced by electron exchange mechanism was proposed by David L. Dexter and in his honour it is sometimes called "Dexter" energy transfer (DET) in literature. DET occurs through simultaneous exchange of the excited electron from the lowest unoccupied molecular orbital (LUMO) of the donor, which is transferred to the LUMO of the acceptor, and the electron from HOMO of the acceptor, which is oppositely transferred to the HOMO of the donor (see figure 1.2). The final state of the process is usually the acceptor in an excited state and the ground state of a donor. Except for the ET, the Dexter mechanism can explain triplet-triplet annihilation, which describes the interaction of two triplets resulting in a higher excited singlet and ground singlet states. The simplified figure 1.2 of DET considers the whole process as double electron transfer, which can be described through Marcus theory. [26, 20] Therefore, the interacting system must fulfil the same necessities for the efficient DET mechanism as for single electron transfer. Primarily, only a donor and acceptor with significant mutual overlap of their wavefunctions can exchange their electrons.

The rate constant of DET can be expressed by the following equation, which is derived from the Marcus theory [20]

$$k_{DET} = \frac{2\pi|H_{if}|^2}{h}\left(\frac{\pi^2}{\lambda RT}\right)\exp\left(-\frac{\Delta G^\dagger}{RT}\right), \tag{1.13}$$

where R is molar gas constant and T is absolute temperature. The expression illustrates the intrinsic dependence of DET on temperature, which can cause the smaller efficiency of the ET at low temperatures. The quantum operator $|H_{ij}|$ is the electronic coupling matrix between donor and acceptor. λ and $\Delta G^\dagger$ are reorganization energy and Marcus free energy of activation, respectively. Marcus free energy of activation exhibits quadratic dependence on the standard free energy of reaction ΔG^0 and λ according to the next equation

$$\Delta G^\dagger = \frac{(\Delta G^0 + \lambda)^2}{4\lambda}. \tag{1.14}$$

The Dexter mechanism expression has a complicated dependence on the distance of acceptor and donor separation and is usually approximated by an exponential function [20]

$$k_{DET} \approx \exp\left(\frac{-2r_{DA}}{L}\right) \int f_D(\nu)\varepsilon(\nu)\mathrm{d}\nu, \tag{1.15}$$

where L is a sum of van der Waals radii of orbitals of a donor and acceptor.

In summary, the Förster mechanism is more efficient in the long-range interaction ($1\,\mathrm{nm} < l \leq 10\,\mathrm{nm}$), and it is dependent on dipoles (oscillator strength) of a donor and an acceptor and their respective orientation. On the contrary, the rate of the DET is independent of the magnitude of transitions moments of a donor or an acceptor and it is active mostly in close contact. Usually, the distance does not exceed more than 1 nm. The strong dependence of DET on the distance separation, which can be explained from the consideration of the DET as the double electron transfer process. [20] Accordingly, the DET depends on the sum of the tunnelling efficiencies of both electron transfers. The ET processes can also be distinguished according to their temperature dependence. The DET rate constant is decreasing with temperature. On the contrary, the FRET is temperature independent and not a thermally activated process in general. However, the situation can be much more complicated. For example, the respective position between a donor and an acceptor may depend on temperature. Also, the rate constants of both mechanisms depend on the overlap between the absorption spectrum of an acceptor and the emission spectrum of a donor.

One can ask if it is possible to realize the ET without electric interaction between two pigments? Except for various types of interactions like magnetic, which are often negligible compared to the electric interaction, there is another ET mechanism sometimes called trivial. [20, 19] In the trivial ET a donor emits a photon that is later absorbed by an acceptor. The trivial ET does not shorten the emission lifetime or the emission probability of the excited donor. The efficiency of the trivial ET depends on the quantum yield of donor emission, number of molecules in the path of an emitted photon, an extinction coefficient of the acceptor at the photon wavelength and the spectral overlap of emission spectrum of the donor and absorption spectrum of the acceptor. Due to the minuscule extinction coefficient of transitions with change of the spin multiplicity, it is only singlet-singlet ET which occurs by the trivial mechanism. The efficiency of the trivial ET decreases with squared distance from photon source

$$k_{trivial} \propto \frac{1}{R^{-2}}. \tag{1.16}$$

Nevertheless, the trivial mechanism of ET is usually much less effective than the other ET mechanisms.

1.3 Spectroscopic and structure properties of LHC pigments

Pigments are fundamental elements of photosynthetic light-harvesting apparatus. Their functions include absorption of a photon, transfer of excitation energy toward the RC, a photochemical transformation of energy in the RC and protection

of photosynthetic apparatus against photodamage. These functions are directly connected to their spectroscopic properties and interactions with the surrounding environment, which is usually formed by proteins.

Based on the semi-empirical quantum chemistry method called the extended Hückel molecular orbital method, the absorption of a photon and simultaneous molecule excitation at the visible range of spectrum can be explained by an interaction of a photon with the valence electrons from a conjugated double bond system. [24, 27] In the Hückel theory, σ and π electron orbitals are orthogonal due to a different symmetry and they form non-interacting blocks in the Hamiltonian matrix. [27] Therefore, the spectroscopic properties of molecules can be extracted from the conjugated system of double bonds, which consists of a linear combination of π orbitals with delocalized electrons. The interaction of a photon with the valence electrons leads to the electronic transition from π to empty $\pi^\star$ anti-bonding orbitals. [24]

The linear molecules (e.g. carotenoids) with a conjugated double bond system absorb photons with energy inversely proportional to the length of the conjugated system. The phenomenon can be explained by the model concept of a particle in an infinite potential well. The one-dimensional Schrödinger equation describes the situation and its solution for a quantum state where the main quantum number is n: [28]

$$E\psi(x,t) = \left[-\frac{h^2}{2m}\Delta + V(x,t)\right]\psi(x,t), \psi(0) = \psi(L) = 0 \Longrightarrow E_n = \frac{n^2h^2}{8mL^2}, \tag{1.17}$$

where m is a mass of an electron and L is well width. The solution for the equation 1.17 relates the quantum state energy level with well width ($\approx$ length of the conjugated system) by squared inverse proportion. The concept can be justified only if the electrons in the conjugated system can move almost freely, which is in good agreement with experiment results. [27]

However, the Hückel's simplified view on a conjugated system gives no information about the intensity of the transition. The Fermi-golden rule 1.18 describes the probability of molecule transition from the ground state to an excited state by absorption of a photon

$$W_{g\to e} = \frac{2\pi}{h}\langle\psi_e^\star|H_{int}|\psi_g\rangle^2\delta(E_e - E_g - h\omega). \tag{1.18}$$

The equation 1.18 provides a simple formula to obtain the transition probability per time from an initial eigenstate ψ_g with energy E_g to a final eigenstate $\psi_e^\star$ with energy E_e. [28] In equation 1.18, according to a Dirac-delta function, the transition can occur only if the energy difference between the two states is in resonance with the energy of a photon.

The symmetry and spin rules for the transition can be extracted from the Fermi-golden rule by an application of a dipole approximation. In the approximation, only the first component of H_{int} Taylor development is used for calculation of the formula 1.18. The calculation is in good agreement with experimental results in the case that the ratio of excitation wavelength and molecule size is larger than 10^2. This is appropriate in our experiment as the wavelength is longer than 420 nm, and the size of all pigments is around $\approx$1 Angstrom. The brackets

in equation 1.18 can be overwritten by an application of the long-wave approach of electric field interaction with a molecule as [19, 28]

$$\langle\psi_e^\star|H_{int}|\psi_g\rangle = \frac{im}{h}\left(E_e - E_g\right)\langle\psi_e^\star|\sum_i \vec{r}_i - \sum_j Z_j\vec{R}_j|\psi_g\rangle = \frac{2im\pi}{eh}\left(E_e - E_g\right)\vec{M}_{ge}, \tag{1.19}$$

where $\vec{M}_{ge}$ is an electric transition dipole moment consisting of nuclei component $\vec{\mu}_n = \sum_j Z_j\vec{R}_j$ and electronic component $\vec{\mu}_e = \sum_i \vec{r}_i$. The expression of the electric transition dipole moment can be overwritten with the presumption that the motion of electrons is much faster compared to the motion of atomic nuclei (Born-Oppenheimer approximation) and the wave function ψ_x describing the molecule can be separated into its vibrational, electronic and spinal parts (we neglect rotational component)

$$\vec{M}_{ge} = \int \psi_e^\star\vec{\mu}\psi_g \mathrm{d}\tau = \int \psi_e^{el.s.\star}(r,t)\psi_e^{vibr.\star}(R,t)\left[\vec{\mu}_n + \vec{\mu}_e\right]\psi_g^{vibr.}(R,t)\psi_g^{el.s.}(r,t)\mathrm{d}\tau. \tag{1.20}$$

The orthogonality of the ground and the excited electronic wave functions and their separation into non-interacting subsets leads to the modification of equation 1.20

$$\begin{aligned}\vec{M}_{eg} = &\langle\psi_g^{vibr.\star}|\mu_n|\psi_e^{vibr.}\rangle\langle\psi_g^{el.\star}|\psi_e^{el.}\rangle\langle\psi_g^{s.\star}|\psi_e^{s.}\rangle + \\ &+\langle\psi_g^{vibr.\star}|\psi_e^{vibr.}\rangle\langle\psi_g^{el.\star}|\mu_e|\psi_e^{el.}\rangle\langle\psi_g^{s.\star}|\psi_e^{s.}\rangle = \\ &= \langle\psi_g^{vibr.\star}|\psi_e^{vibr.}\rangle\langle\psi_g^{el.\star}|\mu_e|\psi_e^{el.}\rangle\langle\psi_g^{s.\star}|\psi_e^{s.}\rangle,\end{aligned} \tag{1.21}$$

where the first component is zero due to $\langle\psi_g^{el.\star}|\psi_e^{el.}\rangle = 0$.

In the equation 1.21, the three independent terms lead to different selection rules. The first term ($\langle\psi_g^{vibr.\star}|\psi_e^{vibr.}\rangle$) is called the Franck-Condon factor, which modulates the transition probability by the overlap of vibrational wave functions. [29] Thanks to the Franck-Condon principle, the absorption of a photon can be seen as a vertical process. The last term ($\langle\psi_g^{s.\star}|\psi_e^{s.}\rangle$) allows transition only between the states with the same multiplicity. And finally, the intermediate term ($\langle\psi_g^{el.\star}|\mu_e|\psi_e^{el.}\rangle$) results in the orbital rules determined by symmetry characteristics of the transition moment and the involved states. [30] The symmetry rules are different for each class of a pigment and will be discussed in the next subsections.

Several major pigments classes are present in the photosynthetic organisms. [2] The most common light-harvesting pigments are chlorophylls and bacteriochlorophylls, which are related to porphyrins and carotenoids. Other classes are water-soluble phycobilins of cyanobacteria and rhodophytes. The phycobilins are tetrapyrroles with an open ring and they will not be discussed further as they are not present in the LHCs we studied in this work.

1.3.1 Chlorophylls and Bacteriochloropylls

Chlorophylls (Chls) and bacteriochlorophylls (BChls) are the main light-harvesting pigments in most of the LHCs of plants, algae and photosynthetic bacteria. Both are cyclic planar tetrapyrrole molecules with the fifth isocycle ring and functional groups attached to the main cycle. [2] Usually, a magnesium ion is

located in the centre of a tetrapyrrole coordinated to four nitrogen atoms. The ring around its circumference forms an extensive conjugated system, which is the reason for their unique spectroscopic properties. [21] Their absorption spectra are divided into two main regions called Soret bands around $\approx 380-450$ nm and Q-bands around $\approx 500-800$ nm. [2] Each tetrapyrrole absorption spectrum can be assigned to a different symmetry point group according to the spectral properties such as the number of absorption bands or their positions. The absorption spectra of Chls and BChls are derived from the spectral properties of metal-porphyrins (M-porphyrins), which are chemically related to them. The shape of UV/VIS absorption spectra of M-porphyrins (point group symmetry D_{4h}) can be explained by Gouterman's four-orbital model, which is based on Hückel's theory. [31, 32]

In general, the four-orbital model provides four possible transitions (x polarized transitions $a_{2u} \rightarrow e_{gx}$, $a_{1u} \rightarrow e_{gy}$ and y polarized transitions $a_{1u} \rightarrow e_{gx}$, $a_{2u} \rightarrow e_{gy}$). This is in agreement with metal free porphyrins with their D_{2h} symmetry. However, the situation is changed in M-porphyrins due to their higher symmetry ($D_{2h} \rightarrow D_{4h}$). [33] According to Gouterman's model, the two LUMO orbitals of the M-porphyrin molecule are degenerated, which makes possible only two transitions to an excited state ($a_{2u} \rightarrow e_g$ and $a_{1u} \rightarrow e_g$). [33] The transition occurring of shorter wavelengths is referred to as the Soret band and it is strongly allowed. The second transition occurring in the long wavelength region is referred to as the Q-band. In fact, the Q-band transition is forbidden. The strong configuration interaction due to a near degeneration of the states results in the destructive configuration of transition dipole moments in the case of the Q-band transition. However, due to a vibronic coupling with the Soret transition, the Q-band yields at least a weak intensity. [31, 32]

In figure 1.3 is shown the model schema of M-porphin and the energy level changes towards M-chlorin and M-bacteriochlorin with the assignment of different transitions between electron energy levels to different spectral bands. The changes of the absorption spectra (and split of energy levels) are directly related to the changes of red marked double bonds in figure 1.3. [31]

The high D_{4h} symmetry of M-porphins and their derivatives is lost by reduction of pyrrolic rings B or D (see 1.3). The oxidation of one double bond in the D pyrrole ring of chlorins and two opposite double bonds in the case of bacteriochlorins leads to reduced symmetry. The lower symmetry splits the Q and Soret bands into two pairs with polarization x and y. The point symmetry groups C_{2v} and D_{2h} describe the symmetry of M-chlorins and M-bacteriochlorins, respectively. In the case of M-chlorins, the reduction of the double bond, which stores a lot of electron density, destabilizes the molecular orbitals. The result of such a destabilization is in a blue shift of the Soret band due to an increase of the HOMO-LUMO energetic gap and a red-shift of the Q_y band, which is intensified in response to a higher oscillator strength of the excited states. [31] The situation is very similar in M-bacteriochlorins. Moreover, an intense Q_y absorption arises at lower energy in M-bacteriochlorins due to the longer conjugation along the y-axis than the x-axis in the macrocycle. [31]

Biosynthesis of chlorophylls and bacteriochlorophylls starts with a condensation of two molecules of δ-aminolevulinic acid into porphobilinogen. [2] In the next step, four porphobilinogens create a porphin ring in uroporphyrinogen and then stabilize the conjugated system by transformation into protoporphyrin IX

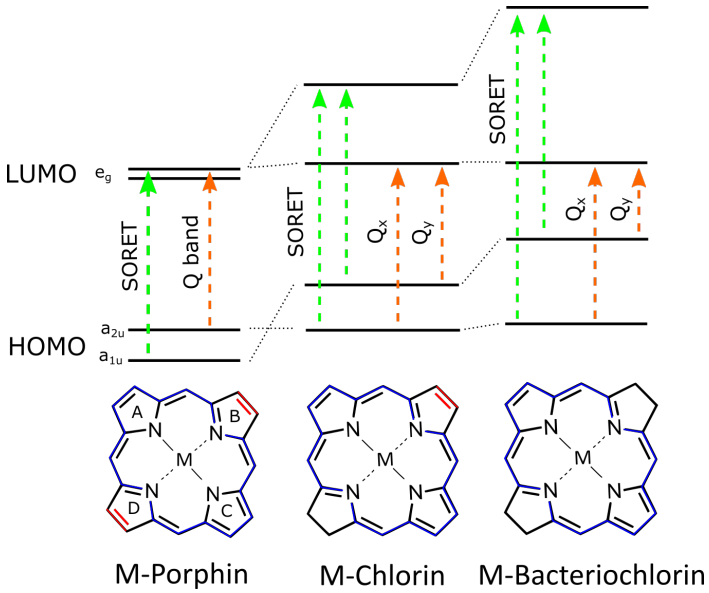

Figure 1.3: Diagram of energy levels and transitions of M-porphin, M-chlorin and M-bacteriochlorin.

by a modification of side chains. During the activity of Mg-chelatase, a metal ion is built into the ring and other enzymes like methyltransferase and vinylreductase activities modify Mg-protoporphyrin IX to NADPH:protochlorophyllide with the fifth isocycle. Subsequent adjustments of side chains and reductions of pyrrole rings lead to the differences between chlorophylls and bacteriochlorophylls. [2] There are some minor differences among the biosynthetic pathways in different organisms, which are more deeply described in [2]. However, most of the steps are similar. The next subsections will discuss tetrapyrrole pigments found in LHCs studied in the experimental section. The spectral properties are taken mainly from [34], where the pigments were dissolved in pyridine.

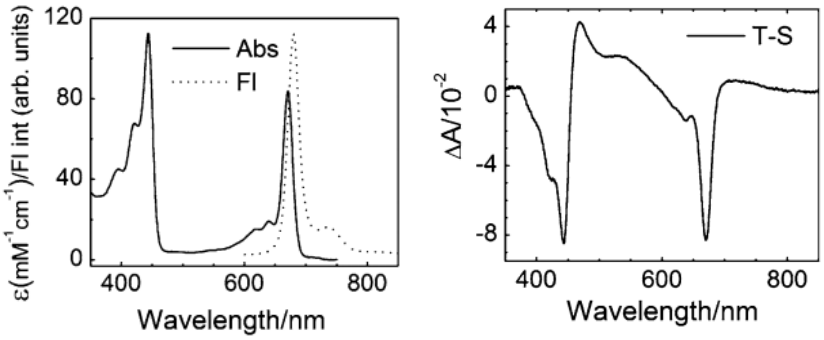

Figure 1.4: (Left) The steady-state absorption and emission spectra of chlorophyll *a*. (Right) The triplet minus singlet spectrum of chlorophyll *a* at 100 ns. The spectra are taken from [34]

Chlorophyll *a*

Chlorophyll *a* (Chl *a*, figure 1.5) is present in all known photosynthetic eukaryotic organisms and cyanobacteria. Also, green sulfur bacteria or heliobacteria possess a small amount of Chl *a* in the RCs. [2, 31] The steady-state absorption spectrum of Chl *a* at 77 K has two main bands with two maxima at ≈440 nm (Soret band) and at ≈670 nm (Q_y band). The several weaker bands between them are assigned to a vibronic structure of the Q_y or Q_x bands. [9, 34] The fluorescence spectrum of Chl *a* at RT has a major peak at 677 nm and a side band at 737 nm. [34] The previously published lifetime of Chl *a* fluorescence and 5.7 ns at 77 K.[34, 9] The transient spectrum at 100 ns has two strong negative bands in place of Soret and Q_y bands corresponding to the ground state bleaching and positive band around 470 nm, which is associated to triplet-triplet absorption. Therefore, the transient spectra are sometimes called triplet minus singlet (T-S) spectra .

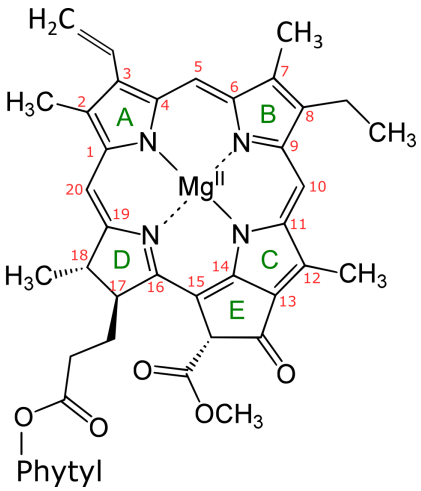

Figure 1.5: Molecular structure of chlorophyll *a*. The figure is taken from [35] and modified to the structures of the other chlorophylls.

Representative steady-state absorption, emission and T-S spectra are shown in 1.4. For the spectra of the other Chls and BChls, see [34].

Chlorophyll *b*

Chlorophyll *b* (Chl *b*, figure 1.6) is the accessory light-harvesting pigment in eukaryotic organisms and prochlorophytes. It differs from Chl *a* structure in the formyl group attached to C_7 instead of the methyl group. [2, 31] The maximum of the Soret band is situated at ≈ 470 nm and the Q_y band is blue-shifted to ≈ 655 nm. [34] The lifetime of fluorescence of Chl *b* is 3.2 ns. The fluorescence spectrum of Chl *b* possesses a major band with the maximum at ≈ 660 nm and its vibronic band with the maximum at ≈ 721 nm. The T-S spectrum has a positive absorption band of triplet-triplet absorption at 510 nm.

Chl *a* and Chl *b* both belong to the chlorin class.

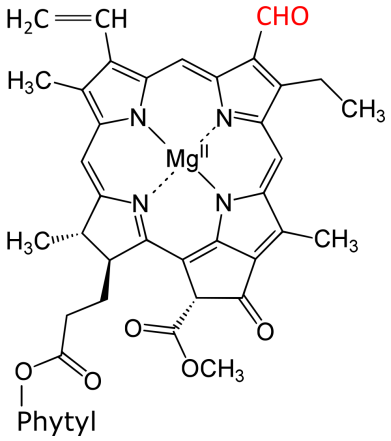

Figure 1.6: Molecular structure of chlorophyll *b*. [35]

Chlorophyll c_2

Contrastingly to the previous chlorophylls, chlorophyll c_2 (Chl c_2, figure 1.7) has a pyrrole ring D with double bond and, therefore, it belongs to the porphin class. The pigment is found in marine algae like diatoms or *Dinoflagellates*. [2] Three types of chl c_{1-3} with different side chains attached to the pyrrole ring B are known from eukaryotic chromophytic algae. In Chl c_2, C_7 binds a methyl group and C_8 binds an ethyl group. Also, Chl c_2 lacks an isoprenoid tail. [2, 31] The maximum of the Soret band of Chl c_2 is at ≈457 nm and Q-bands x and y appear at ≈582 nm and ≈635 nm, respectively. The fluorescence lifetime is 5.9 ns with the main band maximum at ≈640 nm and its vibronic band at ≈700 nm. As a porphyrin type molecule, the absorbance of the Soret band is much higher than the Q_y band. T-S spectra of Chl c_2 has a triplet-triplet positive band with the maximum at ≈490 nm. [34].

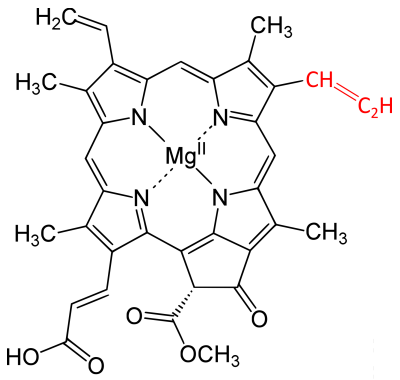

Figure 1.7: Molecular structure of chlorophyll c_2. [35]

Bacteriochlorophyll *c* and *a*

Bacteriochlorophyll c (Bchl c) is a main light-harvesting pigment of green sulfur and non-sulfur bacteria and chloroacidobacteria. [2] The pigment belongs to the chlorin class. The absorption spectrum of Bchl c is very similar to that of Chl a with the Soret band with a maximum at ≈445 nm and the Q_y band with a maximum at 670 nm. Fluorescence decays with a lifetime of 6.7 ns with the maximum at ≈674 nm. The maximum of triplet-triplet absorption of Bchl c is observed at ≈441 nm. [34] Bacteriochlorophyll a (BChl a) can be found for example in purple photosynthetic and green bacteria. The steady-state absorption spectrum of BChl a shows the maxima of the Soret, Q_x and Q_y bands at ≈374 , ≈613 and ≈781 nm, respectively. The maximum of triplet-triplet absorption is at 400 nm. [34]

1.3.2 Carotenoids

Carotenoids are naturally occurring pigments. They can be divided into two classes: carotenes, which are composed of carbons and hydrogens, and xanthophylls containing oxygen. Carotenoids are widely spread molecules with hundreds of members with different structural features, but there are only around 50 carotenoids involved in photosynthesis. [2] They are built from several isoprenoid units in a linear chain sometimes terminated with a ring on one or both sides. Half of the central chain has an opposite orientation of the isoprenoid units. Usually, the central chain has a point reflective symmetry. [2] The colour of carotenoids is directly connected to their extended conjugated system, located in the central

chain. [36] All the photosynthetic organisms, some funghi and bacteria synthesize carotenoids from fats and other building blocks. The initial step of biosynthesis of carotenoids is condensation of eight isoprenoid units into two head-to-tail linked parts, which are connected together tail-to-tail. The initial process is followed by desaturation, which prolongs the conjugated system of double bonds and shifts the absorption spectra of the carotenoids into the visible spectral region. The next two stages of the biosynthesis - cyclization of the central chain endings and an attachment of functional groups - depend on the carotenoid type. [37]

The structure of a steady-state absorption spectrum is dominated by transition from the S_0 state of carotenoid to the S_2 state. The S_2 state quickly relaxes to the S_1 state by internal conversion, with lifetime depending on the length of the conjugated system. The S_1 state then usually relaxes to the S_0 state by a non-radiative path in a picoseconds time. [38, 39] The excited states of carotenoids decay surprisingly quickly compared to the tetrapyrrol pigments and it must be reflected during the light-harvesting. Both excited singlet states, S_2 and S_1, can serve as an energy donor during the light-harvesting. [40] The fluorescence from both excited states is usually very weak. [38] The electron transition from the S_0 state to the S_1 state is forbidden by symmetry selection rules. Even if the carotenoids with side chains and functional groups do not belong to any symmetry point group, the transition is forbidden as in the case of polyenes molecules with C_{2h} symmetry; see figure 1.8. Polyenes ground state belongs to an irreducible representation $1^1A_g^-$, the S_1 state is denoted as 2^1A_g and next singlet state (S_2) is represented by $1^1B_u^+$. Simultaneously, a transition dipole moment is transformed as the Cartesian coordinates. Therefore, the transition dipole moment in the C_{2h} symmetry point group belongs to A_u (z) and B_u (x and y) representations. The symmetry selection rules for polyenes transition can be easily calculated by multiplication of characters of chosen irreducible representations due to the C_{2h} symmetry point group having order equal to 4 ($\Rightarrow$ all the irreducible representations have dimension equal to 1) [41, 42]:

C_{2h}	E	C_2	i	σ_h		
A_g	1	1	1	1	R_z	x^2, y^2, z^2, xy
B_g	1	−1	1	−1	R_x, R_y	xz, yz
A_u	1	1	−1	−1	z	
B_u	1	−1	−1	1	x, y	

Figure 1.8: Table of characters for point group C_{2h}.

$$S_0 \longrightarrow S_1 : \ \langle S_0|\overrightarrow{d_m}|S_1\rangle = \langle A_g|(B_u, B_u, A_u)|A_g\rangle = (B_u, B_u, A_u), \tag{1.22}$$

$$S_0 \longrightarrow S_2 : \ \langle S_0|\overrightarrow{d_m}|S_1\rangle = \langle A_g|(B_u, B_u, A_u)|B_u\rangle = (A_g, A_g, B_g). \tag{1.23}$$

The equation 1.22 shows that the transition $S_0 \longrightarrow S_1$ is not allowed by symmetry selection rules, because none of the component of the transition dipole moment is transformed like A_g. On the contrary, the equation 1.23 illustrates that the transition to the S_2 state of polyenes is allowed by symmetry selection rules. Experimental results show a good agreement between the spectroscopic properties of carotenoids and the model for linear polyenes.

Recently, Fiedor et al. [43] were looking for a different reason for why the transition from the S_0 state to the S_1 state is forbidden. In the paper, the authors discuss the absorption spectra of carotenoids with respect to their side chains

and isomerization. The absorption spectra of the carotenoids prove that the $S_0 \longrightarrow S_1$ transition is forbidden in spite of the lower symmetry of carotenoids with nonlinear π-electron conjugated system. For example, cis-β-carotenes with formally allowed transition to the S_1 state according to their "real" symmetry do not exhibit any $S_0 \longrightarrow S_1$ absorption. Moreover, the "real" symmetry of the carotenoids is manifested in their IR and Raman spectra. Therefore, another mechanism was proposed which reflects deformation of the carotenoid molecule in the S_1 state making Franck-Condon factors for vertical transition negligible because of the displacement along the vibrational coordinates. [43]

Almost all LHCs contain several different types of carotenoids including the three antennas discussed in the next sections. The main function of carotenoids is photoprotection, and the other functions include light-harvesting and structural stabilization of the protein complex. Carotenoids are attached to well defined positions in LHC, which enables them to interact with nearby chlorophylls and consequently regulates energy flow through LHC. [44] The advantage of light-harvesting by carotenoids is their high efficiency in the blue-green spectral region ($400-550\,\mathrm{nm}$). The higher absorbance of carotenoids than tetrapyrrole pigments in the visible spectrum around $\approx 500\,\mathrm{nm}$ is used by some of the sea algae in adaptation to different conditions of spectral irradiantion under sea level. [2]

The energy absorbed by carotenoids is transferred to chlorophylls or bacteriochlorophylls in the same antenna with a transfer rate faster than the carotenoid relaxation to the ground state.

$$\mathrm{Car}(S_0) + h\nu \longrightarrow \mathrm{Car}(S_2), \tag{1.24}$$

$$\mathrm{Car}(S_{2/1}) + \mathrm{Chl}(S_0) \longrightarrow \mathrm{Car}(S_0) + \mathrm{Chl}(S_1). \tag{1.25}$$

In the equation 1.24, a carotenoid in the singlet ground state (S_0) is excited by a photon of energy $h\nu$ to the second excited singlet state (S_2), which can directly transfer energy to chlorophylls by the Förster mechanism (e.g. $50-200\,\mathrm{fs}$ from peridinin to Chl *a*). [36, 11, 40] However, the efficiency of the energy transfer from the S_2 state varies among different LHCs. [40] Carotenoids especially, with a shorter conjugation system, use a different pathway: the S_2 state relaxes to the S_1 state by internal conversion, followed by an ET to chlorophyll. For example, in LHCII the ET from $\mathrm{Car}(S_2)$ to Chl $a/b(Q_x)$ is the main path with efficiency $> 70\%$ in the case of luteins, but "only" $10-50\%$ in the case of neoxanthin. [40] The dynamic processes of the S_1 state are strongly dependent on the conjugation length, carotenoid structure and surrounding environment as is

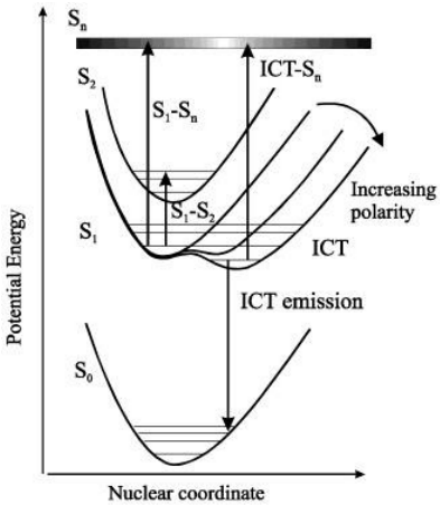

Figure 1.9: Energy levels of peridinin and their dependence on solvent polarity. The figure is taken from [45].

shown in transient absorption spectra and fluorescence measurements. [39] The solvent polarity and polarizability also influence the position of transition to the S_2 state. It should be mentioned that carotenoids may posses other excited states between or in proximity to the S_1 and S_2 states. [45]

Peridinin

The energy level scheme of carotenoids with carbonyl groups includes low-energy intramolecular charge transfer (ICT) state. [47] The ICT state was postulated to explain peridinin absorption spectrum and dynamics, which are strongly affected by solvent polarity. Also, it was suggested that carbonyl groups stabilize the ICT state in polar solvents through interaction with solvent molecules. [45] The S_1 and ICT states differentiability is still a topic of discussion. The quantum mechanical calculations by Vawati et al. and pump-dump-probe spectroscopic experiments on peridinin in methanol show that the S_1 and ICT states are distinct. [36, 48] Oppositely, Shima et al. group published MNDO-PSDI calculations showing that the S_1 and ICT states are identical and their (or its) origin is in a large dipole moment predicted for the S_1 state of peridinin in a solution with different polarity. [49] The ICT state can be also described as the interaction between Frenkel exciton with a localized electron and a hole on one molecule and Wannier-Mott exciton, which describes delocalization of the electron and the hole in bulk. [50, 51]

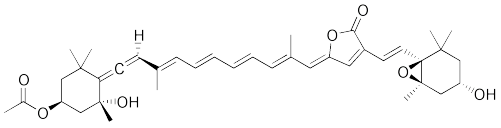

Figure 1.10: Molecular structure of peridinin. [46]

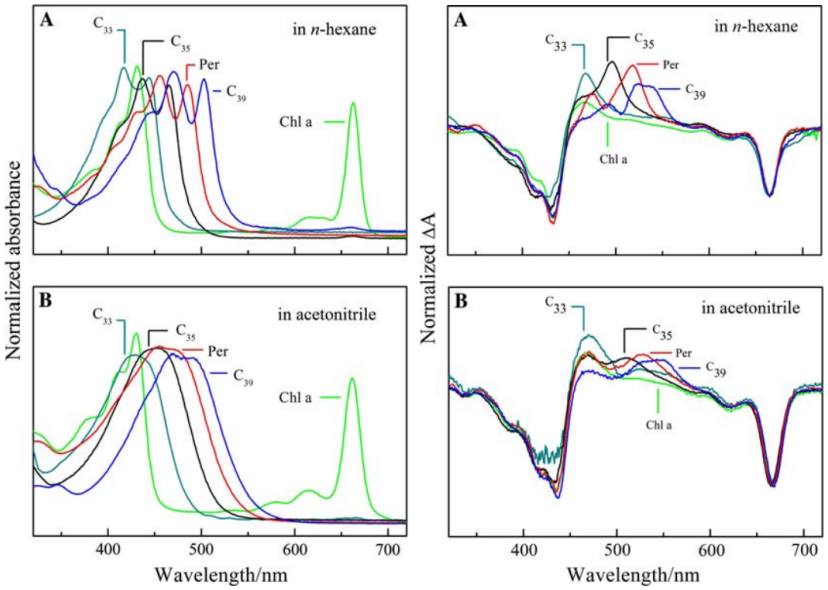

Figure 1.11: (Left) The absorption spectra of peridinin and Chl *a* in non-polar (A) and polar solvent (B). (Right) The triplet minus singlet spectra of peridinin triplets sensitized by Chl *a* in non-polar (A) and polar solvent (B). The figure is taken from [52].

The steady-state absorption spectrum of peridinin is highly dependent on the polarity of the solvent. The structure of absorption spectra in n-hexane (non-polar solvent) is formed by three well-resolved bands, which is typical for carotenoids; see figure 1.11. The vibrational structure is lost in polar solvent like acetonitril. [45, 52] The transient absorption spectrum possesses only one broad band assigned to peridinin ESA at ≈550 nm in a polar solvent. Oppositely, the ESA spectrum of peridinin in a non-polar solvent shows two bands with maxima at ≈470 nm and ≈520 nm. [52] The spectral properties of peridinin dependence on the polarity of solvent is due to the carbonyl group. [45, 53] Zigmantas et al. [45], proposed a model which reflects a complicated structure of the S_1 energy level; figure 1.9. They suggest that the contribution of the ICT state is growing with a rising polarity of a solvent and the singlet ESA absorption at ≈590 nm is from the ICT state. Apparently, the similar situation is observed in triplet-triplet absorption of peridinin. [52]

Lutein, violaxanthin and neoxanthin

Lutein (1.12) and violaxanthin are both xanthophylls located in the light-harvesting complex II (LHC-II) of higher plants. The central position of luteins in LHC (see section 1.5) is essential for the quenching of chlorophyll triplets. Violaxanthin is synthesized from zeaxanthin by epoxidation of the two ending rings. Violaxanthin reverse conversion is involved in non-photochemical quenching (NPQ, see section 1.5) of LHC-II. [55] Also, neoxanthin seems to have its role in NPQ of LHC-II due to the changes of its configuration when LHC-II is in a dissipative state and its strong electronic interactions with the Chl *b* molecules in LHC-II. [6]

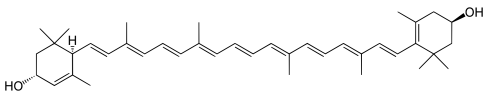

Figure 1.12: Molecular structure of lutein. [54]

The steady-state absorption spectrum of lutein in pyridine yields the main band at 461 nm assigned to $S_0 \longrightarrow S_2$ transition and one side band on each side. The absorption spectrum of violaxanthin in trans isomer form exhibits the main maximum at 456 nm in pyridine. [39] Neoxanthin has the most blue shifted middle band with maximum at 451 nm in pyridine. [39]

β-caroten

The nonpolar *β*-carotene (figure 1.13) is presented as 15-*cis* and trans isomers in chlorosomes and PSI. [57] Trans *β*-carotenes are also involved in energy transfer of CP43 and CP47 antennas in PSII. [57] The absorption spectrum of *β*-carotene consists of three overlapped bands above 400 nm in n-hexane with the middle one at 448 −450 nm corresponding to strongly allowed $S_0 \longrightarrow S_2$. A weak absorption band around 336 nm

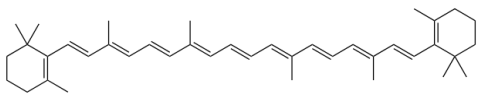

Figure 1.13: Molecular structure of *β*-carotene. [56]

is strongly pronounced in the case of 15-*cis* isomer. The "*cis* band" appears to be indirectly proportional to the $S_0 \longrightarrow S_2$ band, which shows an interaction of the S_2 and S_n states ($n > 2$) depending on the degree of linearity of β-carotene. A simple model based on the splitting of the transition moment into two components is presented in [43] and it shows good agreement with the experimental results. The band broadening in the β-carotene spectrum is due to the β terminal rings, which broaden the distribution of the possible conformation with regards to the conjugated system. [39]

Three light-harvesting antennas studied in the experimental section contain pigment composition of:

- LHC II of pea: chlorophyll *a* and *b*, violaxanthin, neoxathin, lutein [14]
- acpPC of *Amphidinium carterae*: chlorophyll *a* and c_2, peridinin, diadinoxanthin [58]
- chlorosomes of *Chloroflexus aurantiacus*: bacteriochlorophyll *c*, β-carotene, γ-carotene, and OH-γ-carotene glucoside [59]

1.4 Photoprotective role of carotenoids

In low photon flux situations, the population of the S_1 states of Chl and BChl is kept low due to the consumption of the excitation energy by the open RC. However, if the RCs are over-saturated, the excited Chls and BChls have to relax by other pathways, which can lead to the generation of $^1O_2$, which is highly toxic for photosynthetic apparatus.

The S_1 states of Chl and BChl can relax to the ground state by several pathways such as internal conversion, fluorescence or undergoing intersystem crossing (ISC) to the triplet (T_1) states. In general, ISC is forbidden by the spin rules. However, the independent S_1 and T_1 states are only a simplification, and ISC can occur due to spin-spin or spin-orbital interactions, which couple the S_1 and T_1 states and open the transition in certain situations (see Kasha rules and El Sayed rules, [29, 23]). The T_1 states of Chl have the same spin multiplicity as the ground state of molecular oxygen, which can quench them. Therefore, the quenching of T_1 states yields $^1O_2$ with a non-zero efficiency [30]

$$\mathrm{Chl}(S_0) \xrightarrow{h\nu} \mathrm{Chl}(S_1) \xrightarrow{\mathrm{ISC}} \mathrm{Chl}(T_1) \tag{1.26}$$

$$\mathrm{Chl}(T_1) + {}^3O_2 \longrightarrow \mathrm{Chl}(S_0) + {}^1O_2 \tag{1.27}$$

The probability of $^1O_2$ generation is rising with spatial proximity to the RC, where the excitation energy is more easily trapped. [3] Several strategies have been developed by photosynthetic organisms to prevent oxidative damage by dissipation of the gained energy. Carotenoids play a crucial role in these strategies, called non-photochemical quenching of Chl S_1 states (see section 1.5) or direct quenching of Chl T_1 states. In both cases, the proper orientation of carotenoid

and proximity in respect to chlorophylls is highly necessary for efficient quenching. Usually, the specific binding site is provided by interaction of the carotenoid with the protein frame of LHC.

The T_1 state of carotenoid has approximately half the energy of the S_1 state of Chl and, simultaneously, its energy is lower than the energy of the $^1O_2$. Therefore, the T_1 state of carotenoid cannot cause any harm to the complexes. The direct Chl T_1 quenching by carotenoids occurs according to following equation

$$\mathrm{Chl}(T_1) + \mathrm{Car}(S_0) \longrightarrow \mathrm{Chl}(S_0) + \mathrm{Car}(T_1) \tag{1.28}$$

The second mechanism is connected to the direct quenching of $^1O_2$. The $^1O_2$ relaxation paths include heat dissipation, phosphorescence, harmful oxidation of surrounding molecules and energy transfer to other molecules, which is used as another photoprotective mechanism of LHC by carotenoids. The direct quenching of $^1O_2$ is also ensured by the Dexter mechanism of ET.

$$^1O_2 + \mathrm{Car}(S_0) \longrightarrow {}^3O_2 + \mathrm{Car}(T_1) \tag{1.29}$$

The triplet state of carotenoid is later dissipated in the form of heat.

$$\mathrm{Car}(T_1) \longrightarrow \mathrm{Car}(S_0) + \mathrm{heat} \tag{1.30}$$

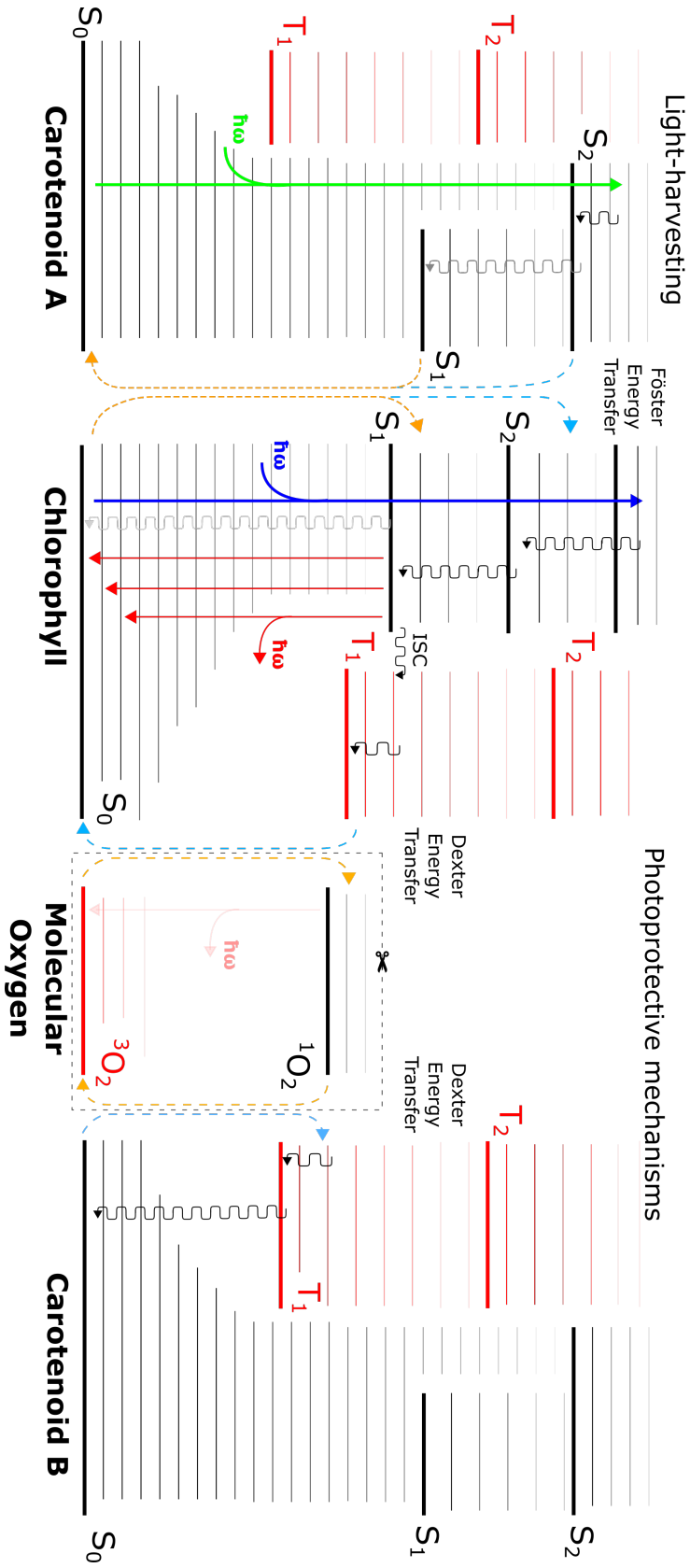

Figure 1.14: Jablonski diagram.

1.5 Light-harvesting complex II of higher plants

The light-harvesting complex II (LHC-II) of higher plants is the most common membrane protein in nature and contains almost all the Chl *b* in plants. [60] LHC-II was identified by Philip Thornber in 1965 as the main light-harvesting antenna of a plant leaf, and since that time it has probably been the most deeply examined LHC. LHC-II is embedded in the lumen part of the thylakoid membrane of the chloroplasts of higher plants. As an accessory light-harvesting complex, it is linked to the RC of photosystem II (PSII) via minor Chlorophyll a/b Proteins (CP29, CP26 and CP24) and other inner antennas, which funnel excitation energy from LHC-II to the RC. [2] However, the position of LHC-II may vary in the case of a disbalance of power supply between PSI and PSII. LHC-II can be detached from PSII through phosphorylation of the threonine residue near the N-terminus in Lhcb1 and Lhcb2 polypeptide components of LHC-II by a specific kinase and subsequently, it is transferred to the lamellar area close to PSI. [60, 55] The process is called "state transition." [61] Carotenoids in LHC-II also play a significant role in ET regulation by Chl triplet quenching and non-photochemical quenching (NPQ). [14, 60] Therefore, the role of carotenoids in the LHC-II structure is crucial.

The LHC-II structure was first determined by Kühlbrandt et al. at 6 Angstroms resolution by electron crystallography. [62] Specifically, three α-helices and 15 chlorophylls were resolved in one of the LHC-II monomers. The LHC-II sample studied in our spectroscopic experiments was extracted from a pea. The structure of LHC-II of the pea was determined by the same group with 2.54 Angstroms resolution by an X-ray crystallography of stacked two-dimensional crystals. [55] The structure is shown in figure 1.15. LHC-II has a trimeric composition with three different polypeptides - Lhcb1, Lhcb2 and Lhcb3. The sequence similarity among Lhcbs is around 77%. [60] Each LHC-II monomer of the pea consists of three transmembrane α-helices, which form the frame for the complex. In addition, two short amphiphilic helices on the lumenal side were found. One monomer binds fourteen molecules of chlorophyll, four carotenoids and two lipids. The occupied lipids are digalactosyl diacylglycerol and phosphatidyl glycerol, which are involved in the filling of a hydrophobic cavity and the structure stabilization of the trimer, respectively. Chl *a* and Chl *b* are found in LHC-II in a ratio of 4:3. The pigment core of an LHC-II monomer consists of six central Chls *a*, the position of which is also conserved in the LHC-II of spinach. [63] The light-harvesting is maximized by the

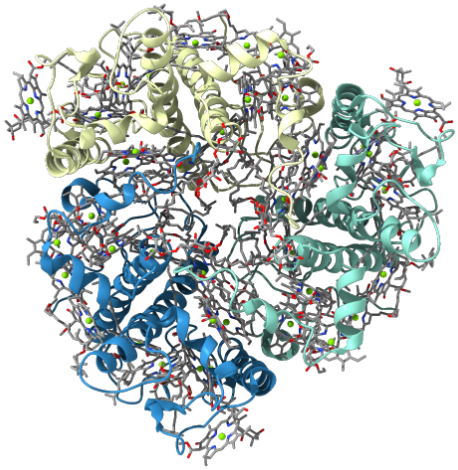

Figure 1.15: The crystal structure of trimeric LHC-II. Figure is taken from [55].

different orientation of Q_y dipole moments of all Chls. [55] Chls *b* are located in the peripheral areas of LHC-II, and they transfer all gained energy to the central Chls. [64, 65, 66]

Other pigments included in the LHC-II monomer are carotenoids: two luteins, neoxanthin, and violaxanthin. [55] Their structural role in the LHC-II assembly was studied through LHC-II mutations, for example in [67]. Two luteins are situated in the centre of LHC-II, opposite to the other two xanthophylls located in the peripheral areas. Neoxanthin in a *cis* isomer form is located on the edge of the LHC-II monomer, sticking into the lipid bilayer. [68] Besides having a structural function, the photoprotective role of neoxanthin for chlorophylls was suggested. [6] The violaxanthin position is at the interface of monomers and is involved in NPQ. [60, 55] Luteins are in close van der Waals contact with Chl 2 and 5 (see figure 1.16) and have the important role of Chl triplet quenching. [14] The close contact causes a red shift of Chl 2 and 5 absorption spectra. The red-shifted Chls apparently play a central role in ET to the RC. [65] They can also obtain energy from the S_2 states of lutein due to the close contact and appropriate orientation of lutein in respect to Chls. [40] However, the light-harvesting function of carotenoids in LHC-II is less important compared to Chls. [55]

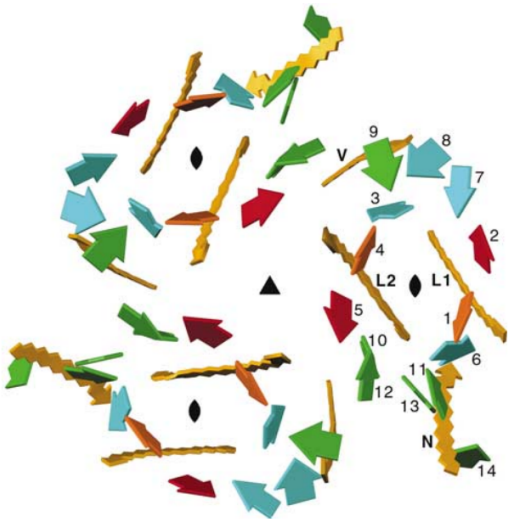

Figure 1.16: Orientation of pigments in LHC II copied from [55]. Squared arrows in the direction of the Q_y dipole moment are assigned to chlorophylls, and yellow arrows in the direction of C1-C24 are assigned to carotenoids.

LHC-II belongs to a large Lhc superfamily with other light-harvesting antennas like minor LHC CP(24, 26,29) of PSII, PS I antenna complexes Lhca(1-4) and the acpPC antenna. [60, 69] The superfamily sequence identities among the members are between $25 - 80\%$. [60]

In LHC-II, the generation of harmful $^1O_2$ from the triplet states of Chl is prevented by the processes involving carotenoids like chlorophyll triplets quenching or NPQ. The central position of luteins and their overlap of π orbitals with two energy-trapping Chl is predetermining for the triplet quenching by the Dexter ET mechanism. In the works of Peterman et al. [8] and Mozzo et al. [14], the generation of Chl triplets in LHC II was studied by transient spectroscopy at room temperature and at very low temperatures ($4 - 77\,\mathrm{K}$) on a microsecond timescale. The experimental results at RT measurements and in the presence of oxygen show two components ascribed to the decay of carotenoid triplets with a lifetime around $\approx 2\,\mu\mathrm{s}$ and $\approx 4\,\mu\mathrm{s}$. [14, 8] The slower component shows a red-shifted triplet ESA band at 518 nm compared to the faster component with the ESA band at 504 nm. Under anaerobic conditions, the two components could not

be distinguished. Mozzo et al. probed several mutants of LHC-II with a different carotenoid composition by transient spectra measurements. These experiments mainly show the involvement of luteins in the quenching of Chl triplets, whereas the position of neoxanthin is related to the oxygen accessibility of one of the luteins. [14] Low-temperature measurements at 77 K show one component with a 12 μs lifetime assigned to the decay of carotenoid triplets and a long-lived $\approx$ ms component assigned to the Chl triplets.

The NPQ mechanism involving the Xanthophyll cycle induces the adaptation of higher plants to high light stress. The whole process consists of two components, which can be activated in seconds and minutes, respectively. [55] The fast component seems to be independent of the Xanthophyll cycle and is related to the rapid drop in pH and to the activity of the PsbS protein. [70, 60] One of the proposed mechanisms of the slow component of NPQ lies in dissipation of energy from the S_1 state by ET to zeaxanthin, which is converted from violaxanthin through antheraxanthin. [61, 55] The mechanism is possible due to the lower position of the S_1 state of zeaxanthin compared to the Q_y state of Chl *a*. Moreover, zeaxanthin is less polar without one of the epoxy groups, which results in a lower repulsive force to the nearby Chl 9. [55] The accepted energy is then dissipated as heat. Oppositely, the S_1 state of violaxanthin should have higher energy than the S_1 state of Chl. The NPQ molecular process is still a topic of discussion, and some papers undermine the necessity of violaxanthin transformation in this process. [6, 7]

As one of the main widespread light-harvesting complexes, LHC-II is highly studied for its photoprotective properties, and it will be compared with acpPC in experimental section.

1.6 The acpPC complex of *A. carterae*

Chlorophyll a-chlorophyll c_2-peridinin-protein-complex (acpPC) is a major membrane-bound intrinsic light-harvesting antenna of the toxic *Dinoflagellate A. carterae*, which is a part of marine plankton. [12] *A. carterae* can be found in coastal bays and estuaries. [71] *Dinoflagellate A. carterae* also possesses a different type of light-harvesting complex, a peridinin-chlorophyll *a*-protein (PCP), which is a water-soluble light-harvesting antenna with the xanthophyll peridinin as the primary light-harvesting pigment. [13] PCP differs from other antennas by a high efficiency of photoprotection, even at low temperature. [13] Both antennas can be found in different forms, probably due to the adaptation to different light conditions under sea level, which are caused by the absorption of water and other surrounding plankton; see figure 1.17. [72] Therefore, the antennas use carbonyl containing peridinin, which absorbs the remaining green light in the spectral region of 450 $-$550 nm.

Purified acpPC from thylakoids is an 18 $-$19 kDa polypeptide unit. [69, 72] The precise structure of acpPC is still unknown. The pigment composition of acpPC has been presented in several papers with different results, probably due to photoadaptation. Early work by Hiller et al. [74] specified the pigment composition of acpPC to 7 Chl *a*, 4 Chl c_2, 12 peridinins and 2 diadinoxanthin per monomer. However, the composition is probably overestimated in the number of carotenoids. [11, 9] The ratio of carotenoids to chlorophylls should probably

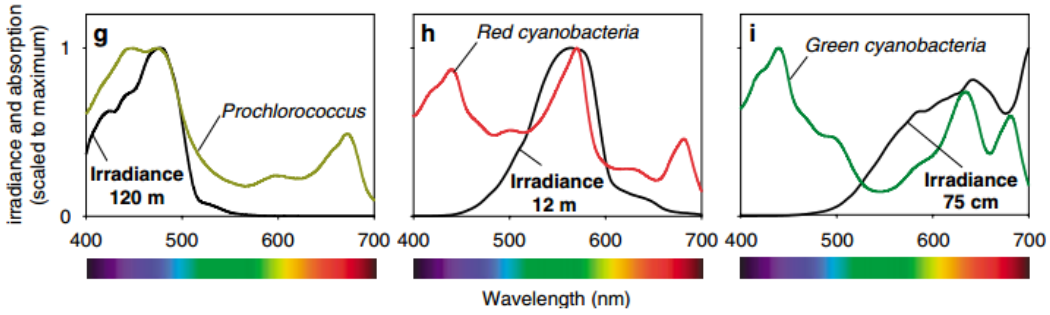

Figure 1.17: Underwater light spectra measured in the subtropical Pacific Ocean (black lines). Spectra of different marine photosynthetic active organisms, which show their adaptation to light conditions. The figure is taken from [73].

be closer to one. [11] In the article [9], Niedzwiedzki et al. show the absorption spectra of individual pigments and acpPC of *Symbiodinum* at 77 K. The spectra were used for determination of the acpPC monomer pigment composition through spectral deconvolution. The result is 4 Chl *a*, 6 Chl c_2, 6 peridinins and 1 diadinoxanthin. The analysis made by Niedzwiedzki et al. shows two spectrally-shifted Chl *a* spectra belonging to two pairs of Chl *a* with a Soret band at 438 and 432 nm, three spectrally-different forms of Chl c_2 and the same for peridinin. [9]

The pigment composition of acpPC is different from that of LHC-II and their overall homology is lower than 30 %. However, the core structure of both antennas is homologous with $\approx$ 44 % of identities and positive substitutions. [69] Also with a high certainty, the acpPC polyprotein structure forms three transmembrane helices, the same as in the case of LHC-II. [69] It was suggested that the same frame is common in different classes of LHCs. [74, 75]. Several papers suggested a structural model for acpPC with a conserved bindings position for five Chls *a* based on the comparative sequential analysis of the core transmembrane polypeptides from LHC-II. [69, 75, 76] The two internal binding sites of luteins in LHC-II should also be conserved and probably occupied by peridinins in the acpPC antenna. [69] The positions of neoxanthin and violaxanthin are most likely not preserved. It was proposed that some Chls *a* in LHC-II were replaced by carotenoids in acpPC. [69]

An early study of acpPC [74] shows a direct energy transfer from Chl c_2 (1.4 ps) or peridinin to Chl *a* immediately after the excitation. [11, 69] The light-harvesting pathway uses ET from peridinin ICT (75 −50 %, 2.6 ps or 200 ps), S_2 (<150 fs) and a hot ICT (360 fs) states. [11, 40, 58] Niedzwiedski et al. [9] show two subpopulations of peridinins with an efficient transfer to Chl *a* in acpPC of *Symbiodinum* (1.5 −1.8 ps and 12 ps) at 77 K. The observed ET from the S_2 state was minimal. Chl *a* transfers the excitation energy through singlet-singlet ET to the chlorophyll *a* with the lowest energy in $\approx 10 - 100$ ps. At late nanosecond times, the only contribution to the TA spectra originates from Chl *a*. Similar kinetics were measured in PCP antenna. [9] However, the packaging of the pigments seems to be higher in PCP antennas. [9] The differences among antennas show the importance of the surrounding protein environment influencing the excited state dynamics of LHC.

Oppositely to the peridinin, diadinoxanthin shows no involvement in singlet energy transfer. [11] Diadoxanthin is proposed to have a photoprotective role

in a NPQ process through de-epoxidation to diatoxanthin. [77] Except for the light-harvesting function, the peridinin photoprotective role was reported through the quenching of Chl *a* triplets [69], resulting in two differing carotenoid triplet domains surrounded by different protein environments. Niedzwiedzki et al. also present a kinetic trace of acpPC recorded at 680 nm (Chl *a* emission) and at 77 K. The kinetic trace shows two decays with lifetimes of 150 ns and 2 μs. [9] The shorter lifetime was interpreted as being due to the Chl *a* triplet state, which is ineffectively quenched by the ground state of peridinin ($\approx$ 7%). [9] Also, the direct $^1O_2$ quenching was proposed as one of the photoprotective mechanisms of acpPC. Peridinin photoprotective ability was also studied in PCP proteins, where the quenching of chlorophylls is highly efficient. [13]

In 2015, Kvičalová et al. published a study [12] about the photoprotection and energy pathways of acpPC at RT and compared it to PCP. This work is a cornerstone of our measurements on acpPC at low temperatures. TA spectra show a $\approx$5 ns decay of excited states of Chl *a* and its replacement by the signal of carotenoid triplet states [12], which consist of negative carotenoid ground state bleaching (GSB) and three positive bands ascribed to excited state absorption (ESA). Two of them were assigned to carotenoid triplet ESA. They are formed by a sharp band with maxima at 470 nm and 505 nm. Similar bands were resolved in LHC-II. [14, 8] The analysis of TA spectra at aerobic conditions by decay associated spectra (DAS, see chapter 2.2.2) provided two components with different lifetimes. The faster component with a lifetime of 5.5(6) ns was caused by ET from the singlet state of Chl *a* to the triplet state of carotenoid via the triplet state of Chl *a*. The slower component of DAS had a lifetime of $\approx$2.4 μs, and its shape depended on the excitation wavelength. [12] The rest of the component formed a mirror image to the fast component with a broad band around 555 nm, which is due to the triplet ESA of peridinin in a polar environment. The other sharp positive ESA bands (470 , 507 nm) are ascribed to the triplet states of diadinoxanthin or peridinin in the non-polar environment. [69, 12] Kvíčalová et al. suggest that peridinins in two different environments, or peridinin and diadinoxanthin, are responsible for Chl triplet quenching. No accumulation of the triplet states of Chl *a* was observed. Simultaneously, it was suggested that the T_1 state populated by ISC is immediately quenched by carotenoids. The lifetime of triplet Chl was proposed to be even shorter than 0.1 ns, using kinetic calculation analysis. The previously mentioned Chl *a* triplets observed by Niedzwiedzki et al. [9] in *Symbiodinium* seem to be in contradiction to the results reported by Kvíčalová et al. However, the two species of algae can have slightly different compositions of acpPC antenna, or the low-temperature measurement can be responsible for generation of the Chl *a* triplet population. The temperature dependency is supported by the observation of Chl *a* triplets in acpPC complex from *A. carterae* at 77 K revealed by ODMR and EPR spectroscopy. [69]

The results highlight that particular consideration should be given to triplet-triplet ET by the Dexter mechanism, responsible for the (in)efficiency of Chl *a* quenching at a low temperature.

1.7 Chlorosomes of *Chloroflexus aurantiacus*

Chloroflexi (Clf.) - filamentous anoxygenic phototrophs, also known as green non-sulfur bacteria - contain unique light-harvesting complexes called chlorosomes, which have a very distinct structure compared to the previously discussed LHC-II and acpPC. [78] Their main light-harvesting pigments are bacteriochlorophylls (BChls) situated inside a pocket formed by proteins. BChls aggregate in thousands into lamellar structures by the interaction between hydrophobic esterifying alcohols of BChls from adjacent layers. [78] The arrangement of pigments supports strong exciton coupling. [79, 80] Chlorosomes are believed to be the most efficient antennas in nature. In our experiments, the chlorosomes of *Clf.* will be compared to the previously mentioned LHCs.

The composition of *Clf.* chlorosomes in dry weight is Bchl *c* (50%), proteins (30%), lipids (10%), carotenoids, quinones and Bchl *a* (5%) [82]. Bchl *c* can aggregate into large assembles due to the presence of a hydroxy group attached to asymmetric $C3^1$ and the absence of a methoxycarbonyl group at $C13^2$. The intramolecular coordination of the central ion of one BChl to the hydroxy group of a second BChl seems to be important in the formation of the aggregate. [78] Moreover, according to the prevailing opinion, the hydrogen bond connects the hydroxy group of the second BChl and the keto group of a third BChl. [83] The importance of the hydrogen bond lies in the stabilization of the Q_y transition dipole moments, which enables the strong exciton coupling. The whole aggregate is stabilized by π-π stacking interactions. [38] Oppositely, BChls *a* are not part of the aggregate and are situated in a pigment-protein complex within the baseplate. The carotenoids are located inside the chlorosomal protein pocket near to BChls *c* or surrounding BChls *a* in the baseplate. The number of carotenoids inside chlorosomes depends on the light and temperature conditions during the growth phase. For example, high-light conditions cause an increase of the carotenoid fraction in *Clf.* The composition of carotenoids inside the chlorosomes of *Clf.* consists mainly of β, γ-carotene and their derivatives with β-ring. [38, 84] The planar conjugated systems of β-ring of carotenoids and conjugated systems of BChl *c* most probably interact by π-π interactions, which support the electronic coupling of both pigments. The interaction plays a significant role in photoprotection by the quenching of BChl triplets and ET from the S_2 state of carotene to BChl *c*. [85] The amphiphilic quinones inside the chlorosomes of *Clf.* are menaquinones-10 (1:10 to BChl *c*). Nevertheless, their function is not known, and they are

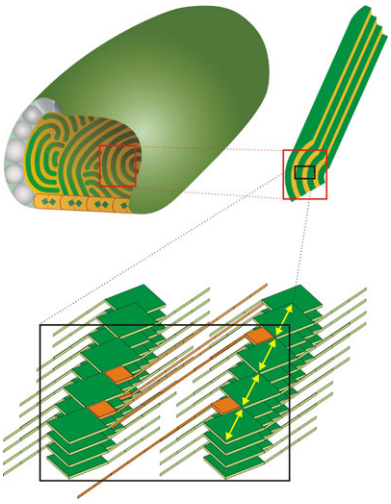

Figure 1.18: Schema of chlorosomes with detail on the aggregation of BChl pigments in the lamellar structure. The figure is taken from [81].

probably not involved in excitation quenching like in *Chlorobi.* [86] Lipids are represented mainly by glycolipids and a smaller amount of phospholipids. In the case of *Clf.*, the chlorosomes are directly linked to the cytoplasmic membrane. [78]

One of the photoprotective processes in chlorosomes is the quenching of BChl triplets by carotenoids. No triplet states of BChl *c* in aggregates or BChl *a* in the baseplate were observed at room temperature measurements [87, 88], which points to the 100% efficiency of the quenching. [87] Consequently, the excitation energy must be transferred to some of the few BChls *c* with neighbouring carotenoids or to BChls *a*, which are all in close contact with at least one carotenoid. Oppositely, the triplet states of BChl *c* and BChl *a* were detected at low temperatures (1.8 K). [15] The observed triplet states of carotenoids seem to be generated mainly by the quenching of BChl *a*. BChl *a* in a baseplate is a bottleneck for excitation energy. Therefore, the triplet quenching of BChl *a* by carotenoids is essential for photoprotection. As well as the photoprotective mechanism based on the quenching of BChls by carotenoids, the aggregation-mediated protection mechanism should also be involved. [89] Another mechanism is based on a shortening of both singlet and triplet excited state lifetimes. [88] The singlet state lifetime decreases the triplet state population through ISC. Moreover, the shorter triplet state lifetime directly decreases the probability of the $^1O_2$ generation. Some early works by Krasnovsky et al. demonstrated the mechanism. [90]

2. Materials and methods

2.1 Samples

The acpPC complex from *Amphidinium carterae* was kindly provided by the group of Prof. Eckhard Hofmann (Department of Biology and Biotechnology, Ruhr-University Bochum, Germany). The acpPC complex was isolated as described in [58, 12] The samples were dissolved in a tricin-buffer (pH 7.5). The buffer for RT measurements consisted of 20 mM KCl (Sigma-Aldrich), 0.16 % n-decyl β-D-maltoside (DM, Glycon) and 20 mM tricin (Sigma-Aldrich). The samples for low-temperature experiments were diluted in a tricine-buffer/glycerol mixture (1:2, Sigma-Aldrich). However, the composition of the tricin-buffer was 80 mM KCl, 0.64 % DM and 80 mM tricin in the case of low-temperature measurements. The different composition of the buffer was necessary to prevent sample aggregation in the presence of glycerol (see figure 3.7).

LHC-II extracted from the pea was kindly provided by Dr. Heiko Lokstein. The LHC-II antennas were isolated as described previously in [55]. The buffer (pH 7.8) for RT samples was prepared from 20 mM tricin and 0.06 % n-Dodecyl β-D-maltoside (DDM, Glycon) in distilled water. The buffer for low-temperature samples was prepared from 20 mM tricin and 0.12 % DDM and mixed with glycerol in a ratio of 1:2.

An isolation of chlorosomes of green non-sulfur bacteria *Chloroflexus aurantiacus* is described in [91]. The sample was dissolved in a tris-HCl buffer (pH 8.0) mixed with glycerol in a ratio of 1:2. The tris-HCl buffer was prepared from tris base (Sigma-Aldrich) and adjusted with concentrated HCl.

The target absorbance of the sample was $\approx 0.4 - 0.6$ OD per 1 cm at Q_y band for all samples. All measurements were performed under aerobic conditions.

2.2 Transient spectroscopy setup

In chapter 3, photoprotective and spectral properties of LHCs are studied through measurements of transient absorption (TA) spectra. The TA spectra were further processed by global analysis, which extracts information about the energy transfer dynamics and pathways. The Optical Spectroscopy Group of the Department of Chemical Physics and Optics is equipped with the setup for TA spectra measurements with a nanosecond resolution. However, several improvements had to be made for experiments at low temperatures.

The scheme of the transient spectroscopy setup is shown in figure 2.1. The samples are excited by an optical parametric oscillator (OPO, PG122, EKSPLA) providing laser pulses of $3 - 3.5$ ns FWHM between 200 to 2000 nm. The excitation energy was set to $\approx 500\,\mu\mathrm{J} \cdot \mathrm{cm}^{-2}$ per pulse. OPO is pumped by the second and third harmonic frequency of a Q-switched solid-state Nd:YAG laser (NL303G/TH, EKSPLA) with a repetition rate of 5 or 10 Hz for TA and transient fluorescence measurements, respectively. A laser pulse passes through several neutral density filters (ND) and lenses to the optical cryostat (OptistatDN2, Oxford Instrument) for low-temperature measurements, or the sample holder for RT measurements

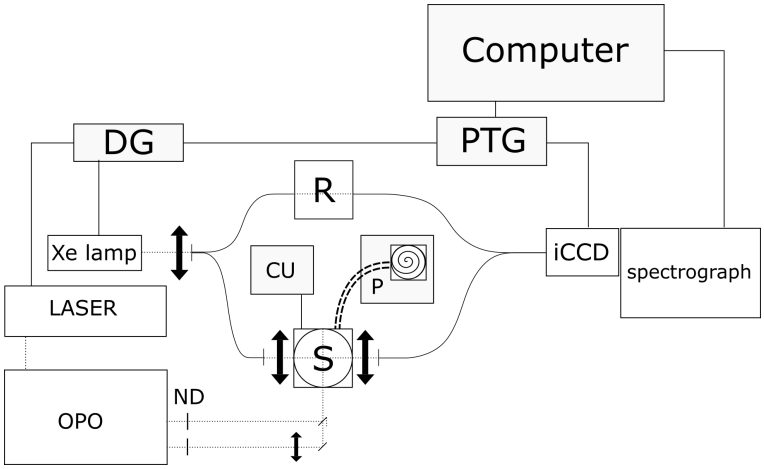

Figure 2.1: Scheme of the transient spectroscopy setup.

(not shown in the scheme). The sample (S) in a cuvette is excited at t_0 in a right-angled geometry. The sample is probed by radiation of Xenon flash lamp with a broad spectrum (LS-1130-1, FX-1161 flash tube, Perkin Elmer) at a certain time delay after the laser excitation. The Xenon flash lamp is also used for reference (R) signal. The probe pulse is delivered to and from the sample by optical fibres and collimated by two lenses into the cryostat. A precise x-y shift of collimators is used for maximizing the signal. The sample and reference signals are transmitted to the imaging spectrometer (iHR 320, Horiba Jobin Yvon) with a $100\,\mathrm{gr}\cdot\mathrm{mm}^{-1}$ grating blazed at 450 nm. The grating was usually centred at 550 nm for detection of a $375-750$ nm spectral region. The signal was detected by an intensified charge-coupled device camera (iCCD, PI-MAX 512RB, Roper Scientific). The amplifier of the iCCD camera is used for fast gating with a 2 ns gate-width. The synchronization of excitation pulses, probe pulses and iCCD camera gating is secured by a programmable delay generator (DG535, Stanford Research Systems) triggered by a timing generator (PTG) integrated in the controller of the iCCD camera. All the TA or fluorescence spectroscopy measurements are controlled by a program called WinSpec together with a measurement script written in Python. The TA spectra are averaged of 500 (500x2 flash pulses) or 750 cycles.

A liquid nitrogen optical cryostat is used for measurements in temperatures from 77 to RT. The sample temperature is controlled by the control unit (CU, MercuryiTC, Oxford Instruments). The cryostat vacuum chamber is pumped out by a turbomolecular pump (P, T-Station 85, Edwards) to at least $< 10^{-5}$ mbar. The heat is exchanged between the liquid nitrogen and the sample by helium gas fed into the sample chamber through a valve vent with attached bladder. A new path was built for visible and near-infrared excitation in the cryostat. The sample can be measured in UV plastic cuvette (Kartell) with 1 cm optical path inserted into the sample holder, or it can be brought to the low-temperature quartz cuvette with $0.1-0.5$ mm optical path in a teflon home-made sample holder. All measurements described in this thesis were performed in plastic cuvettes. The instruction list for measurements with the cryostat is attached to the thesis; see attachment 1.

2.2.1 Measurement of transient absorption spectra

TA spectra measurements belong to "pump-probe" methods. In these methods, pump pulse disrupts an equilibrated sample by the supply of energy, and probe monitors the relaxation and ET processes.

During the TA measurement a short and spectrally narrow laser pulse excites the sample at t_0. At the certain delay τ after the laser pulse, the sample is probed by a polychromatic Xenon lamp pulse. The TA spectra measurement process is shown in figure 2.2. The signal detected on the iCCD camera is compared with the reference signal and subtracted from the sample absorption in equilibrium. The expression for TA absorbance can be derived from the Lambert-Beer law [29]

$$\begin{aligned} \Delta A_{\mathrm{TAS}}(\tau,\lambda) = A_{pump}(\tau,\lambda) - A_{eq}(\lambda) = \\ = -\log\left(\frac{I_{pump}(\tau,\lambda)}{I_{pump(ref)}(\tau,\lambda)}\right) + \log\left(\frac{I_{eq}(\lambda)}{I_{eq(ref)}(\lambda)}\right) = \\ = -\log\left(\frac{I_{pump}(\tau,\lambda)}{I_{eq}(\lambda)}\right) + \log\left(\frac{I_{pump(ref)}(\tau,\lambda)}{I_{eq(ref)}(\lambda)}\right) = \\ = -\log\left(\frac{I_{pump}(\tau,\lambda)}{I_{eq}(\lambda)}\right) + \text{background}, \end{aligned} \tag{2.1}$$

where the meaning of I_x is explained in figure 2.2. In the ideal case, the background defined in equation 2.1 should be the same for each cycle. However, it is measured separately for every excitation because of the instability of the xenon lamp ($\pm 5\%$ difference in pulse intensity) and the photodegradation of the measured sample.

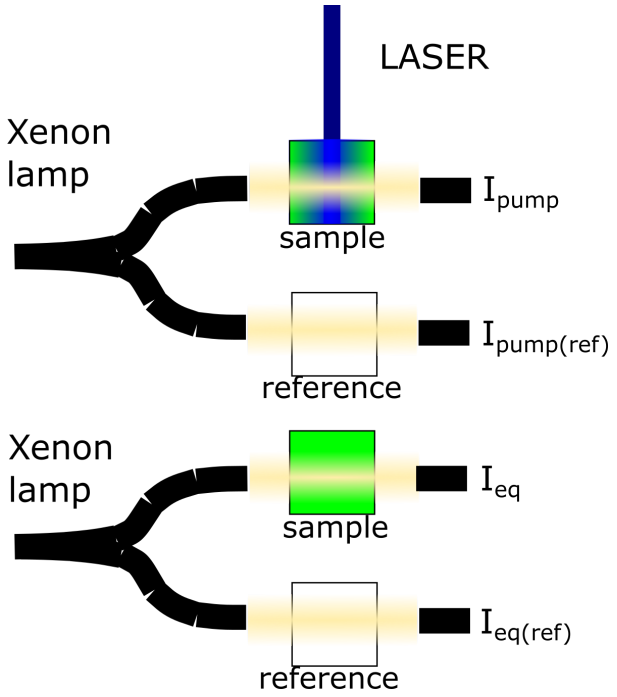

Figure 2.2: Scheme of measurement of transient absorption spectra.

In the steady-state absorption spectra, each band refers to the transition from the ground state to the excited states. TA spectra provide information about the

evolution of excited states and the return of the sample to its equilibrium. Let us describe the difference between the steady-state absorption spectrum and the TA spectrum in a model situation illustrated in figures 2.3 and 2.4. In figure 2.3 (A), a blue and a green absorption bands are assigned to the transitions of molecules X and Y to an excited state, respectively. The sum of both bands forms a steady-state absorption spectrum (dotted line). If the sample is excited at the wavelength of the blue band, then there will be fewer X molecules in the ground state. The excited molecules may absorb at different wavelengths (orange colour in figure 2.3 (B)). The resulting TA spectrum in figure 2.3 (C) is the difference between the steady state absorption spectrum and the excited state absorption spectrum (dashed line) in (B).

In the TA spectra of the model shown in figure 2.3 (C) three bands are visible, which are caused by different processes. The blue negative band is a result of the lower absorption from the ground state of X molecules after being excited. This phenomenon is called ground state bleaching (GSB). Excited state absorption (ESA, orange) is the process behind the positive band occurring in the higher wavelengths. The most red-shifted band in the TA spectrum in figure 2.3 (C) arises due to the luminescence of X molecules. The emitted photons amplify the signal and result in a negative band of the TA spectrum. The luminescence signal is usually much stronger than GSB and, therefore, it overlays GSB of the smallest absorption band. Of course, the TA spectra would exhibit a decrease of all three bands in time.

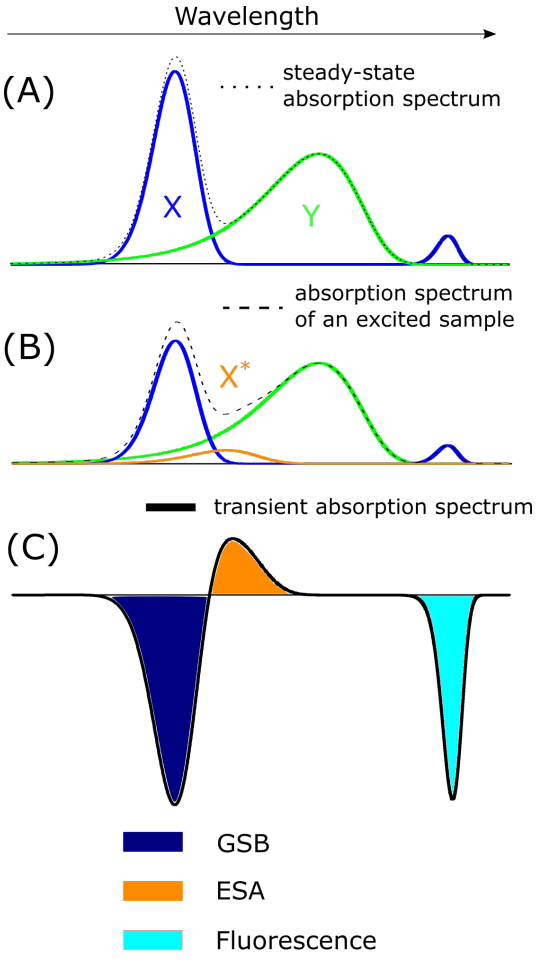

Figure 2.3: Example of formation of transient absorption spectrum at exact delay after laser pulse and its derivation from the steady-state absorption spectrum.

As almost none of the Y molecules were excited, they do not contribute to the TA spectrum. The situation is different in the presence of ET from X molecules to Y molecules. In that case, the TA spectra would reflect the rise of GSB and ESA assigned to the Y molecule. Simultaneously, the TA spectrum would exhibit a decay of all the bands assigned to the X molecule. Therefore, the TA spectra contain information about the system evolution and ET.

All the TA spectra presented in chapter 3 are processed by global analysis, which can extract information about dynamic paths of excited energy.

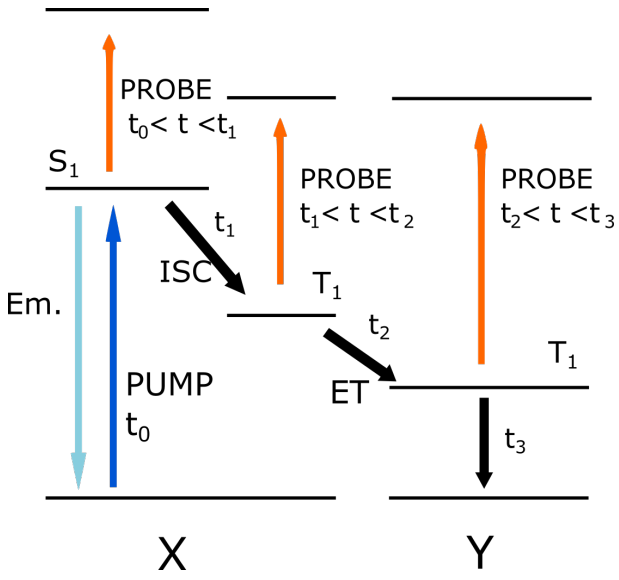

Figure 2.4: Example of a pump-probe measurement for two interacting molecules. The X molecule is excited at t_0. The excitation is transferred to other states at t_1, t_2 and t_3. For instance, if we probe the sample at $t_0 < t < t_1$, then the exact molecule can be excited to a higher excited state.

2.2.2 Global analysis

Global analysis will be discussed on the model situation described by the black arrows in figure 2.4. Dynamics paths of molecules X and Y are described through equations:

$$\frac{\mathrm{d}[\mathrm{X}(\mathrm{S}_1)]}{\mathrm{d}t} = -k_{ISC}[\mathrm{X}(\mathrm{S}_1)] - k_{Em.}[\mathrm{X}(\mathrm{S}_1)], \tag{2.2}$$

$$\frac{\mathrm{d}[\mathrm{X}(\mathrm{T}_1)]}{\mathrm{d}t} = -k_{ET}[\mathrm{X}(\mathrm{T}_1)] + k_{ISC}[\mathrm{X}(\mathrm{S}_1)], \tag{2.3}$$

$$\frac{\mathrm{d}[\mathrm{Y}(\mathrm{T}_1)]}{\mathrm{d}t} = -k_{deact.}[\mathrm{Y}(\mathrm{T}_1)] + k_{ET}[\mathrm{X}(\mathrm{T}_1)], \tag{2.4}$$

where [M(S)] is concentration of a molecule M in the S state and $k_{process}$ is a rate constant for a process shown in figure 2.4. We assume that the $k_{Em.} >> k_{ISC}$. The differential equations 2.2-2.4 solution is:

$$[\mathrm{X}(\mathrm{S}_1)](t) = [\mathrm{X}(\mathrm{S}_1)](0)\exp\left(-k_{Em.}t\right), \tag{2.5}$$

$$\begin{aligned}[\mathrm{X}(\mathrm{T}_1)](t) = [\mathrm{X}(\mathrm{S}_1)](0)\frac{-k_{ISC}}{k_{Em.}-k_{ET}}\exp\left(-k_{Em.}t\right) \\ + \left([\mathrm{X}(\mathrm{T}_1)](0) + [\mathrm{X}(\mathrm{S}_1)](0)\frac{k_{ISC}}{k_{Em.}-k_{ET}}\right)\exp(-k_{ET}t),\end{aligned} \tag{2.6}$$

and if we denote $[\mathrm{X(S_1)}](0)\frac{k_{ISC}}{k_{Em.}-k_{ET}}$ as C then the solution of the last differential equation is

$$[\mathrm{Y(T_1)}](t) = k_{ET}\left[\frac{\mathrm{C}}{k_{Em.}-k_{deact.}}\exp\left(-k_{Em.}t\right) - \left(\frac{[\mathrm{X(T_1)}](0)+\mathrm{C}}{k_{ET}-k_{deact.}}\right)\exp\left(-k_{ET}t\right)\right] + \left[[\mathrm{Y(T_1)}](0) - \frac{k_{ET}\mathrm{C}}{k_{Em.}-k_{deact.}} + k_{ET}\left(\frac{[\mathrm{X(T_1)}](0)+\mathrm{C}}{k_{ET}-k_{deact.}}\right)\right]\exp\left(-k_{deact.}t\right). \tag{2.7}$$

The solution can be simplified with the assumption that $[\mathrm{A(S_1)}](t_0) = 0$ and $[\mathrm{B(T_1)}](t_0) = 0,\ t_0 = 0$. As shown in the case of the model from figure 2.4, evolution of concentration for each excited state is described by a sum of exponentials. In general, if it is assumed that population and depopulation of an excited state can be described by linear kinetics equation, then its decay is governed by equation [92]

$$[\mathrm{M_i}](t) = \sum_m \left(\sum_n [M_n](0)K_i^{mn}\right)\exp\left(-k_m t\right), t \geq 0. \tag{2.8}$$

Each excited state contributes to overall transient absorption signal at given delay after laser pulse by

$$\Delta A_{TAS}(t,\lambda) = \sum_i [M_i](t)\Delta A_i(\lambda), \tag{2.9}$$

where $\Delta A_i(\lambda)$ is TA spectrum of state i.

The data in chapter 3 are processed by a global analysis program kindly provided by Dr. Jan Alster. In the program, the TA experimental data (ΔA_{TAS}) are automatically processed to the matrix with rows according to delay (t_ϱ) after pump pulse and columns according to the wavelength (λ_σ). The experimental data are fitted by a linear combination of exponentials, which are convoluted with an instrument response function (IRF). The convolution with IRF is necessary to obtain a good agreement of a fit with experimental data on the nanosecond time scale. TA spectra from equation 2.9 can be rewritten assuming convolution with IRF and equation 2.8 as

$$\begin{aligned}\Delta A_{TAS}(t,\lambda) &= \sum_i\sum_m \left(\sum_n [M_n](0)K_i^{mn}\right)\exp\left(-k_m t\right)\Delta A_i(\lambda) * \mathrm{IRF}, \\ &= \sum_i\sum_m \left(\sum_n [M_n](0)K_i^{mn}\right)\exp_{IRF}\left(-k_m t\right)\Delta A_i(\lambda).\end{aligned} \tag{2.10}$$

The IRF was written as a subscript for convoluted monoexponential function. The fitting model can be extended by adding a "zero lifetime component" with Gaussian function shape, which is approximately equal to the shape of the scattered laser pulse signal. Such an approximation is in good agreement with the real profile of laser pulse due to the signal noise. Through modification and mixing of components in equation 2.10, we can split the model expression into three independent matrices

$$\Delta A_{TAS}(t_\varrho, \lambda_\sigma) =$$
$$= \sum_i \sum_m \left[\exp_{IRF}(-k_m t)\right]_{\sigma m} \left[\left(\sum_n [M_n](0) K_i^{mn}\right)\right]_{mi} [\Delta A_i(\lambda)]_{i\varrho} = \tag{2.11}$$
$$= C_{\sigma m} D_{mi} E_{i\varrho},$$

where columns of matrix C describe convoluted monoexponential decays of all individual excited states, rows of matrix E belong to individual excited state transient spectra and square matrix D mix transient spectra of the various excited states with decays in columns of matrix C. For more details see [92].

The data separation in equation 2.11 is further used for data analysis through decay associated spectra (DAS, or in singular form "DA spectrum"). The product of matrices D and E has rows composed of a mixture of TA spectra belonging to the excited states, which decay with the same rate. The previous sentence shows that each DA spectrum is connected to a lifetime of one excited state and consists of the TA spectra of this excited state and other excited states interacting with this excited state. These interactions include ET, ISC, etc.

For example, DAS can be extracted from a solution of differential equations 2.5-2.7. Considering the above mentioned DA spectrum specification and established notation, we get DA spectrum for the state with the rate constant $k_{Em.}$

$$\mathrm{DAS(k_{Em.})} = [\mathrm{X(S_1)}](0)\Delta A_{[\mathrm{X(S_1)}]}$$
$$+[\mathrm{X(S_1)}](0)\frac{-k_{ISC}}{k_{Em.} - k_{ET}}\Delta A_{[\mathrm{X(T_1)}]} + \frac{k_{ET}\mathrm{S_1}}{k_{Em.} - k_{deact.}}\Delta A_{[\mathrm{Y(T_1)}]}. \tag{2.12}$$

However, two fundamental limitations should be kept in mind. First, the signal in the DA spectrum is detected only if accumulation of the excited state level is high enough to yield a signal higher than noise. For example, $[\mathrm{A(T_1)}]$ would not be detected if the rate of k_{ET} quickly depopulated the level and thus prevented its accumulation. The second limitation is in time resolution.

The lifetimes in the next chapter are reported with standard errors, which were always calculated from at least four measurements. The errors in the charts with temperature dependence (figures 3.16, 3.23, 3.6) are estimation ($5-10\,\%$).

2.3 Absorption spectroscopy at 77 K and room temperature

The steady-state absorption spectra were measured in a spectrometer (Specord 250, Analytik Jena) for characterization of samples. The RT steady-state absorption spectra were used for monitoring of the sample photodegradation. Apart from the measurements at RT, we modified the spectrometer for measurements with the cryostat. Now we can measure the absorption spectra from 77 K to RT. The reference for low-temperature absorption spectrum was always measured separately, before each measurement. The advantage of low-temperature absorption spectra is in a better vibronic resolution. Also, the low-temperature absorption spectra are used in comparison with the TA spectra.

3. Results and discussion

3.1 Light-harvesting complex II of higher plants

3.1.1 Steady-state absorption spectra

Figure 3.1 shows the absorption spectra of LHC-II at RT and 77 K. The RT spectrum is formed mainly by the Soret bands of Chl *a* (≈436 nm) and Chl *b* (≈471 nm) overlapped with an absorption of carotenoids. The Q_y bands with maxima at 653 and 672 nm are ascribed to Chl *b* and Chl *a*, respectively. The sidebands in the spectral region between 630 −650 nm are ascribed to the vibronic structure of the Q-bands. [93, 8] The vibronic resolution is significantly improved in the low-temperature spectrum. The spectrum at 77 K shows several new peaks centred at 676 nm, 672 nm, 662 nm, which agree with spectrally shifted subpopulations of Chl *a* reported in [93]. Also, the Q_y band of Chl *b* is magnified. In the region of the Soret band, several sidebands at ≈461 nm, ≈486 nm and ≈494 nm can be observed.

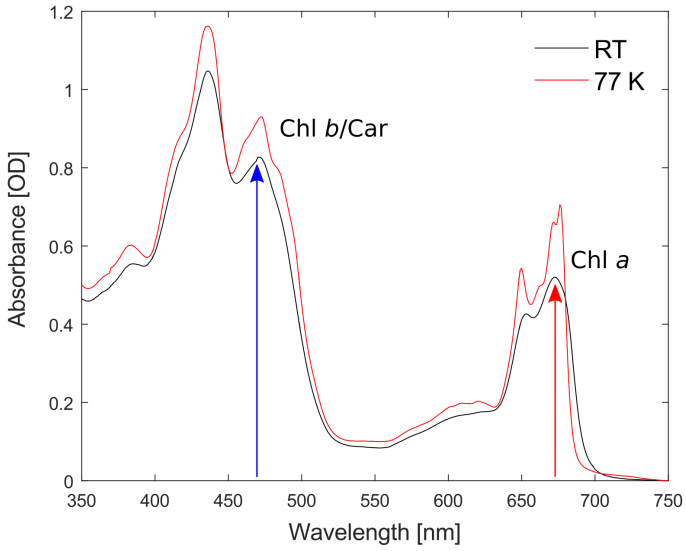

Figure 3.1: Steady-state absorption spectra of LHC-II from pea at room temperature (RT, black line) and 77 K (red line).

3.1.2 Transient absorption spectra between 77 K and room temperature

Transient absorption spectra at room temperature

The measurements of TA spectra at RT were performed on the samples of LHC-II dissolved in a buffer and a buffer/glycerol (1:2). The results in the buffer solution can be compared to the results reported in microsecond time scale by Mozzo et al. and Peterman et al. [8, 14]

Figure 3.2 (Left) shows selected TA spectra of LHC-II excited at 675 nm (the Q_y band of Chl *a*) in the buffer, which were measured in a room-temperature

sample holder (RTSH). Although the spectra were recorded up to 740 nm, they are cut off at 630 nm due to the strong fluorescence signal at longer wavelengths. The spectrum at 1 ns shows a significant Soret band bleaching of Chl *a*. No Soret band bleaching of Chl *b* was observed, even in the case of excitation at 470 nm (data not shown, the Soret band of Chl *b*), proving that the singlet-singlet ET between Chls *b* and Chls *a* occurs in a picosecond time scale. [94] GSB of Chl *a* quickly decays in few nanoseconds and it is exchanged for GSB of carotenoids, which is connected with the shift of the band minimum to ≈425 nm. [8] The positive bands in the spectral region between 460 −570 nm are assigned to triplet ESA of carotenoids. [8, 14] The decay of the singlet state of Chl *a* is followed by a rise of the triplet ESA band of carotenoids centred at 510 nm. The TA spectra at later times (>200 ns) exhibit structures of carotenoid triplets and decay within 10 μs. The maximum of the major ESA band is slightly shifted during the decay from 510 nm to 515 nm. On the contrary, the ESA band with the maximum at 475 nm remains at its position.

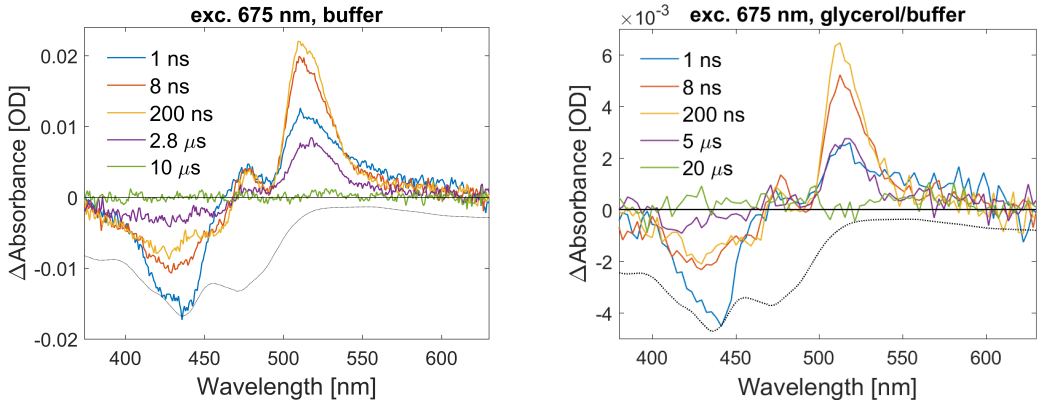

Figure 3.2: Transient absorption spectra of LHC-II at room temperature (RT) with excitation at 675 nm. (Left) The sample dissolved only in a pure buffer. (Right) The sample dissolved in a buffer/glycerol (1:2). Software data binning is used. The inverted steady-state absorption spectra at RT (black dotted line) are shown for comparison.

Figure 3.2 (Right) shows selected RT TA spectra of LHC-II dissolved in a buffer/glycerol (1:2) taken in the cryostat. The experiment was performed to observe how much the results are affected by change of the solvent from buffer to a mixture of buffer with glycerol. The data illustrate the same spectral evolution of the spectra as in the case of buffer solution. However, the lifetime of excited states of carotenoids is significantly prolonged, which is related to different accessibility of oxygen, or different solvent viscosity. [14]

Decay associated spectra at room temperature

The TA spectra were processed by global analysis. Three components were used for fitting in the case of the pure buffer solution, see figure 3.3 (Left). The TA spectra decomposition into three components is in agreement with reported results at RT under aerobic conditions. [8, 14] Other groups resolved only one component with a microsecond lifetime. [95, 96] The satisfactory residua can be obtain in both cases.

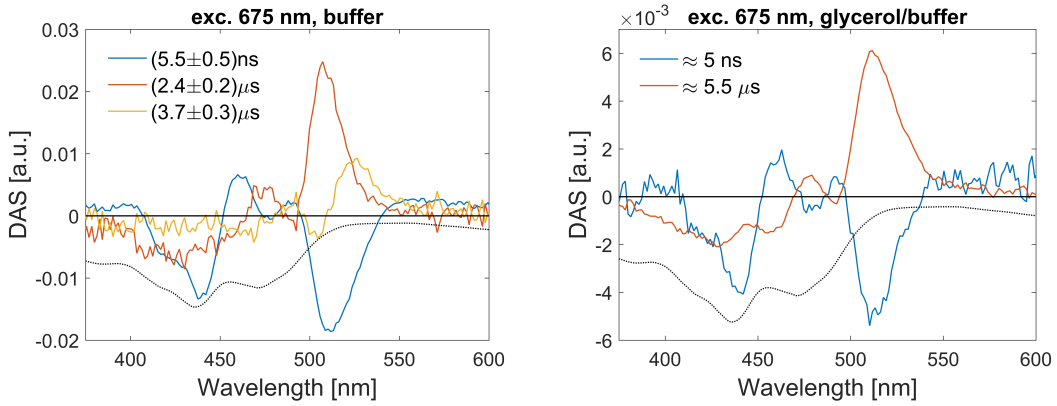

Figure 3.3: Decay associated spectra (DAS) of LHC-II excited at 675 nm at room temperature (RT). (Left) The sample dissolved only in a buffer. (Right) The sample dissolved in a buffer/glycerol (1:2). The inverted steady-state absorption spectra at RT (black dotted line) are shown for comparison.

The ns component (blue line) of decay associated spectra (DAS) consists of several regions. The negative band with the minimum at 440 nm is assigned to the Soret band bleaching of Chl *a* and the sideband peaking at 420 nm is ascribed to the vibronic structure of the Soret band. The singlet ESA of Chl *a* at 450 −500 nm is overlapped with the negative band of carotenoid triplet ESA with the minimum at 479 nm, which is neighbouring with the major negative triplet ESA band with the minimum at 510 nm. The triplet ESA bands of carotenoids are negative due to their rising signal during the decay of excited states of Chl *a*. The Soret band of Chl *a* is most likely diminished by the rising GSB (positive band) of carotenoids. Also, carotenoids usually have higher extinction coefficient compared to chlorophylls. [34, 39] Therefore, it is lower than the major triplet ESA band centred at 510 nm. The first component of DAS definitely corresponds to the ET from Chls to carotenoids. However, the spectral features of Chl *a* S_1 state and lifetime 5.5(5) ns, which is close to the fluorescence lifetime of Chl *a* at RT [34, 9], show that the Chl *a* triplets are quenched by carotenoids with the transfer time of DET under our resolution. Therefore, the component does not exhibit Chl *a* triplet features. The similar behaviour was observed in acpPC. [12]

The 2.4(2) μs and 3.7(3) μs components of DAS are ascribed to the decay of generated triplets of carotenoids. The lifetimes are similar to the previously published results. [14, 8] Each component belongs to a different subpopulation of carotenoids. Both DAS show GSB bands with minima at ≈430 and ≈470 nm. [14] The spectral shift is also well illustrated by the ESA bands. The faster component exhibits the ESA band centred at 475 nm and the major ESA band with the maximum at 507 nm. The maxima of the ESA bands of the slower component are shifted to 492 and 525 nm.

Mozzo et al. [14] suggest that the two microsecond components have an origin in two central luteins with a different oxygen accessibility. The outcome is in agreement with our results.

The DAS of LHC-II in a more viscous glycerol/buffer solution are presented in figure 3.3 (right). Only two components were resolved. The spectral shape of the fast DA spectrum is identical to the previous sample. Also, its lifetime is conserved, which illustrates that chlorophylls inside the antenna complex are

shielded from interaction with solvent. The lifetime of the decay of carotenoid triplets is prolonged to ≈5.5 μs. The prolongation of the lifetime of carotenoid triplets was observed before, and it is due to a different oxygen concentration which enhances the ISC, and different viscosity of the solvent. [8, 14] The maxima of triplet ESA bands of carotenoids are at 478 and 511 nm. The spectral shape of the slower component corresponds to the sum of ≈2.4 μs and ≈3.7 μs DAS in the case of a buffer solvent. The result is similar to LHC-II under anaerobic conditions. However, we do not observe long-lived triplets of Chl, which were reported in [14].

No triplets of Chl were observed at RT, as in the case of Peterman et al. [8] We cannot confirm the previous reports of low concentration of long-lived Chl triplets (≈ 5%) under anaerobic conditions. [14] We suggest that the Chl triplets can be presented at RT in the case of LHC disintegration. Our results show 100 % efficiency of photoprotection in LHC-II at RT.

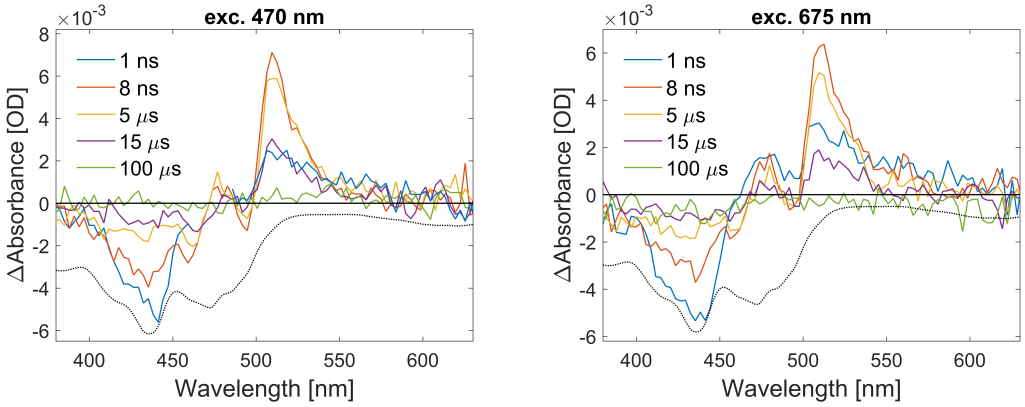

Figure 3.4: Transient absorption spectra of LHC-II at 77 K with excitation at 470 nm (Left) and 675 nm (Right). Software data binning is used. The inverted steady-state absorption spectra at 77 K (black dotted line) are shown for comparison.

Transient absorption spectra at 77 K

The TA spectra of LHC-II at different temperatures were measured with excitation at 470 and 675 nm. The spectra at 77 K are shown in figure 3.4. In both cases, the spectra show better vibronic resolution as it is typical for low-temperature measurements. The evolution of the system is much slower compared to RT at the late times. However, the signal from Chls *a* also vanishes in several nanoseconds. The negative band at 460 nm is more pronounced and triplet ESA band of carotenoids at 510 nm is narrower than at RT.

There are no significant differences between the excitation at 470 nm and 675 nm. The TA spectra of LHC-II at 77 K also describe the fast quenching of Chls *a* and relaxation of carotenoids in a time scale of microseconds same as the RT spectra.

Decay associated spectra at 77 K

In the same way as the TA spectra, the ns and μs components of DAS at 77 K show only minor spectral changes compared to RT DAS in a buffer/glycerol solution.

The samples excited at 470 and 675 nm exhibit prolonged lifetime of the fast component to ≈6.8 ns and 6.5(7) ns, respectively. The lifetime of the S_1 state of Chl *a* is independent of the efficiency of quenching of Chl triplets. Therefore, the prolongation is most likely due to an intrinsic dependence of $S_1 \rightarrow S_0$ transition on temperature, which was observed before. [97] No Chl triplet features are observed in the faster component, which means that the transfer time of DET between Chl triplets and central carotenoids (most likely luteins) is still fast enough to prevent accumulation of Chl triplets.

The carotenoid triplets decay with a lifetime of ≈11.8 μs (excitation at 470 nm) and 12.3(6) μs (excitation at 675 nm) in line with previously reported results. [8] Previously reported decay of carotenoids in LHC-II at low temperature was also fitted by one component contrary to a pure buffer solution at RT, which is presumably due to lower oxygen diffusion in a frozen sample.

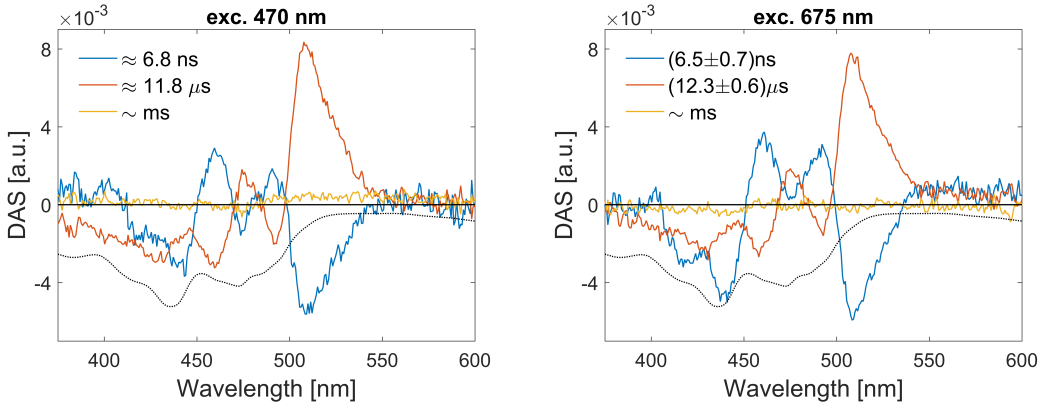

Figure 3.5: Decay associated spectra (DAS) of LHC-II at 77 K with excitation at 470 nm (Left) and 675 nm (Right). The inverted steady-state absorption spectra at 77 K (black dotted line) are shown for comparison.

A weak signal is resolved, which decays with a millisecond lifetime. The signal was too low to be observed in TA spectra. The signal is assigned to triplets of Chl *a* in the case of excitation at 675 nm and triplets of Chl *a* and *b* in the case of excitation at 470 nm. The population of Chl triplets is around <5 %. A similar signal was reported in [8]. The Chl triplets belong to a subpopulation not presented in the fast component. Therefore, we suggest that the long-lived Chl triplets are generated from Chls, which cannot transfer their energy to the red Chls protected by luteins. LHC-II should be intact in view of no observation of Chl triplets at RT.

Temperature dependence

Figure 3.6 shows a temperature dependence of the lifetimes of the ns and μs components of DAS (buffer/glycerol solvent). The lifetimes ascribed to the long-lived Chl triplets are not shown due to the weak signal resulting in large error of the estimated values. The results for excitation at 675 and 470 nm are analysed together as the differences between the lifetimes are under an experimental error and no significant differences are observed at the DA and TA spectra. The temperature dependence of the lifetimes is fitted by the Arrhenius equation

$k_{decay} \approx A \exp\left(-\frac{E_a}{RT}\right)$. [98] Lifetimes were determined with an error more than 8 %.

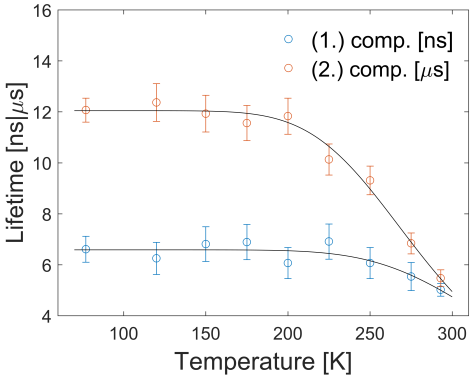

Figure 3.6: Temperature dependence of the lifetimes of the DAS components (excitation at 675 and 470 nm).

The fast component (blue line, lifetime scale is in ns) is slightly prolonged from ≈5.5 ns at RT to ≈6.5 ns at 225 K. The lifetime does not changed below 225 K. Obviously the ns lifetimes illustrate the dependence of the S_1 state of Chl *a* on temperature. Direct observation of the Dexter energy transfer (DET) from Chl triplets to carotenoids is not possible due to a transfer time under our resolution, which precludes the generation of an observable population of Chl triplets. The quenching by carotenoids works efficiently at low temperature. We suggest that the transfer time of DET from triplets of Chls to carotenoids must be at least under 0.1 ns. [12]

The lifetime of the slower component (red line, lifetime scale is in μs) rises from ≈5.5 μs at RT to ≈12.0 μs at 200 K and is not changed by further cooling. The same (in)dependency of carotenoids lifetime on the temperature below 150 K was previously reported in [99].

3.2 The acpPC complex of *A. carterae*

3.2.1 Steady-state absorption spectra

The steady-state absorption spectra of acpPC from *Amphidinium carterae* are shown in figure 3.7. The spectra were measured from 350 to 750 nm at RT and 77 K. Both spectra were taken on the same sample in the cryostat.

The RT sample has a dominant absorption between 350 −570 nm, which is formed mainly by an absorption of Chls and the contributions of peridinin and diadinoxanthin. Two maxima at 441 nm and 461 nm are assigned to the Soret bands of Chl *a* and Chl c_2, respectively. The blue-shifted sidebands of the major band are most likely vibronic bands of Chl *a* and Chl c_2. Both carotenoids are responsible for the red-shifted absorption. The main transition $S_0 \longrightarrow S_2$ of peridinin is at 485 nm in a non-polar n-Hexane solvent. Nevertheless, a polar environment and an interaction with surrounding proteins can blur its spectra and shift it to longer wavelengths. Therefore, the sidebands at ≈500 and ≈540 nm are assigned to peridinin. Diadinoxanthin is also involved in the formation of a shoulder at ≈500 nm. [9] However, its low stoichiometry in acpPC prevents any significant contribution. A sharp peak with a maximum at 672 nm is due to the Q_y transition of Chl *a*. Its blue-shifted sidebands at ≈636 and ≈650 nm are due to its vibrational structure, and the Q_x band overlapped with the Q-bands of Chl c_2 at ≈632 nm and ≈649 nm, which were identified by circular dichroism and low-temperature absorption. [11, 74]

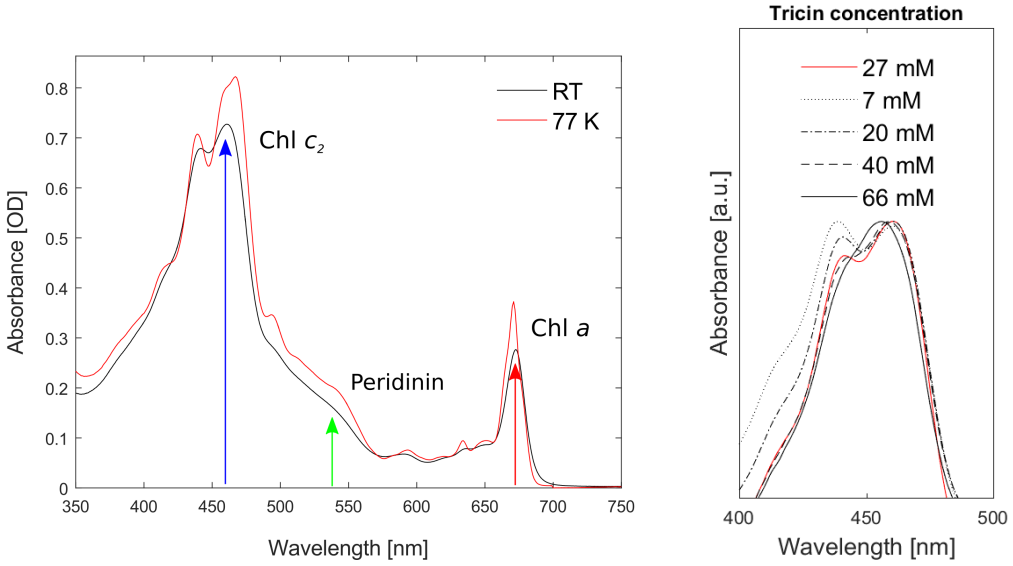

Figure 3.7: (Left) Steady-state absorption spectra of acpPC from *Amphidinium carterae* at room temperature (RT, black line) and 77 K (red line). (Right) The dependence of the shape of the major band on concentration of detergent.

The frozen sample at 77 K shows an enhanced vibronic structure of the absorption spectrum in all bands. Also, a slightly higher absorbance across almost the whole spectrum is observed, which is most likely due to an increased scattering on ice. The major band is split into three maxima at 439 nm, 460 nm and 468 nm. The peak at 439 nm is obviously connected to Chl *a*, and the other two

are from the absorption of Chl c_2. The positions of the peaks are in good agreement with the deconvolution of absorption spectra of acpPC from *Symbiodinium* made by Niedzwiedzki et al. [9] The significantly-enhanced peak at 494 nm is most likely connected to the diadinoxanthin, which exhibits a significant increase of vibronic peaks of the $S_0 \rightarrow S_2$ transition at a low temperature. [9] The rest of the sideband shows at least two other bands peaking at ≈510 nm and ≈545 nm, which correspond to two spectrally-shifted peridinins. Another band centred at 594 nm is red-shifted compared to the RT spectrum and is most likely connected to the Q_x band of Chl c_2. [34] The Q_y band of Chl a is blue-shifted to 671 nm with two shoulders, which suggest that at least two spectrally-different subpopulations of Chl a are presented. Several bands arise in the area of Chl c_2 and Chl a Q-bands, with maxima at 650 nm, 634 nm and 618 nm.

Figure 3.7 (Right) shows the dependence of the shape of the major band on the concentration of the detergent (27 mM of tricin ⇒ 0.21 % of DM). The low concentration of detergent leads to an aggregation of the acpPC complexes. The high concentration shows the disintegration of acpPC and a blurring of the major band. The sensitivity of acpPC to the detergent concentration is high. The better resolution of our spectrum at 77 K compared to [9, 69] is most probably due to a good ratio of detergent in the sample.

3.2.2 Transient absorption spectra between 77 K and room temperature

Transient absorption spectra at room temperature

Figure 3.8 (Left) presents selected transient absorption spectra of acpPC dissolved in a buffer and measured in RTSH. The sample was excited at 670 nm (the Q_y band of Chl a). The experiment in RTSH was performed to demonstrate the same results for a new batch of the acpPC sample compared to the previously-reported ones. [12] Also, the spectra exhibit a better resolution due to changes in iCCD camera binning. The spectra will serve as a control for the low temperature measurements due to their higher S/N ratio. As usual, the spectra were recorder from 370 to 740 nm.

The spectrum at 1 ns delay (blue line) exhibits a strong bleaching band around ≈438 nm with a vibrational structure and a broad ESA band in the spectral region between 470 −620 nm with three maxima at 490 nm, 510 nm and 555 nm. The spectrum above 630 nm (not shown) shows a strong signal from fluorescence, which overlays a bleaching of the Q_y band of Chl a. Fluorescence quickly vanishes with no signal after 50 ns. The comparison of the TA spectra with the steady-state spectrum illustrates that the bleaching at ≈438 nm is due to the Soret band of Chl a. The same situation is observed in the case of excitation at 540 nm or 460 nm (spectra not shown), which is in accordance with the previously reported fast ET (fs − ps) from all pigments to Chl a. [9, 58] The broad positive band (470 −620 nm) has its origin in the singlet ESA of Chl a at 470 −530 nm, the triplet ESA of carotenoids with a maximum at 510 nm, and a broad band at 530 −620 nm assigned to the triplet ESA of peridinin in a polar environment. [12] The maximum of the latter positive band is at 560 nm. The signal from Chl a bleaching quickly decays, and it is replaced by a shallow negative band corresponding to the GSB of carotenoids. Similarly, a positive signal at 510 nm

is replaced by a new band at ≈470 nm. The same sharp bands assigned to the triplet ESA of carotenoids are shown in the TA spectra of LHC-II, e.g. figure 3.2. The bands assigned to carotenoid ESA decay during several microseconds.

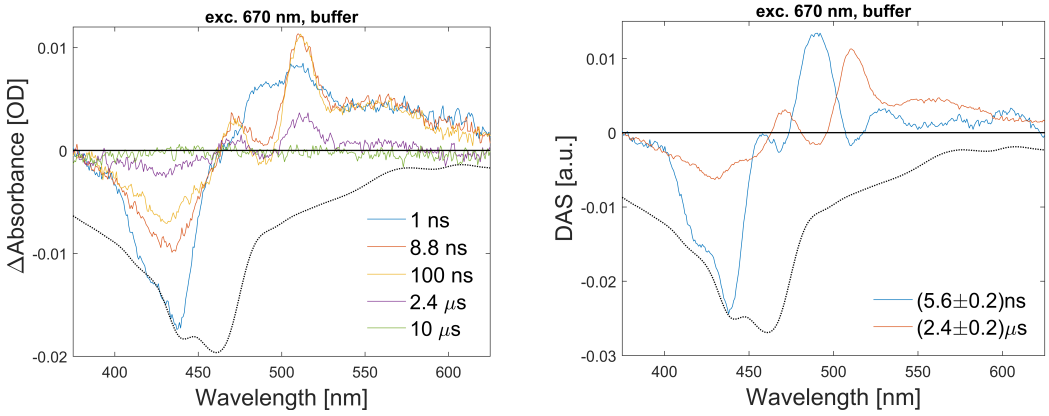

Figure 3.8: Transient absorption spectra (Left) of acpPC in a pure buffer at RT with excitation at 670 nm and their decay associated spectra (DAS, Right). The inverted steady-state absorption spectra (black dotted line) are shown for comparison.

Decay associated spectra at room temperature

The TA spectra in the spectral region between 370 −630 nm were processed by a global analysis. The region above 630 nm cannot be fitted simultaneously with the rest of the spectra due to the signal from fluorescence above 630 nm. The spectra are fitted by two components. Their lifetimes are determined to be 5.6(2) ns and 2.4(2) μs. The values are in good agreement with the lifetimes reported in [12]. The DAS are presented in figure 3.8 (Right).

The faster component of the DAS (blue line) consists of three spectral regions. The region between 400 −455 nm shows a negative band assigned to the decay of the Chl *a* Soret band bleaching. The region between 455 −530 nm reveals a decrease of a singlet ESA band of Chl *a* with a maximum at 490 nm and two bands with minima at 470 nm and 510 nm, which are caused by the rising signal of the triplet ESA of carotenoids. The third region between 530 −600 nm is related to the rise of the peridinin triplet ESA and a decrease of the singlet ESA of Chl *a*. The positive peaks at 575 and 605 nm are due to the singlet ESA of Chl *a*. The faster component shows that the lifetime of excited Chl *a* is identical to the lifetime of the generation of the triplet states of carotenoids. The observation demonstrates that the triplet states of carotenoids are populated by the quenching of Chl *a*.

The slower component is connected to the decay of carotenoids. The region above 470 nm seems to be a mirror image of the faster component except for missing notches at ≈575 and ≈605 nm, which proves that the bands are from the singlet ESA of Chl *a*. The region between 375 −500 nm is formed by the GSB of carotenoids, which is overlapped with positive triplet ESA bands of the peridinin in a non-polar environment, or diadinoxanthin, with maxima at 470 nm and 510 nm. Also, the other positive band with maximum at ≈560 nm is ascribed to the decay of peridinin triplet ESA, however, this time the peridinin must be located in a polar environment.

In summary, the spectra show only minor differences from the previously published data. [12] The red shift (≈5 nm) of all bands compared to [12] is probably due to a new calibration. The better resolution allows us to see a decay of the singlet ESA of Chl *a* at ≈575 and ≈605 nm. The TA and DA spectra are quite similar to LHC-II (glycerol/buffer), where we detected also two components with the same meaning: (1.) the quenching of Chls *a* by carotenoids and (2.) the relaxation of the populated triplets of carotenoids. No features of Chl *a* triplets are observed in the fast component, similarly as in the case of LHC-II due to the high rate of their quenching, which keeps their concentration at "zero" and so prevents the generation of harmful $^1O_2$.

Transient absorption spectra at 77 K

The acpPC complexes were dissolved in a glycerol/buffer (2:1) solvent for low-temperature measurements. The wavelengths for excitation were selected at 670 nm, 540 nm and 460 nm. The data from the sample excited at 460 nm are discussed separately in the last subsection.

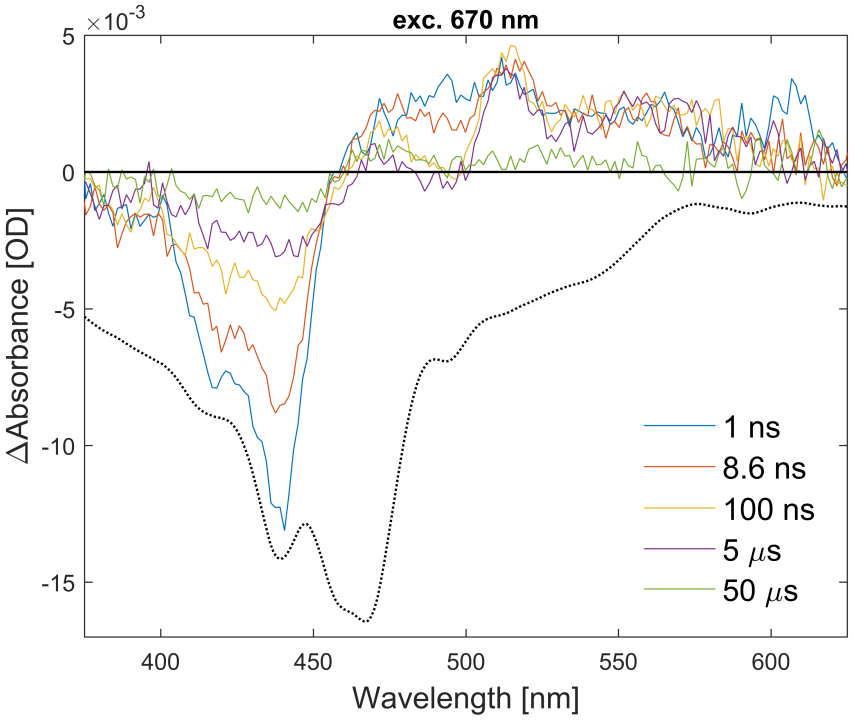

Figure 3.9: Transient absorption spectra of the acpPC at 77 K with excitation at 670 nm. The inverted steady-state absorption spectrum at 77 K (black dotted line) is shown for comparison.

Figure 3.9 presents TA spectra at 77 K of a sample excited at 670 nm. The spectra exhibit a lower S/N ratio compared to the RT measurement. However, the main features of the acpPC time-resolved evolution are well resolved. The region of the Soret band bleaching has a more pronounced structure and it quickly decreases in time. Contrary to the RT spectra, the maximum of the Soret band at ≈440 nm is visible even in the spectrum at 100 ns. The broad band from 460 to 525 nm assigned to singlet ESA of Chl *a* also quickly decays and is replaced by

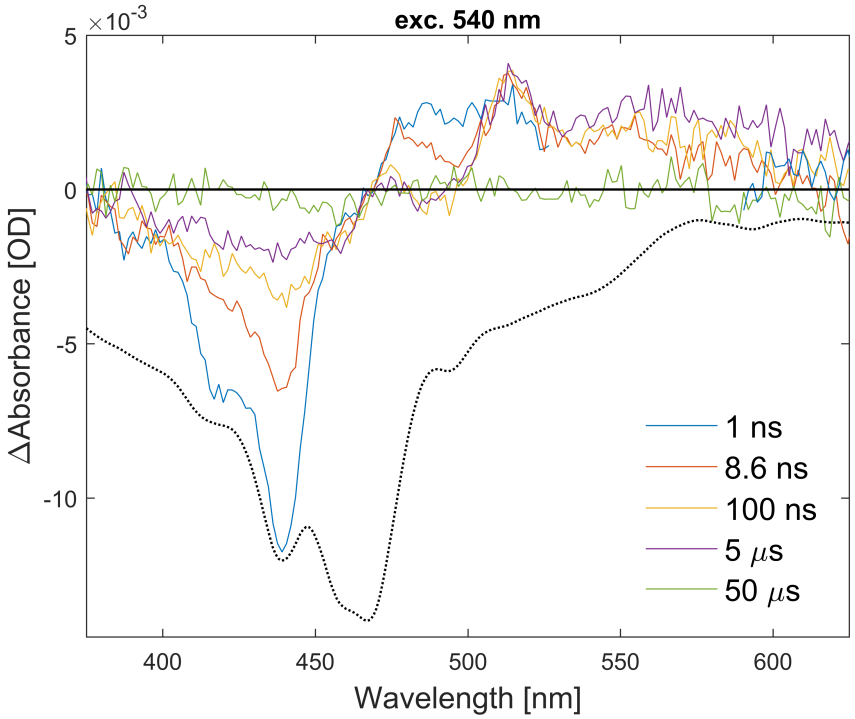

Figure 3.10: Transient absorption spectra of the acpPC antenna at 77 K with excitation at 540 nm. The inverted steady-state absorption spectrum at 77 K (black dotted line) is shown for comparison.

two triplet ESA bands of carotenoids with maxima at 475 nm and 510 nm. The signal of broad band with maxima at ≈560 nm rises during the first 200 ns. The spectrum at 1 ns also shows the strong band with a maximum at 610 nm, which is assigned to singlet ESA of Chl *a*. In the latter times, the spectral region between 450 −620 nm consists of spectral features assigned to carotenoids as in the case of the RT spectra. However, the evolution of the spectra is significantly slower. The prolongation of the carotenoid lifetime was expected, as the same feature was observed in LHC-II. Finally, the spectrum at 50 μs shows a structure indicating the presence of long-lived T_1 states of Chls, which will be better seen by global analysis in the next section.

Figure 3.10 shows the TA spectra of acpPC excited at 540 nm, where peridinin mainly absorbs. However, a small amount of Chl c_2 or diadinoxanthin is also excited. The laser signal around 540 nm was extracted from the spectrum with a 1 ns delay. There are minimal differences between excitation at 540 nm and 670 nm, same as in the case of LHC-II and different excitation wavelengths. The minor differences are the weaker singlet ESA band of Chl *a* with a maximum at 610 nm. The lower ESA around 610 nm is most likely due to the laser scattering.

Figure 3.11 presents a comparison of the TA spectra colour maps for both excitations at 670 nm (Left) and 540 nm (Right) in the whole measured spectral region. Except for the laser pulse detected as a blue spot around 540 nm, both figures show the same features in the spectral region between 375 −630 nm. The situation is different above 630 nm. In the first 40 ns, the region exhibit a strong signal from the fluorescence of Chl *a*, which is also observed in the RT spectra. However, the RT spectra show decay of the band with a maximum at 680 nm at

initial 40 ns. On the contrary, the band is prolonged to ≈250 ns at 77 K. Also, there are signs of a weak negative signal at even later times. The weak signal can also be observed in LHC-II, and it is most likely connected to a so called interaction peak [100, 101] or the GSB of the Q_y band of long-lived Chls. In the case of excitation at 540 nm, fluorescence of Chl c_2 can be noticed at ≈650 nm. However, the excitation from Chl c_2 should be transferred to Chl a within 1 ns according to [9, 11]. No fluorescence from Chls c_2 was observed at RT. Therefore, the fluorescence must be emitted by Chls c_2, which cannot transfer their energy to the Chls a due to a lower efficiency of the singlet-singlet ET at a low temperature.

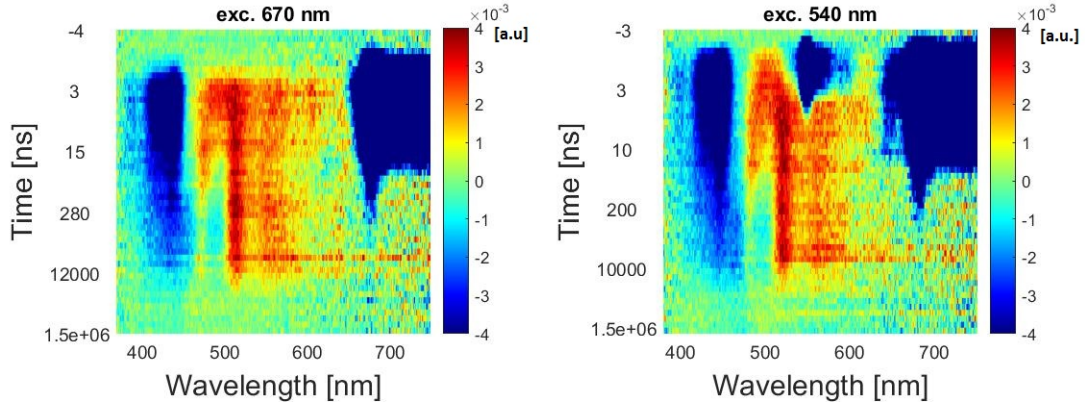

Figure 3.11: Transient absorption spectra of the acpPC antenna at 77 K with excitation at 670 nm (Left) and 540 nm (Right).

In summary, the main features of the transient absorption spectra at RT are preserved at 77 K. However, some new features are visible, which are discussed with help of a global analysis in next section.

Decay associated spectra at 77 K

As in the previous sections, the region above 630 nm is omitted from the global analysis at the short delays, when it is dominated by fluorescence. As we are interested in the strong band at 680 nm, the whole spectral region between 370 −740 nm is also analysed separately for delays >40 ns.

The transient spectra at 77 K of a sample excited at 670 nm require four components to obtain a satisfactory fits. Figure 3.12 presents the result of the fitting. The lifetimes of the DAS are estimated to be 5.9(7) ns for the (1.) component (blue line), 137(15) ns for the (2.) component (red line), 15.0(6) μs for the (3.) component (orange line), and 2.5(7) ms for the (4.) component (purple line).

The fastest (1.) component of the DAS exhibits a strong negative bleaching between 400 and 460 nm assigned to the decay of the Soret band of Chl a, and a positive singlet ESA band in the spectral regions of 460 −530 nm and 595 −630 nm. A sharp minima at 475 nm and 520 nm are ascribed to the increasing signal of the triplet ESA of carotenoids. The component shows that a subpopulation of Chl a is quenched by carotenoids with the same rate as at RT. Also, the lifetimes of the (1.) components at RT and 77 K are similar. However, the RT DA spectrum shows a negative shallow band with a maximum at ≈560 nm (see figure 3.8, Right), which is not observed in the case of the (1.) spectrum at

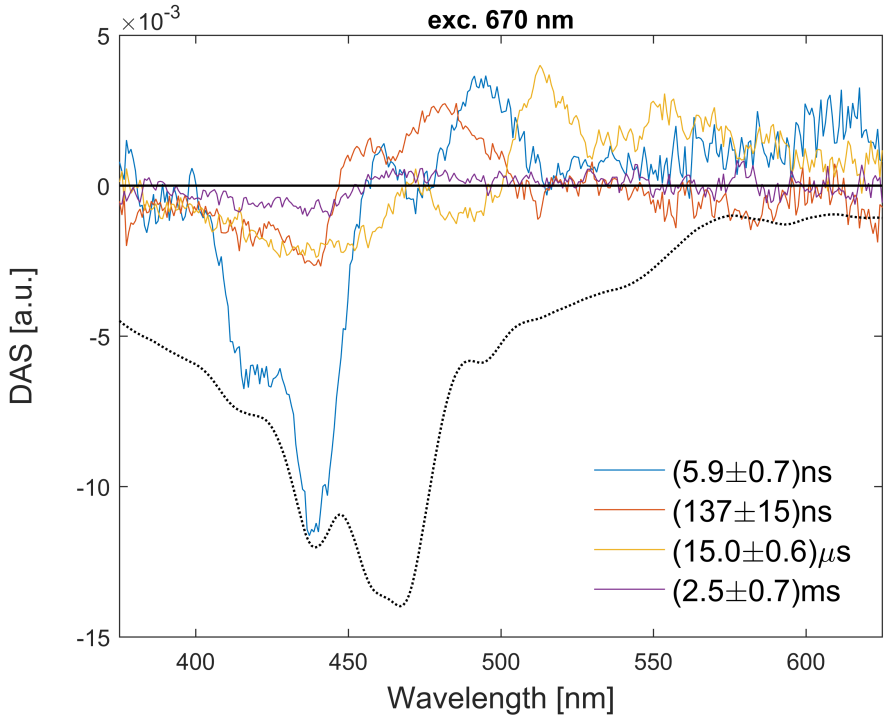

Figure 3.12: Decay associated spectra (DAS) of acpPC antenna at 77 K with excitation at 670 nm. The inverted steady-state absorption spectrum at 77 K (black dotted line) is shown for comparison.

77 K. The broad band was ascribed to peridinins in polar environment, which are apparently not able to quench triplets of Chl *a* with the same rate as at RT.

The (2.) component of the DAS must be added to obtain a good fit. The component is also shown in figure 3.13 (A) in the full spectral range. The area of the Soret band shows a negative signal with a maximum at the same wavelength (≈439 nm) as the ≈6 ns component. The blue shifted ESA in the spectral region between 446 −530 nm compared to the fast component and the lifetime of ≈140 ns, which is several times higher than a lifetime of Chl *a* singlet, suggest that the Chls *a* are in the triplet states. Therefore, the positive signal in the spectral region between 446 −530 nm seems to have origin in the triplet ESA of Chl *a* with two sharp minima at 468 and 515 nm due to the triplet ESA of carotenoids. The minima at 468 nm and 515 nm are blue-shifted compared to the minima at 475 nm and 520 nm in the (1.) component, which indicates that a different subpopulation of carotenoids is involved in the formation of the (2.) component. The ESA bands correspond to peridinin in non-polar environment, or diadinoxanthin. Also, the negative shallow band ascribed to peridinin in the polar environment is obvious with a maximum at ≈560 nm. The strong band with a minimum at 680 nm is observed in the full DA spectrum; see figure 3.13. The band is approximately three times higher than the GSB in the region of the Soret band. Therefore, it cannot be explained by the GSB of the Q_y band or by the interaction peak of carotenoids with Chls. We propose that the band has its origin in stimulated emission, which can be fitted simultaneously with the rest of the spectrum. However, the stimulated emission should not be observed, as we expect that the Chls are in the triplet states. In the next section, we

show a mechanism based on triplet-triplet annihilation, which can explain the observation.

The ≈15 μs component of DAS in figure 3.12 (orange line) shares most of the features with the slow component in the RT measurement, and is connected to the decay of the carotenoid triplets. The DA spectrum consists of a shallow negative band between 400 −500nm assigned to the carotenoid GSB, two positive sharp bands with maxima at 472 and 514 nm ascribed to the triplet ESA of carotenoids, and a broad ESA band of peridinin in a polar environment. The spectrum shows a zero signal above 600 nm (see 3.13 (B)), where we would expect the interaction peak. The spectral region between 460 −600 nm is a mirror image of the combination of the both nanosecond components of DAS. Obviously, the ≈15 μs spectrum is a mix of two components with similar lifetimes, which describes the deactivation of the excited triplet states of carotenoids, which are populated by the both nanosecond components.

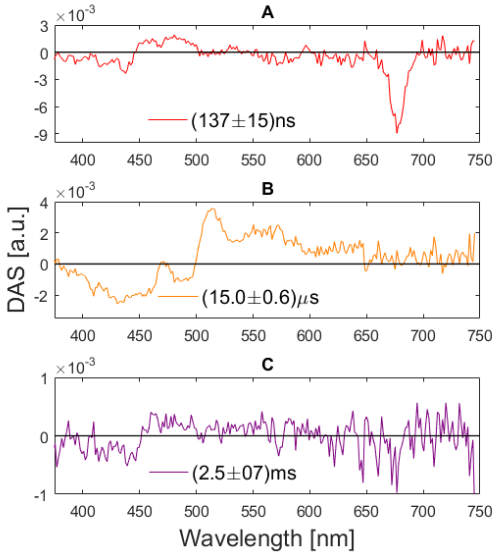

Figure 3.13: The components of the decay associated spectra from the acpPC antenna at 77 K and an excitation of 670 nm in a spectral range between 375 −750 nm. The transient absorption data with a delay < 40 ns were fitted separately.

The last millisecond component has a typical structure of a Chl *a* triplet transient spectrum with the Soret, ESA and Q_y bands (see figure 3.13 (C)).

The result of the global analysis of the TA spectra from a sample excited at 540 nm is shown in figure 3.14. The DAS are the same for (1.), (2.) and (3.) components. However, the millisecond component shows a features of Chl c_2 in the triplet state with a minimum of the Soret band at 465 nm. The lifetime of the component is also around ≈3 ms. In the previous subsection, we observed fluorescence from Chls c_2 and explained it through the subpopulation, which cannot transfer the energy to the central Chls. Apparently, some Chls c_2 from the subpopulation undergo transition to the triplet state, the lifetime of which is in a milliseconds range because no active carotenoid is situated in their neighbouring at 77 K. The population of long-lived triplets of Chl c_2 is around <7 %. The population was estimated from the TA spectra analysis.

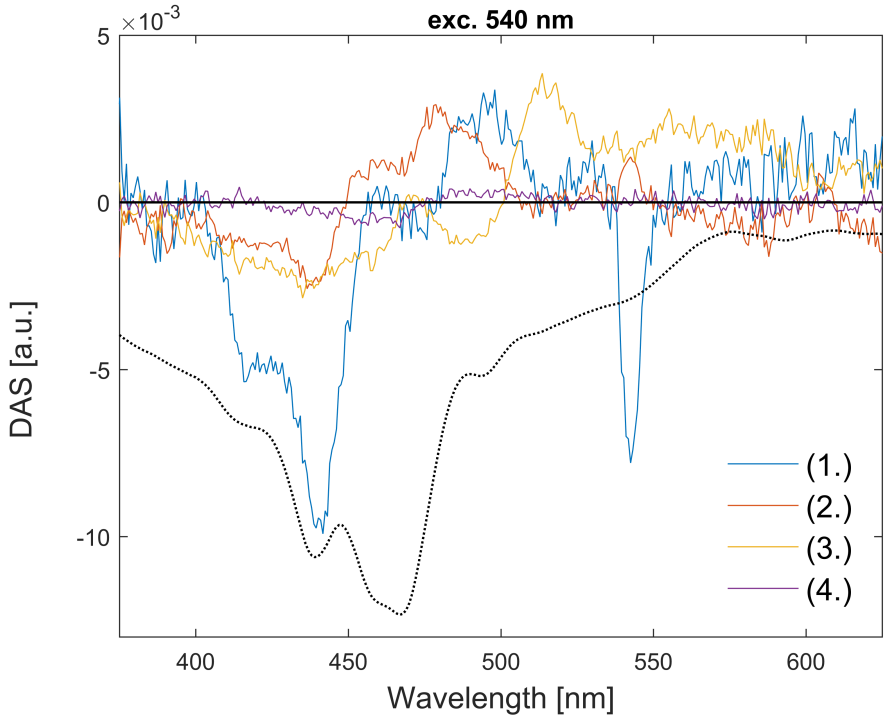

Figure 3.14: Decay associated spectra (DAS) of the acpPC antenna at 77 K with excitation at 540 nm. The inverted steady-state absorption spectrum at 77 K (black dotted line) is shown for comparison.

The comparison of transient spectra of acpPC and LHC-II show several outcomes:

1) Carotenoids, most likely luteins, involved in quenching of the triplet states of Chl in LHC-II show a fast quenching independent on temperature. The same observation is made in acpPC for a subpopulation of carotenoids. These carotenoids in acpPC are most likely peridinins in non-polar environment (or diadinoxanthin).

2) In the acpPC complex, the peridinins in a polar environment and a subpopulation of peridinins in a non-polar environment (or diadinoxanthin) show a strong dependence on temperature, influencing their ability to quench the Chl triplets.

3) The triplet states of Chl with millisecond lifetimes have their origin in peripheral Chls, which cannot transfer the excitation to the central Chls. Simultaneously, they cannot be neighbouring with an carotenoid active at 77 K.

Our conclusions show at least three subpopulations of carotenoids in the acpPC antenna involved in Chl triplet quenching. We would like to repeat that three spectrally-shifted subpopulations of peridinin were resolved through the deconvolution of the steady-state absorption spectrum of acpPC in [9]. The involvement of diadinoxanthin in the quenching cannot be absolutely excluded. However, its low stochiometry and the spectrally shifted ESA notches in both nanosecond components ((1.) comp.: 475 and 520 nm, (2.) comp.: 468 and

515 nm), which seems to be caused by the same type of carotenoid in a little bit different environment, illustrate that most likely only peridinins are involved in the quenching. The lower efficiency of the quenching (quenched Chl triplets by carotenoids/populated Chl triplets) at a low temperature is not due to lower rate of DET. However, it is due to the trapping of excitation in peripheral Chls.

Delayed fluorescence

The strong negative band of the (2.) component visible around 680 nm is certainly connected to the Chl *a*. However, due its magnitude relatively to the Soret band GSB and lifetime, it cannot be explained as the GSB of Chl *a* or an interaction peak. We have measured the prompt fluorescence at 77 K. The lifetime of the prompt fluorescence was determined to be 5.6(2) ns, which is in accordance with the previously-reported results and with the previous subsection. [9, 34] As expected, the prompt fluorescence did not exhibit a lifetime around ≈150 ns. Therefore, we were looking for another mechanism, which could cause the strong band.

Such a mechanism can be triplet-triplet annihilation (TTA), which results in the emission of delayed fluorescence (DF). For measure DF, experimental settings had to be changed to a higher gain of iCCD camera (≈100 Gain at 77 K vs. ≈75 Gain at RT) and a longer gate width (50 ns). The temperature was kept at 77 K. The first delay was set to 100 ns, when a prompt fluorescence should not play any significant role. The sample was excited at 460 nm to prevent any confusion of the DF with a laser scattering from the optical fibres or lenses.

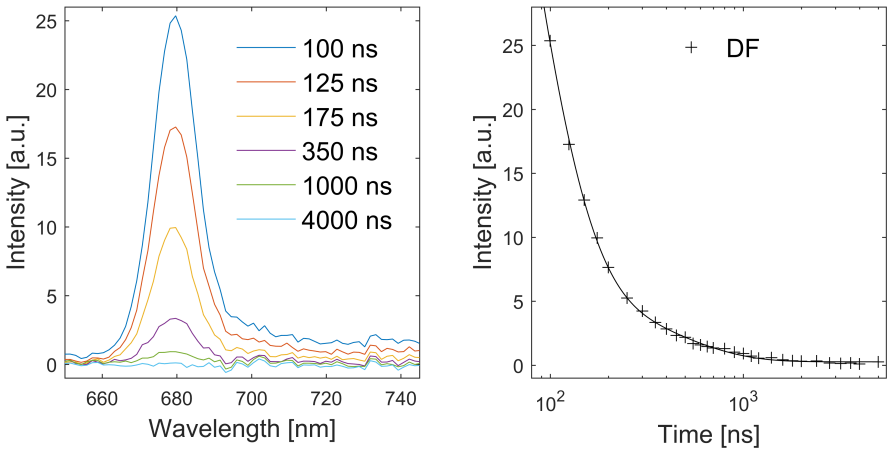

Figure 3.15: The delayed fluorescence (DF) of acpPC at 77 K upon excitation at 460 nm. (Left) DF spectra in different delays. (Right) DF kinetics at 680 nm were fitted by biexponential function.

Figure 3.15 shows that DF can be detected even at 1 μs, when the prompt fluorescence intensity is proportional to $\approx \exp\left(-\frac{1000}{5}\right)$, which is definitely under our S/N ratio. The DF signal is satisfactorily fitted by two components with lifetimes of ≈60 ns and ≈540 ns, and amplitudes ≈ 110 a.u. and ≈ 7 a.u., respectively. The measurement proves that the singlet states of Chl *a* are generated in late times in acpPC.

The DF is generated most likely through TTA. In TTA, one molecule in a triplet state relaxes to the ground state by transferring its energy to the other triplet, which is converted back to the singlet state. The other two well-known mechanisms - thermally activated DF and singlet oxygen feedback-induced DF - are likely not involved due to the low temperature, a high viscosity and no interaction with oxygen. [102] The strong signal in the TA spectra at ≈680 nm and 40 −100 ns cannot be directly TTA DF, which exhibits only a weak signal. TTA DF is used only as a generator of singlet states of Chl *a*, which are depopulated by a probe flash as a stimulated emission.

The function, which describes the evolution of TTA DF, can be solved directly from differential equations. In general, the result is not a sum of exponential functions. Therefore, it is necessary to discuss if the fitting by an exponentials is appropriate in this situation. Several arguments can be used to justify the exponential fit, which describes DF generated by TTA:

1) The exponential functions are good estimates for the unknown evolution of DF, especially when the DF decay is not a monoexponential function. In this case, the identified lifetimes have no physical meaning.

2) If TTA is not a significant relaxation path for Chl triplets, and the other rates are independent on their concentration, then the triplets decay as a monoexponential function with the lifetime τ, and the TTA DF lifetime is $\tau_{TTA} = \frac{\tau}{2}$. [102]

The second argument seems to be the most interesting as we presume that the main pathway for Chl triplet relaxation is quenching by carotenoids. Moreover, the lifetime ≈60 ns is close to half of the lifetime belonging to the (2.) component. However, the exponential decay with the lifetime ≈540 ns would have to be connected to a different subpopulation of Chl triplets, which was not observed in the previous chapters. The measurement should be taken as a proof of the principle, especially when we did not considered reabsorption, which can influence the estimated lifetimes.

Temperature dependence

The temperature dependence of the lifetimes of the DAS components was estimated for different temperatures between 77 K and RT. The sample was always excited at 670 nm.

The lifetime of the (1.) component gives almost the same value of the lifetime ≈5.7 ns, independent of temperature, which is similar to the situation in LHC-II, where only an insignificantly small prolongation was observed. The lifetime of the component is mainly given by the lifetime of the singlet state of Chl *a*.

The lifetime of the (2.) component is fitted by equation 1.13, as presumably it illustrates the direct dependence of the DET rate on temperature. The fit shape is in a good agreement with experimental results. Calculated $\Delta G^{\dagger}$ is equal to $\approx 11\ \mathrm{kJ \cdot mol^{-1}} \Rightarrow 0.1$ eV. The rate of DET significantly depends on temperature above 150 K. The rate is at least 1000× higher at RT compared to 77 K. The lower rate of DET between Chls and peridinins seems to have its origin in the intrinsic temperature dependence of Dexter energy transfer.

The temperature dependencies of the (3.) and (4.) components are fitted by the Arrhenius law as presumably they reflect a rate of relaxation of excited triplets to the ground states by ISC. [98] The signal of the (4.) component cannot be detected above 200 K, and the (3.) component shows highly-specific temperature dependence. The (3.) component seems to be independent of temperature between 200 −250K, with a constant lifetime around ≈9 μs. The lifetime is similar to detected lifetime under anaerobic conditions at RT. [12] We suggest that the independence in acpPC is due to no oxygen accessibility to carotenoids in the frozen sample. The chart shows that the lifetimes below 175 K is getting longer with decreasing temperature. The situation is different compared to LHC-II, where the lifetime of the μs component is independent of temperature below 200 K and then decreases to RT value.

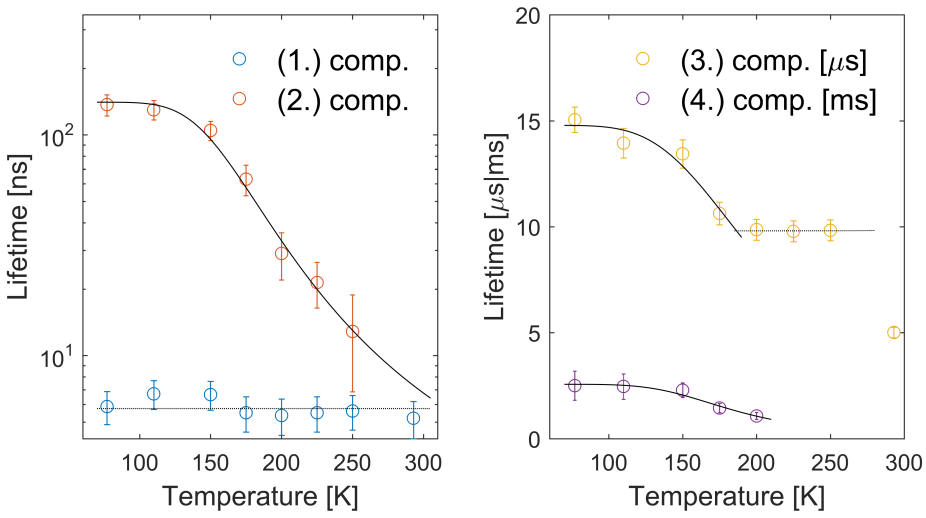

Figure 3.16: Temperature dependence of lifetimes of decay-associated spectra components. Transient spectra were measured with excitation at 670 nm.

The acpPC complex excited at 460 nm

Kvíčalová et al. in [12] resolved two spectrally-shifted components, which were assigned to the relaxation of carotenoids, upon excitation at different wavelengths. The excitation at 460 nm resulted in a red shift of GSB and the triplet ESA band (≈475 nm) of carotenoids compared to the excitations at 540 or 670 nm. In the article, they propose that the excitation at 460 nm uses another pathway, which is quenched by a different subpopulation of carotenoids. Therefore, we excited a cooled sample (77 K) at 460 nm to observe the spectrally-shifted component.

Several measurements were performed with the same result shown in figure 3.17. The result corresponds to the previous figures 3.12 and 3.14. The (1.) component is deformed by a laser pulse at 460 nm. The (3.) component is not spectrally shifted, and it is exactly the same as in the case of excitation at 670 or 540 nm. However, a strong signal from the Chl c_2 triplets is observed from the (4.) component. According to the observation, we suggest that the spectral shift reported by Kvíčalová et al. was not due to a different type of carotenoid. However, it is shifted due to a mixing of signals from carotenoids and free Chls

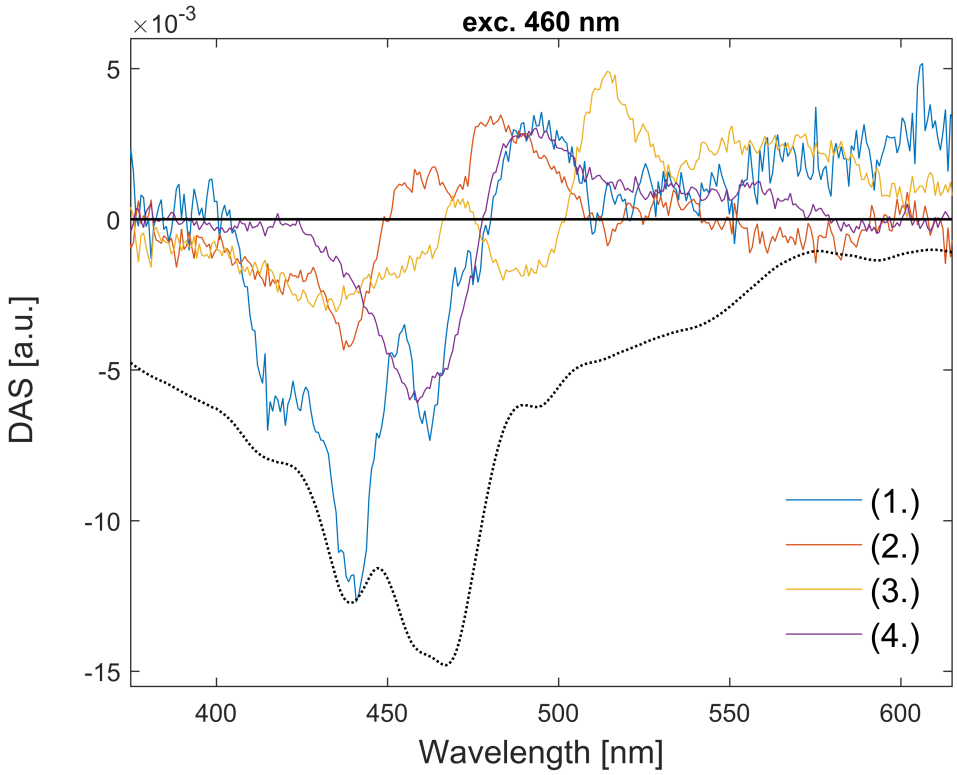

Figure 3.17: The decay associated spectra (DAS) of acpPC at 77 K with excitation at 460 nm. The inverted steady-state absorption spectrum at 77 K (black dotted line) is shown for comparison.

c_2. We conclude that the Chls c_2 are presented in two forms: free Chls c_2, which are not bound to the protein complex and the Chls c_2, which cannot tranfer the excitation to Chls a at 77 K. The population of long-lived triplets of Chl c_2 is around ≈26 %. The hypothesis is further confirmed by the differences of the two reported components of DAS shown in the paper of Kvíčalová et al., which show the exact shape of the T-S spectrum assigned to Chl c_2. [12]

3.3 Chlorosomes of *Chloroflexus aurantiacus*

3.3.1 Steady-state absorption spectra

The steady-state absorption spectra of chlorosomes from *Clf. aurantiacus* at RT and 77 K are shown in figure 3.18. Both absorption spectra were taken on the same sample in the cryostat in the spectral region between 300 −900 nm.

The RT absorption spectrum exhibits a strong absorption band with the maximum at 464 nm and sidebands at ≈400 and ≈500 nm. The peak centered at 464 nm is ascribed to the Soret band of BChl *c* and its vibronic structure with a significant contribution of absorption of carotenoids and absorption of BChl *a* at shorter wavelengths. The maximum of the BChl *c* Q_y band is located at 742 nm. Also, a small band appears peaking at 797 nm, which is ascribed to the Q_y band of BChl *a*. The peak with the maximum at 596 nm is assigned to the Q_x band of BChl *a*. No appearence of an absorption band around 675 nm indicates that the complexes are intact. [87] The RT spectrum corresponds to previously published spectra. [103, 104, 105]

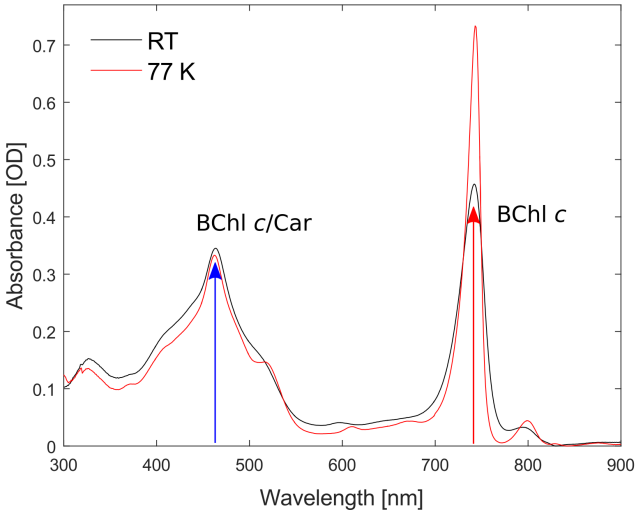

Figure 3.18: Steady state absorption spectra of chlorosomes from *Chloroflexus aurantiacus* at room temperature (RT, black line) and 77 K (red line).

The absorption spectrum at 77 K (red line) shows a significant enhancement of the Q_y absorption peak and enhanced vibronic resolution at shorter wavelengths. The major Soret/carotenoid band structure is presented with a well differentiable peak at 516 nm. The lower absorbance over the Soret band compared to the RT spectrum is probably due to the slightly different position of the cryostat in the absorption spectrometer. The Q_y and the Q_x bands of BChl *a* are red-shifted to 800 and 603 nm, respectively.

3.3.2 Transient absorption spectra between 77 K and room temperature

Transient absorption spectra at room temperature

The typical transient absorption spectra of chlorosomes at RT are shown in figure 3.19. Chlorosomes were excited at 465 nm (Left) and 740 nm (Right). The excitation wavelengths at 465 and 740 nm correspond to excitation of Bchl *c* and carotenoids, and only BChl *c*, respectively. Data binning by four points was used, because the TA spectra exhibit only a weak and noisy signal. The data from the spectral region between 450 and 475 nm was cut off from the TA spectrum at 1 ns (excitation at 465 nm) due to laser scattering.

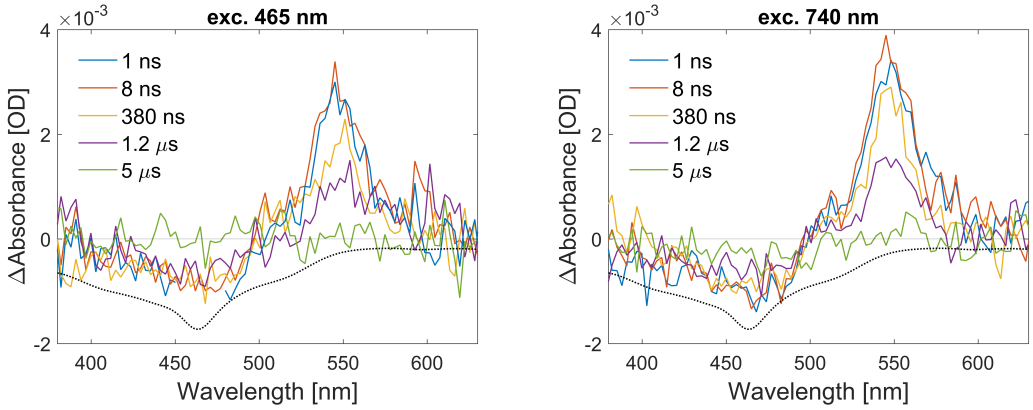

Figure 3.19: Transient absorption spectra of chlorosomes at room temperature (RT). The sample was excited at 465 nm (Left) and 740 nm (Right). Software data binning is used. The inverted steady-state absorption spectra at RT (black dotted line) are shown for comparison.

Both measurements illustrate the decay of carotenoids mainly represented by β-carotenes. The negative band with the maximum at 475 nm is ascribed to GSB of carotenoids. The positive peak with the maximum at 545 nm and sideband at ≈515 nm are ascribed to ESA of β-carotene triplets. [38] Both bands slowly decay with almost no signal detected after 5 μs. The spectra show no signs of the fast decay in contrary to the previously studied antennas.

Decay associated spectra at room temperature

Figure 3.20 presents DAS obtained from global analysis of TA spectra at RT. The TA spectra from chlorosomes excited at 465 nm (Left) are satisfactorily fitted by one component. The lifetime was estimated to be 1.4(2) μs. The spectral shape of the DA spectrum corresponds to the broad negative band at 400 −500 nm due to GSB of carotenoids and two ESA peaks of β-carotene with maxima at 515 and 545 nm. The DA spectrum obviously describes relaxation of carotenoid triplets.

The TA spectra of chlorosomes excited at 740 nm can be fitted by one or two components with the same χ^2. The fitting by two components is presented in figure 3.20 (Right) due to the comparison with low-temperature measurements. The spectral features and lifetime of the slower component of DAS are approximately the same as of the one for chlorosomes excited at 465 nm. A special measurement

with the grating centred at 700 nm was performed to detect the interaction peak of carotenoids and BChls *c*. [88, 87] The gain of the iCCD camera was set to a higher value (90 −110 Gain) due to the low intensity of the Xenon lamp above 700 nm. The TA spectra yielded a very noisy signal and, therefore, we present only the DA spectrum. The result of the global analysis is added to the figure and separated by a dashed line. A strong interaction peak with the maximum at 750 nm is shown, which decays with the same lifetime as the rest of the slower component.

The negative signal in the faster component between 400 −500 nm is ascribed to the Soret band with the maximum at 467 nm from decaying excited states of BChl *c*, overlapped with a rising positive signal from GSB assigned to carotenoids. The negative band centred at 550 nm and its sideband at ≈515 nm are mirror images to the triplet ESA of carotenoids of the slower DAS component. The spectrum and the lifetime of ≈3 ns of the fast component indicate that it represents triplet ET from BChls to carotenoids. However, the lifetime value should only be taken as an approximative number as it is close to our time resolution. Therefore, we cannot exclude that the real lifetime is even shorter, especially when we do not observe BChl spectral features at TA spectra.

The fast component cannot be resolved in the case of excitation at 465 nm due to strong laser scattering. For both excitation wavelengths, the component with the microsecond lifetime corresponds to previously reported spectra. [38, 87]

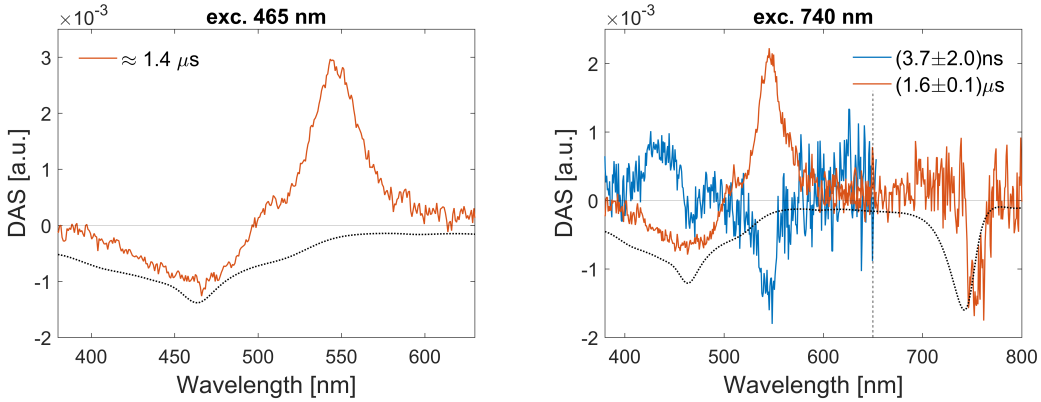

Figure 3.20: Decay associated spectra (DAS) of chlorosomes at 300 K. The sample was excited at 465 nm (Left) and 740 nm (Right). Software data binning is used. The inverted steady-state absorption spectra at 77 K (black dotted line) are shown for comparison.

Transient absorption spectra at 77 K

The TA spectra of chlorosomes at 77 K are represented by figure 3.21. The scattering of the laser at 465 nm was extracted from the spectrum at 1 ns in the left figure. Unfortunately, the scattering of the laser is overlapped with the early evolution of BChls *c*. Therefore, only a weak signal of BChl *c* seems to be located at ≈470 nm as a small negative peak in the spectrum at 8 ns. The later spectra show only a decay of carotenoids characterised by a negative GSB (400 −520 nm) and triplet ESA bands centred at 515 and 550 nm. The triplet ESA of carotenoids

at 550 nm is red-shifted compared to RT spectra. Enhanced vibronic resolution of the TA spectra reveals a new ESA band at ≈580 nm.

The scattering of the laser can be avoided by excitation at 740 nm, see figure 3.21 (Right). The spectrum at 1 ns (thick blue line) proves that the observed DA spectrum ascribed to the quenching of BChls *c* by carotenoids is a real. The spectrum exhibits a strong negative band at 470 nm arising from the Soret band bleaching of BChl *c*. The signal of BChl *c* is quickly replaced by a negative band assigned to GSB of carotenoids. BChls *c* exhibit only a weak signal compared to the previously antennas. The evolution of the TA spectra in late times corresponds to the relaxation of carotenoids, which is described in the preceding paragraph.

The problem of the strong laser scattering of the samples at 77 K in the case of excitation at 465 nm is partly due to the size of chlorosomes. Therefore, the temperature dependence of photoprotective efficiency in chlorosomes is measured with excitation at 740 nm.

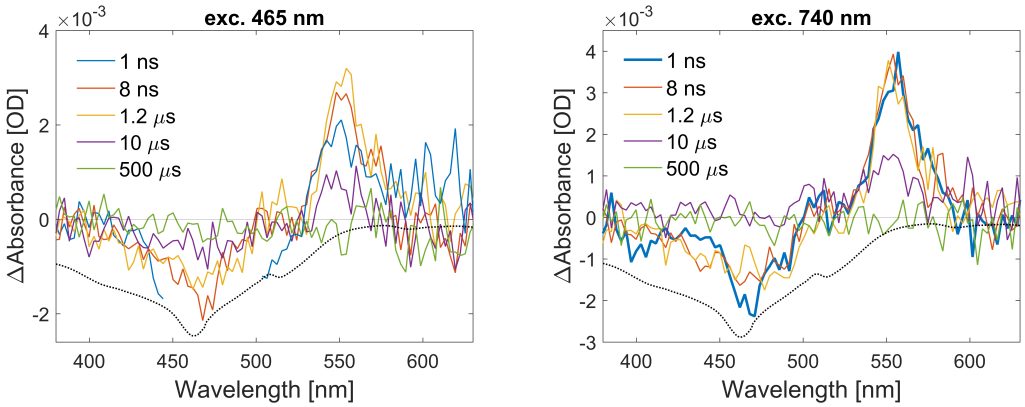

Figure 3.21: Transient absorption spectra of chlorosomes at 77 K. The sample was excited at 465 nm (Left) and 740 nm (Right). Software data binning is used. The inverted steady-state absorption spectra at 77 K (black dotted line) are shown for comparison.

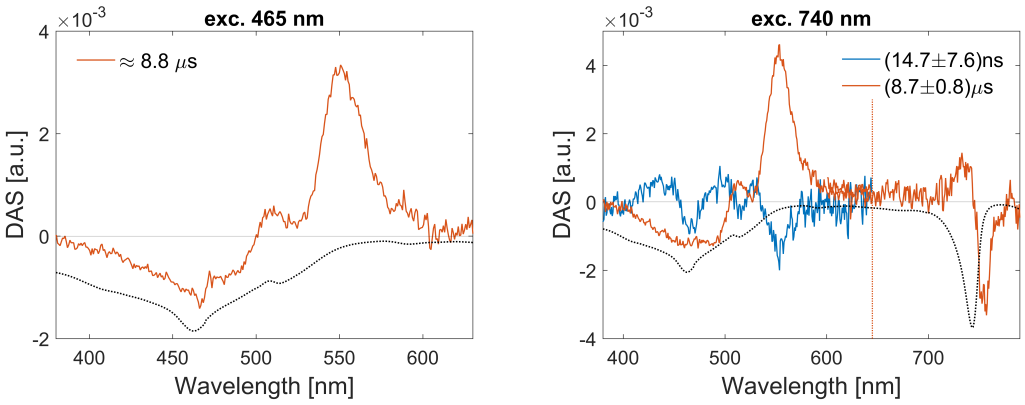

Figure 3.22: Decay associated spectra (DAS) of chlorosomes at 77 K. The sample was excited at 465 nm (Left) and 740 nm (Right). Software data binning is used. The inverted steady-state absorption spectra at 77 K (black dotted line) are shown for comparison.

Decay associated spectra at 77 K

The DAS obtained at 77 K are shown in figure 3.22. The TA spectra of the sample excited at 465 nm (Left) were fitted satisfactorily by one component as in the case of the RT spectra. However, the "zero lifetime component" of the laser exhibits higher width. This might be a result of strong scattering and the remains of the fast component. The one component illustrates the relaxation of carotenoid triplets with a significant prolongation of the lifetime to ≈8.8 μs.

Chlorosomes excited at 740 nm show the same component describing for the carotenoid relaxation with a similar lifetimes 8.7(8) μs. The major ESA band and interaction peak are narrower and red-shifted to 553 nm and 755 nm, respectively. The shape of the interaction peak is similar to the reported ones in [87, 88]. The faster component is presented with an enhanced spectral resolution compared to the DAS at RT. The component illustrates the ET from BChls to carotenoids. The meaning of the DA spectrum is the same as in the case of LHC-II and acpPC. However, the lifetime of 14.7(76) ns of the fast component is far beyond the reported lifetimes of the singlet state of BChl *a* and BChl *c* in solutions at 77 K. [106, 107] Moreover, the lifetime of the singlet state should be significantly shortened for the case of aggregated pigments. [78] Therefore, we suggest that we observe BChls in the T_1 state.

The long-lived BChl triplets with a millisecond lifetime are not observed contrary to acpPC and LHC-II .

.

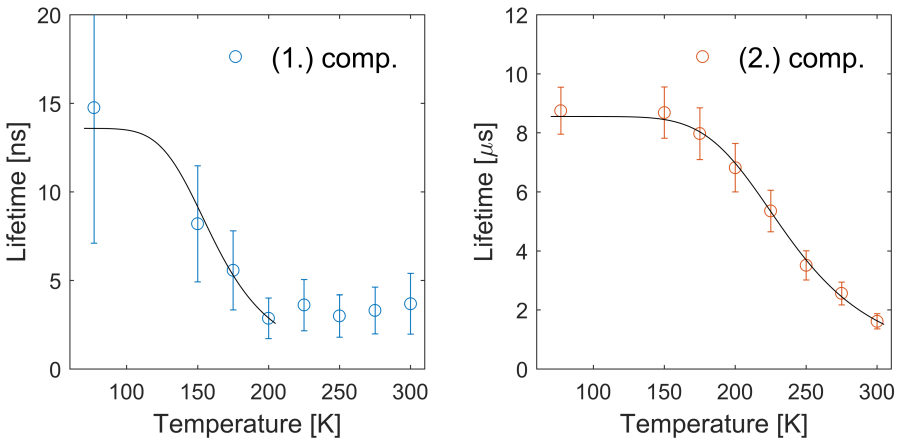

Figure 3.23: Temperature dependence of lifetimes of decay associated spectra components. Transient spectra were measured with excitation at 740 nm.

Temperature dependence

Figure 3.23 shows temperature dependence for both components of the DAS. The lifetime of the fast ns component seems to be a constant ≈3 ns above 200 K. The temperature dependence below 200 K exhibits a substantial rise of the lifetime to 14.7(76) ns. However, the values were estimated with a large error due to a weak noisy signal. Also, the laser width is ≈3 ns. Therefore, we suggest that the real lifetime above 200 K is much shorter. The data below 200 K are fitted by

equation 1.13 as we presume that the signal of the fast component describe DET from BChl triplets to carotenoids.

Temperature dependence of the lifetime of carotenoid triplets represented by the μs slower component is shifted compared to the ns component. The rise of the lifetime from 1.6(1) μs at RT to $\approx$8 μs at 175 K is followed by a constant dependence at lower temperatures. The lifetime of carotenoid triplet relaxation at 77 K is significantly shorter compared to the other antennas, which shows that the carotenoids must be in stronger interaction with the surrounding environment. The data are fitted by the Arrhenius equation.

Chlorosomes show different results in comparison with acpPC and LHC-II, which illustrates that the structure and the presence of a protein scaffold of LHC plays an important role in the photoprotective mechanisms.

Conclusion

In summary, our results show significant differences among the three selected antennas in their ability to quench Chl or BChl triplets at temperatures between 77 K and RT.

All three antennas show ≈100 % efficiency of the excitation transfer from Chl or BChl triplets to carotenoids at RT, which is in accordance with the previously reported results [8, 12, 87]. The apparent lifetime (≈5 ns) of the Chl triplets in acpPC and LHC-II at RT is given by the Chl singlet lifetime, which is a consequence of the fact that the intrinsic rate of DET is fast enough to prevent any accumulation of Chl triplets. Chlorosomes exhibit an even shorter lifetime of the fast component of DAS at RT. The high rate of quenching of Chl triplets in LHC-II seems to be independent of temperature, whereas the acpPC complex and chlorosomes exhibit a significant rate decreases at low temperatures.

In acpPC, two components of DAS at 77 K were assigned to energy transfer from Chl triplets to three subpopulations of carotenoids, most likely peridinins. One subpopulation formed by peridinins in a non-polar environments is able to quench Chl triplets with a rate independent of temperature. The other two subpopulations show a significant decrease of the quenching rate resulting in the lifetime of Chl triplets equal to ≈140 ns at 77 K. The decrease of the quenching rate is most likely connected to its intrinsic dependence on temperature. We presume that the two subpopulations involved in the strongly temperature-dependent quenching are formed by peridinins in a polar and non-polar environment according to the observed spectral features in the corresponding DAS. The ≈140 ns component of DAS and TA spectra of acpPC exhibit strong band at 680 nm, origin of which was explained by stimulated emission of Chl *a*. We propose a mechanism of the generation of the S_1 states of Chl *a* at late nanosecond times based on triplet-triplet annihilation. A decrease in the quenching rate was also observed in chlorosomes. However, the quenching rate seems to be less effected as the lifetime of Chl triplets is ≈14 ns at 77 K.

In addition, we have also observed the long-lived triplets of Chl with a millisecond lifetime in acpPC and LHC-II at temperatures below 200 K. We suggest that the long-lived triplet states of Chls are located at the periphery of LHC and are unable to transfer the singlet excitation to central Chls at 77 K. At the same time any nearby carotenoid is not able to quench the long-lived Chl triplets at 77 K. We observed that the efficiency of quenching of all Chl triplets in LHC-II is >95 % at 77 K, which is in accordance with [8]. The efficiency of the quenching in acpPC is strongly dependent on the excitation wavelength. The population of long-lived triplets is around <7 % in the case of the excitation of Chl *a* and peridinin. On the contrary, in the case of the excitation of Chl c_2 around ≈26 % of excitations is trapped on them. The results suggest that the position of Chls c_2 is in the periphery of the protein complex and most likely some free Chl c_2 molecules, which are not functionally connected to the acpPC complex, are present at the sample.

The three selected antennas exhibit also different temperature dependence of carotenoid triplet relaxation via ISC to the ground state. The LHC-II antenna and chlorosomes show the same dependence, which can be easily fitted by the

Arrhenius equation. Both complexes show a smooth prolongation of lifetimes with a decreasing temperature, which is followed by saturation at ≈12 μs (200 K) for LHC-II and ≈9 μs (150 K) for chlorosomes. The situation is different in acpPC, which is most likely due to a different protein structure compared to LHC-II. This results in the constant value of the lifetime (≈9 μs) between 200 and 250 K.

We also confirm the double exponential decay of carotenoids in the LHC-II under aerobic conditions as reported in [8, 14]. Moreover, we have explained the origin of two spectrally-shifted components assigned to the relaxation of carotenoids in acpPC, which were reported in [12]. The observed spectral shift is due to the signal from Chl c_2 triplets, which were most likely present as free monomers in the sample.

Minor outcomes of this thesis are the attached guidelines for measurements with the cryostat, modification of the setup for low-temperature measurements, the sample holder for thin quartz low-temperature cuvettes and the holder of the cryostat in the steady-state absorption spectrometer.

Bibliography

[1] D. G. Nocera. The artificial leaf. *Accounts of Chemical Research*, 45(5):767–776, 2012.

[2] R. E. Blankenship. *Molecular mechanisms of photosynthesis*. Blackwell Science Ltd., 2002.

[3] L. Dall'Osto, C. Lico, J. Alric, G. Giuliano, M. Havaux, and R. Bassi. Lutein is needed for efficient chlorophyll triplet quenching in the major LHCII antenna complex of higher plants and effective photoprotection in vivo under strong light. *BMC plant biology*, 6(1):32, 2006.

[4] B. Halliwell and J. M. C. Gutteridget. Oxygen toxicity, oxygen radicals, transition metals and disease. *Biochem. J*, 219:1–14, 1984.

[5] S. M. Theg and F.-A. Wollman. *Plastid Biology*. Springer New York Heidelberg Dordrecht London, 2014.

[6] A. A. Pascal, Z. Liu, K. Broess, B. van Oort, H. van Amerongen, C. Wang, P. Horton, B. Robert, W. Chang, and A. Ruban. Molecular basis of photoprotection and control of photosynthetic light-harvesting. *Nature*, 436(7047):134–137, 2005.

[7] A. V. Ruban, R. Berera, C. Ilioaia, I. H. M. van Stokkum, J. T. M. Kennis, A. Pascal, H. van Amerongen, B. Robert, P. Horton, and R. van Grondelle. Identification of a mechanism of photoprotective energy dissipation in higher plants. *Nature*, 450(7169):575–578, 2007.

[8] E. J. G. Peterman, F. M. Dukker, R. van Grondelle, and H. van Amerongen. Chlorophyll *a* and Carotenoid Triplet States in Light-Harvesting Complex II of Higher Plants. *Biophys. J.*, 69(6):2670–2678, 1995.

[9] D. M. Niedzwiedzki, J. Jiang, C. S. Lo, and R. E. Blankenship. Spectroscopic properties of the Chlorophyll *a*-Chlorophyll c_2-Peridinin-Protein-Complex (acpPC) from the coral symbiotic *dinoflagellate Symbiodinium*. *Photosynthesis Research*, 120(1-2):125–139, 2014.

[10] C. B. Field. Primary Production of the Biosphere: Integrating Terrestrial and Oceanic Components. *Science*, 281(5374):237–240, 1998.

[11] T. Polívka, I. H. M. van Stokkum, D. Zigmantas, R. van Grondelle, V. Sundström, and R. G. Hiller. Energy transfer in the major intrinsic light-harvesting complex from *Amphidinium carterae*. *Biochemistry*, 45(28):8516–8526, 2006.

[12] Z. Kvíčalová, J. Alster, E. Hofmann, P. Khoroshyy, R. Litvín, D. Bína, T. Polívka, and J. Pšenčík. Triplet-triplet energy transfer from chlorophylls to carotenoids in two antenna complexes from *dinoflagellate Amphidinium carterae*. *Biochimica et Biophysica Acta - Bioenergetics*, 1857(4):341–349, 2016.

[13] D. M. Niedzwiedzki, J. Jiang, C. S. Lo, and R. E. Blankenship. Low-temperature spectroscopic properties of the peridinin-chlorophyll *a*-protein (PCP) complex from the coral symbiotic *dinoflagellate symbiodinium*. *Journal of Physical Chemistry B*, 117(38):11091–11099, 2013.

[14] M. Mozzo, L. Dall'Osto, R. Hienerwadel, R. Bassi, and R. Croce. Photoprotection in the antenna complexes of photosystem II: Role of individual xanthophylls in chlorophyll triplet quenching. *Journal of Biological Chemistry*, 283(10):6184–6192, 2008.

[15] D. Carbonera, E. Bordignon, G. Giacometti, G. Agostini, A. Vianelli, and C. Yannini. Fluorescence and absorption detected magnetic resonance of chlorosomes from green bacteria *chlorobium tepidum* and *chloroflexus aurantiacus*. A comparative study. *Journal of Physical Chemistry B*, 105(1):246–255, 2001.

[16] B. R. Green, J. M. Anderson, and W. W. Parson. *Photosynthetic Membranes and Their Light-Harvesting Antennas*, pages 1–28. Springer Netherlands, Dordrecht, 2003.

[17] T. Renger. Theory of excitation energy transfer: From structure to function. *Photosynthesis Research*, 102(2):471–485, 2009.

[18] L. N. M. Duysens. *Transfer of excitation energy in photosynthesis*. Kemink Utrecht, 1952.

[19] N. J. Turro, V. Ramamurthy, and J. C. Scaino. Energy and Electron Transfer. In *Principles of Molecular Photochemistry: An Introduction*, volume 6, chapter 7, pages 383–483. University Science Books, USA, 2004.

[20] J. G. Vos, R. J. Foster, and T. E. Keyes. Theoretical Framework for Electrochemical and Optical Processes. In *Interfacial Supramolecular Assemblies*, chapter 2, pages 9–48. John Wiley & Sons, Ltd., Chichester, 2003.

[21] M. Şener, J. Strümpfer, J. Hsin, D. Chandler, S. Scheuring, N. Hunter, and K. Schulten. Föster energy transfer theory as reflected in the structures of photosynthetic light harvesting systems. *Chemphyschem.*, 12(3):518–531, 2012.

[22] H. H. Jaffe and A. L. Miller. The fates of electronic excitation energy. *J. Chem. Educ*, 43(9):469, 1966.

[23] M. Kasha. Energy Transfer Mechanisms and the Molecular Exciton Model for Molecular Aggregates. *Radiat. Res.*, 20(1):55–71, 1963.

[24] L. Skála. *Kvantová teorie molekul*. Karolinum, 1994.

[25] W. S. Struve. *Theory of Electronic Energy Transfer*, pages 297–313. Springer Netherlands, Dordrecht, 1995.

[26] L. Sudha Devi, M. K. Al-Suti, C. Dosche, M. S. Khan, R. H. Friend, and A. Köhler. Triplet energy transfer in conjugated polymers. I. Experimental investigation of a weakly disordered compound. *Physical Review B - Condensed Matter and Materials Physics*, 78(4):1–8, 2008.

[27] E. Hückel. Quantentheoretische Beiträge zum Benzolproblem - I. Die Elektronenkonfiguration des Benzols und verwandter Verbindungen. *Zeitschrift für Physik*, 70(3-4):204–286, 1931.

[28] J. Zamastil and J. Benda. *Kvantová mechanika a elektrodynamika*. Charles University in Prague, Karolinum Press, Prague, 2016.

[29] J. R. Lakowicz. *Principles of Fluorescence Spectroscopy Principles of Fluorescence Spectroscopy*. Springer, 2006.

[30] M. Nepraš and M. Titz. *Základy teorie elektronových spekter*. Nakl. techn. lit., 1983.

[31] M. O. Senge, A. A. Ryan, K. A. Letchford, S. A. MacGowan, and T. Mielke. Chlorophylls, symmetry, chirality, and photosynthesis. *Symmetry*, 6(3):781–843, 2014.

[32] G. P. Gurinovich, A. N. Sevchenko, and K. N. Solov'ev. The Spectroscopy of the Porphyrins. *Usp. Fiz. Nauk*, 79(1):173–234, 1963.

[33] V. N. Nemykin and R. G. Hadt. Interpretation of the UV - Vis spectra of the meso (ferrocenyl)-containing porphyrins using a TDDFT approach: Is Gouterman's classic four-orbital model still in play? *Journal of Physical Chemistry A*, 114(45):12062–12066, 2010.

[34] D. M. Niedzwiedzki and R. E. Blankenship. Singlet and triplet excited state properties of natural chlorophylls and bacteriochlorophylls. *Photosynthesis Research*, 106(3):227–238, 2010.

[35] Yikrazuul. Structure of chlorophyll a, b and d @ONLINE, available from: `https://commons.wikimedia.org/wiki/File:Chlorophyll_a_b_d.svg`, [accessed 5 october 2016], 2009.

[36] R. P. Ilagan, J. F. Koscielecki, R. G. Hiller, F. P. Sharples, G. N. Gibson, R. R. Birge, and H. A. Frank. Femtosecond time-resolved absorption spectroscopy of main-form and high-salt peridinin-chlorophyll *a*-proteins at low temperatures. *Biochemistry*, 45(47):14052–14063, 2006.

[37] D. DellaPenna. Carotenoid Synthesis and Function in Plants: Insights from Mutant Studies in *Arabidopsis thaliana*. In Harry A Frank, Andrew J Young, George Britton, and Richard J Cogdell, editors, *The Photochemistry of Carotenoids*, pages 21–37. Springer Netherlands, Dordrecht, 1999.

[38] J. Alster, T. Polívka, J. B. Arellano, P. Chábera, F. Vácha, and J. Pšenčík. β-Carotene to bacteriochlorophyll *c* energy transfer in self-assembled aggregates mimicking chlorosomes. *Chemical Physics*, 373(1-2):90–97, 2010.

[39] D. M. Niedzwiedzki, J. O. Sullivan, T. Polívka, R. R. Birge, and H. Frank. Femtosecond time-resolved transient absorption spectroscopy of xanthophylls. *The journal of physical chemistry. B*, 110(45):22872–22885, 2006.

[40] T. Polívka and H. A. Frank. Molecular Factors Controlling Photosynthetic Light Harvesting by Carotenoids. *Accounts of Chemical Research*, 43(8):1125–1134, 2010.

[41] J. R. Ferraro. *Introductory raman spectroscopy*. Academic press, 2003.

[42] R. W. Carter. Representation theory of the 0-Hecke algebra. *Journal of algebra*, 104(1):89–103, 1986.

[43] L. Fiedor, Heriyanto, J. Fiedor, and M. Pilch. Effects of Molecular Symmetry on the Electronic Transitions in Carotenoids. *The Journal of Physical Chemistry Letters*, 7(10):1821–1829, 2016.

[44] L. Dall'Osto, R. Bassi, and A. Ruban. Photoprotective Mechanisms: Carotenoids. In *Plastid Biology*, chapter 15, pages 393–428. Springer Science+Business Media, New York, 2014.

[45] D. Zigmantas, R. G. Hiller, A. Yartsev, and V. Sundstro. Dynamics of Excited States of the Carotenoid Peridinin in Polar Solvents: Dependence on Excitation Wavelength, Viscosity, and Temperature. *The Journal of Physical Chemistry B*, 107(22):5339–5348, 2003.

[46] Edgar181. Chemical structure of peridinin @ONLINE, available from: `https://commons.wikimedia.org/wiki/File:Peridinin.png`, [accessed 5 october 2016], 2008.

[47] M. M. Enriquez, M. Fuciman, A. M. Lafountain, N. L. Wagner, R. Robert, and H. A. Frank. The Intramolecular Charge Transfer State in Carbonyl-Containing Polyenes and Carotenoids. *Journal of physical Chemistry B*, 114(38):12416–12426, 2011.

[48] E. Papagiannakis, M. Vengris, D. S. Larsen, I. H. M. Van Stokkum, R. G. Hiller, and R. Van Grondelle. Use of Ultrafast Dispersed Pump-Dump-Probe and Pump-Repump-Probe Spectroscopies to Explore the Light-Induced Dynamics of Peridinin in Solution. *J. Phys. Chem. B*, 110(1):512–521, 2006.

[49] R. P. Ilagan. *Spectroscopic Properties of Carotenoids in Red and Blue Hues*. PhD thesis, University of Connecticut, 2006.

[50] M. Hoffmann, K. Schmidt, T. Fritz, T. Hasche, V. M. Agranovich, and K. Leo. The lowest energy Frenkel and charge-transfer excitons in quasi-one-dimensional structures: Application to MePTCDI and PTCDA crystals. *Chemical Physics*, 258(1):73–96, 2000.

[51] T. Mančal, L. Valkunas, and G. R. Fleming. Theory of exciton-charge transfer state coupled systems. *Chemical Physics Letters*, 432(1-3):301–305, 2006.

[52] S. Kaligotla, S. Doyle, D. M. Niedzwiedzki, S. Hasegawa, T. Kajikawa, S. Katsumura, and H. A. Frank. Triplet state spectra and dynamics of peridinin analogs having different extents of pi-electron conjugation. *Photosynthesis Research*, 103(3):167–174, 2010.

[53] H. A. Frank and R. L. Christensen. *Singlet Energy Transfer from Carotenoids to Bacteriochlorophylls*, pages 373–384. Springer Netherlands, Dordrecht, 1995.

[54] Yikrazuul. Structure of violaxanthin @ONLINE, available from: `https://commons.wikimedia.org/wiki/File:Luteine_-_Lutein.svg`, [accessed 5 october 2016], 2008.

[55] J. Standfuss, A. C. Terwisscha van Scheltinga, M. Lamborghini, and W. Kühlbrandt. Mechanisms of photoprotection and nonphotochemical quenching in pea light-harvesting complex at 2.5 A resolution. *The EMBO Journal*, 24(5):919–928, 2005.

[56] NEUROtiker. Structure of beta-carotene @ONLINE, available from: `https://commons.wikimedia.org/wiki/File:Beta-Carotin.svg`, [accessed 5 october 2016], 2007.

[57] G. E. Białek-Bylka, B. Jazurek, R. Dědic, J. Hála, and A. Skrzypczak. Unique spectroscopic properties of synthetic 15-cis β-carotene, an important compound in photosynthesis, and a medicine for photoprotective function. *Cellular and Molecular Biology Letters*, 8(3):689–697, 2003.

[58] V. Šlouf, M. Fuciman, S. Johanning, E. Hofmann, H. A. Frank, and T. Polívka. Low-temperature time-resolved spectroscopic study of the major light-harvesting complex of *Amphidinium carterae*. *Photosynthesis Research*, 117(1-3):257–265, 2013.

[59] K. Schmidt, M. Maarzahl, and F. Mayer. Development and pigmentation of chlorosomes in *Chloroflexus aurantiacus* strain Ok-70-fl. *Archives of Microbiology*, 127(2):87–97, 1980.

[60] T. Barros and W. Kühlbrandt. Crystallisation, structure and function of plant light-harvesting Complex II. *Biochimica et biophysica acta*, 1787(6):753–72, 2009.

[61] A. Dreuw, G. R. Fleming, and M. Head-Gordon. Chlorophyll fluorescence quenching by xanthophylls. *Physical Chemistry Chemical Physics*, 5(15):3247, 2003.

[62] W. Kühlbrandt and D. N. Wang. Three-dimensional structure of plant light-harvesting complex determined by electron crystallography. *Nature*, 350(February):130–134, 1991.

[63] J. Wu, F. Liu, Y. Shen, J. Cao, and R. J. Silbey. Efficient energy transfer in light-harvesting systems, I: Optimal temperature, reorganization energy and spatial-temporal correlations. *New Journal of Physics*, 12(10):105012, 2010.

[64] K. L. Wells, P. H. Lambrev, Z. Zhang, G. Garab, and H.-S. Tan. Pathways of energy transfer in LHCII revealed by room-temperature 2D electronic spectroscopy. *Physical chemistry chemical physics : PCCP*, 16(23):11640–6, 2014.

[65] H. Rogl and W. Kühlbrandt. Mutant trimers of light-harvesting complex II exhibit altered pigment content and spectroscopic features. *Biochemistry*, 38(49):16214–16222, 1999.

[66] H. Rogl, R. Schödel, H. Lokstein, W. Kühlbrandt, and A. Schubert. Assignment of spectral substructures to pigment-binding sites in higher plant light-harvesting complex LHC-II. *Biochemistry*, 41(7):2281–2287, 2002.

[67] I. Heinze, E. Pfundel, and M. Huhn. Assembly of light harvesting complexes II (LHC-II) in the absence of lutein: A study on the α-carotenoid-free mutant C-2A X -34 of the green alga. *Biochimica et Biophysica Acta*, 1320:188–194, 1997.

[68] S. Takaichi and M. Mirauro. Distribution and Geometric Isomerism of Neoxanthin in Oxygenic Phototrophs: 9-Cis, a Sole Molecular Form. *Plant Cell Physiol*, 39(9):968–977, 1998.

[69] M. Di Valentin, E. Salvadori, G. Agostini, F. Biasibetti, S. Ceola, R. Hiller, G. M. Giacometti, and D. Carbonera. Triplet-triplet energy transfer in the major intrinsic light-harvesting complex of *Amphidinium carterae* as revealed by ODMR and EPR spectroscopies. *Biochimica et Biophysica Acta - Bioenergetics*, 1797(10):1759–1767, 2010.

[70] P. Müller, X.-P. Li, and K. K. Niyogi. Non-photochemical quenching. A response to excess light energy. *Plant physiology*, 125(4):1558–1566, 2001.

[71] D. L. Spector. Dinoflagellates. *The Quarterly Review of Biology*, 60(4):508–508, 1985.

[72] J. Jiang, H. Zhang, G. S. Orf, Y. Lu, W. Xu, L. B. Harrington, H. Liu, C. S. Lo, and R. E. Blankenship. Evidence of functional trimeric chlorophyll a/c_2-peridinin proteins in the *dinoflagellate Symbiodinium*. *Biochimica et Biophysica Acta - Bioenergetics*, 1837(11):1904–1912, 2014.

[73] M. Stomp, J. Huisman, L. J. Stal, and H. C. P. Matthijs. Colorful niches of phototrophic microorganisms shaped by vibrations of the water molecule. *The ISME journal*, 1(4):271–282, 2007.

[74] R. G. Hiller, P. M. Wrench, A. P. Gooley, G. Shoebridge, and J. Breton. The major intrinsic light-harvesting protein of *Amphidinium*: characterization and relation to other light-harvesting proteins. *Photochemistry and Photobiology*, 57(I):125–131, 1993.

[75] R. G. Hiller, P. M. Wrench, and F. P. Sharples. The light-harvesting chlorophyll *a*-*c*-binding protein of *dinoflagellates*: a putative polyprotein. *FEBS Letters*, 363(1-2):175–178, 1995.

[76] W. Kühlbrandt, D. N. Wang, and Y. Fujiyoshi. Atomic model of plant light-harvesting complex by electron crystallography. *Nature*, 367(6464):614, 1994.

[77] H. Y. Yamamoto. Xanthophyll cycles. *methods in Enzymology*, 110:303–312, 1985.

[78] J. Pšenčík, S. J. Butcher, and R. Tuma. Chlorosomes: Structure, Function and Assembly. In *The Structural Basis of Biological Energy Generation*, pages 77–109. Springer Netherlands, Dordrecht, 2014.

[79] J. T. Beatty, J. Overmann, M. T. Lince, A. K. Manske, A. S. Lang, R. E. Blankenship, C. L. Van Dover, T. A. Martinson, and F. G. Plumley. An obligately photosynthetic bacterial anaerobe from a deep-sea hydrothermal vent. *Proceedings of the National Academy of Sciences of the United States of America*, 102(26):9306–9310, 2005.

[80] J. Overmann, H. Cypionka, and N. Pfennig. An extremely low-light adapted phototrophic sulfur bacterium from the Black Sea. *Limnology and oceanography*, 37(1):150–155, 1992.

[81] J. Pšenčík, J. B. Arellano, T. P. Ikonen, C. M. Borrego, P. Laurinmäki, S. J. Butcher, R. E. Serimaa, and R. Tuma. Internal structure of chlorosomes from brown-colored *chlorobium* species and the role of carotenoids in their assembly. *Biophysical journal*, 91(4):1433–1440, 2006.

[82] R. E. Blankenship and K. Matsuura. Antenna complexes from green photosynthetic bacteria. In *Light-harvesting antennas in photosynthesis*, pages 195–217. Springer, 2003.

[83] P. Hildebrandt, H. Tamiaki, A. R. Holzwarth, and K. Schaffner. Resonance Raman spectroscopic study of metallochlorin aggregates. Implications for the supramolecular structure in chlorosomal BChl *c* antennae of green bacteria. *Journal of Physical Chemistry*, 98(8), 1994.

[84] L. N. Halfen, B. K. Pierson, and G. W. Francis. Carotenoids of a gliding organism containing bacteriochlorophylls. *Archiv für Mikrobiologie*, 82(3):240–246, 1972.

[85] Z. Wang, A. C. Bovik, H. R. Sheikh, and E. P. Simoncelli. Image quality assessment: from error visibility to structural similarity. *IEEE transactions on image processing*, 13(4):600–612, 2004.

[86] N.-U. Frigaard, S. Takaichi, M. Hirota, K. Shimada, and K. Matsuura. Quinones in chlorosomes of green sulfur bacteria and their role in the redox-dependent fluorescence studied in chlorosome-like bacteriochlorophyll *c* aggregates. *Archives of microbiology*, 167(6):343–349, 1997.

[87] T. B. Mellø, N. U. Frigaard, K. Matsuura, and K. Razi Naqvi. Electronic energy transfer involving carotenoid pigments in chlorosomes of two green bacteria: *Chlorobium tepidum* and *Chloroflexus aurantiacus*. *Spectrochimica Acta Part A*, 56A(10):2001–2010, 2000.

[88] J. B. Arellano, T. B. Melø, C. M. Borrego, J. Garcia-Gil, and K. Razi Naqvi. Nanosecond Laser Photolysis Studies of Chlorosomes and Artificial Aggregates Containing Bacteriochlorophyll *e*: Evidence for the Proximity of Carotenoids and Bacteriochlorophyll *a* in Chlorosomes From *Chlorobium Phaeobacteroides* Strain CL1401. *Photochemistry and photobiology*, 72(5):669–675, 2000.

[89] H. Kim, H. Li, J. A. Maresca, D. A. Bryant, and S. Savikhin. Triplet exciton formation as a novel photoprotection mechanism in chlorosomes of *Chlorobium tepidum*. *Biophysical journal*, 93(1):192–201, 2007.

[90] A. A. Krasnovsky, J. Lopez, P. Cheng, P. A. Liddell, R. E. Blankenship, T. A. Moore, and D. Gust. Generation and quenching of singlet molecular oxygen by aggregated bacteriochlorophyll d in model systems and chlorosomes. *Photosynthesis research*, 40(2):191–198, 1994.

[91] J. Pšenčík, J. B. Arellano, A. M. Collins, P. Laurinmäki, M. Torkkeli, B. Löflund, R. E. Serimaa, R. E. Blankenship, R. Tuma, and S. J. Butcher. Structural and functional roles of carotenoids in chlorosomes. *Journal of Bacteriology*, 195(8):1727–1734, 2013.

[92] J. Alster. *Study of light-harvesting antennae based on bacterio chlorophyll aggregates*. PhD thesis, Charles University in Prague, Faculty of Mathematics and Physics, 2011.

[93] P. W. Hemelrijk, S. L. S. Kwa, R. van Grondelle, and J. P. Dekker. Spectroscopic properties of LHC-II, the main light-harvesting chlorophyll a/b protein complex from chloroplast membranes. *BBA - Bioenergetics*, 1098(2):159–166, 1992.

[94] S. Savikhin, H. van Amerongen, S. L. S. Kwa, R. van Grondelle, and W. S. Struve. Ultrafast energy transfer in LHC-II trimers from the Chl a/b light-harvesting antenna of Photosystem II. *Biophysical Journal*, 1102(2):202–212, 1994.

[95] R. Schödel, K. D. Irrgang, J. Voigt, and G. Renger. Quenching of chlorophyll fluorescence by triplets in solubilized light-harvesting complex II (LHCII). *Biophysical journal*, 76(4):2238–2248, 1999.

[96] D. Siefermann-Harms and A. Angerhofer. Evidence for an O_2-barrier in the light-harvesting chlorophyll-a/b-protein complex LHC II. *Photosynthesis Research*, 55(1):83–94, 1998.

[97] G. F. W. Searle, R. Tamkivi, A. Vanhoek, and T. J. Schaafsma. Temperature-Dependence of Antennae Chlorophyll Fluorescence Kinetics in Photosystem-I Reaction Center Protein. *Journal of the Chemical Society-Faraday Transactions II*, 84(July 1986):315–327, 1988.

[98] F. Kita, W. Adam, P. Jordan, W. M. Nau, J. Wirz, A. Hubland, and V. Uni. 1, 3-Cyclopentanediyl Diradicals: Substituent and Temperature Dependence of Triplet - Singlet Intersystem Crossing. *J. Am. Chem. Soc.*, 121(11):9265–9275, 1999.

[99] A. Angerhofer. *Electron Magnetic Resonance of Carotenoids*, pages 203–222. Springer Netherlands, Dordrecht, 1999.

[100] R. van der Vos, D. Carbonera, and A. J. Hoff. Microwave and Optical Spectroscopy of Carotenoid Triplets in Light-Harvesting Complex LHC II of Spinach by Absorbance-Detected Magnetic Resonance. *Applied Magnetic Resonance*, 202(2):179–202, 1991.

[101] T. Jávorfi, G. Garab, and K. Razi Naqvi. Reinvestigation of the triplet-minus-singlet spectrum of chloroplasts. *Spectrochimica Acta - Part A: Molecular and Biomolecular Spectroscopy*, 56(1):211–214, 2000.

[102] I. S. Vinklárek, M. Scholz, R. Dědic, and J. Hála. Singlet oxygen feedback delayed fluorescence of protoporphyrin IX in organic solutions. *Photochem. Photobiol. Sci.*, 16:507–518, 2017.

[103] P. G. Adams, A. J. Cadby, B. Robinson, Y. Tsukatani, M. Tank, J. Wen, R. E. Blankenship, D. A. Bryant, and C. N. Hunter. Comparison of the physical characteristics of chlorosomes from three different *phyla* of green phototrophic bacteria. *Biochimica et Biophysica Acta - Bioenergetics*, 1827(10):1235–1244, 2013.

[104] R. P. Lehmann, R. A. Brunisholz, and H. Zuber. Structural differences in chlorosomes from *Chloroflexus aurantiacus* grown under different conditions support the BChl *c*-binding function of the 5.7 kDa polypeptide. *FEBS Letters*, 342(3):319–324, 1994.

[105] J. Pšenčík, A. M. Collins, L. Liljeroos, M. Torkkeli, P. Laurinmäki, H. M. Ansink, T. P. Ikonen, R. E. Serimaa, R. E. Blankenship, R. Tuma, and S. J. Butcher. Structure of chlorosomes from the green filamentous bacterium *Chloroflexus aurantiacus*. *Journal of Bacteriology*, 191(21):6701–6708, 2009.

[106] J. S. Connolly, E. B. Samuel, and A. F. Janzen. Effects of solvent on the fluorescence propertioes of bacteriochlotophyll *a*. *Photochemistry and Photobiology*, 36(5):565–574, 1982.

[107] D. C. Brune, R. E. Blankenship, and G. R. Seely. Flurescence quantum yields and lifetimes for bacteriochlorophyll *c*. *Photochemistry and Photobiology*, 47(5):759–763, 1988.

List of Figures

List of Abbreviations

- $^1O_2$: molecular oxygen in the first singlet excited state
- $^3O_2$: molecular oxygen in the ground state
- acpPC: chlorophyll *a*-chlorophyll c_2-peridinin-protein complex
- A: acceptor
- ATP: Adenosin triphosphate
- BChl(s) *a*and *c*: bacteriochlorophyll(s) *a* and *c*
- Car: carotenoid
- Chl(s) *a* and *b* and c_2: chlorophyll(s) *a* and *b* and c_2
- *Clf.*: *Chloroflexi*
- CU: control unit
- D: donor
- DAS: decay associated spectra (singular: DA spectrum)
- DDM: n-Dodecyl β-D-maltoside
- DET: Dexter energy transfer
- DF: delayed fluorescence
- DG: delayed generator
- DM: n-decyl β-D-maltoside
- Em.: emission
- ESA: excited state absorption
- ET: energy transfer
- FRET: Förster resonant energy transfer
- FWHM: full width at half maximum
- GSB: the ground state bleaching
- HOMO: the highest occupied molecular orbital
- IC: internal conversion
- iCCD (camera): an intesified charge coupled device (camera)
- ICT (state): intramolecular charge transfer (state)

- IRF: instrument response function
- ISC: intersystem crossing
- LHC(s): light-harvesting complex(es)
- LHC-II: light-harvesting complex II of higher plants
- LUMO: the lowest unoccupied molecular orbital
- M(-porphin): metal(-porphin)
- M_i: molecule denoted as i
- NAD(H): nicotinamide adenine dinucleotide (in reduced form)
- ND (filter): neutral density (filter)
- NPQ: non-photochemical quenching
- OD: optical density
- OPO: optical parametric oscillator
- P: turbomolecular pump
- PCP (complex): peridinin-chlorophyll-a-protein (complex)
- PS: photosystem
- PTG: timing generator
- R: reference
- RC(s): (the) reaction centre(s)
- RT: room temperature
- RTSH: room temperature sample holder
- S: (the) sample
- S_0 (state): (the) ground siglet (state)
- S_n (state), $n > 0$: (the) n-th singlet excited (state)
- S/N (ratio): the signal to noise (ratio)
- T_n (state), $n > 0$: (the) n-th triplet excited (state)
- T-S (spectra): triplet minus singlet (spectra)
- TA (spectrum): transient absorption (spectrum)
- TTA: triplet-triplet annihilation
- UV (spectrum): ultraviolet (spectrum)
- VIS (spectrum): visible (spectrum)

Attachments